

# **FIBRE SPREADING AND IMPREGNATION MONITORING**



by

**Francisco Daniel Nieves Bogonez**

A dissertation submitted to the  
University of Birmingham  
for the degree of  
MASTER of RESEARCH

School of Metallurgy and Materials

College of Engineering & Physical Sciences

University of Birmingham

November 2013

UNIVERSITY OF  
BIRMINGHAM

**University of Birmingham Research Archive**

**e-theses repository**

This unpublished thesis/dissertation is copyright of the author and/or third parties. The intellectual property rights of the author or third parties in respect of this work are as defined by The Copyright Designs and Patents Act 1988 or as modified by any successor legislation.

Any use made of information contained in this thesis/dissertation must be in accordance with that legislation and must be properly acknowledged. Further distribution or reproduction in any format is prohibited without the permission of the copyright holder.

## **Abstract**

A novel methodology based on the use of low cost CMOS-cameras and pigmented photo-curable resin has been developed and successfully evaluated under laboratory conditions for measuring quantitatively through-thickness impregnation of as-received and spread E-glass fibres. Test results showed that as-received PPG fibres exhibit higher impregnation rates when compared with as-received Owens Corning fibres. Further tests on spread PPG fibres clearly revealed that the spreading process of the fibres results in a dramatic increase of permeability and thus significantly faster impregnation rates.

An innovative monitoring technique also based on the use of CMOS-cameras was investigated in parallel for evaluating variations in the thickness and tension of glass fibre creels during unwinding. In order to enable the assessment of the novel monitoring technique a special test rig was constructed and instrumented with two load cells and the two CMOS-cameras. Tests were carried out using either centre-pull or external-draw unwinding methods. Results have demonstrated that the centre-pull technique creates more variations on the tow geometry giving a higher variability in thickness in comparison to external-draw unwinding. Furthermore, it was seen that the tow thickness in PPG fibres decreased as the diameter of the creel increased.

## **Dedication**

This thesis is dedicated to my fiancé Mariana and to my family for their unconditional support and understanding in this adventure of returning to the University. This work would not be possible without them; thank you so much.

## **Acknowledgements**

I would like to thank Professor Fernando and the University of Birmingham for the financial support given during this Master. In addition, I would like to personally acknowledge the labour of Professor Fernando during this year transmitting to me his passion for research and science, and for his personal guidance and support.

I would like to acknowledge Dr. Papaelias for all his help, feedback, understanding and trust.

I would also like to thank the valuable contribution of Mr. Warren Hay for all his help in improving my designs and for his commitment in finishing the manufacturing of all the parts on time. Finally, I would like to recognise the assistance of Dr. M.S. Irfan for his helpful feedback and constructive discussions during the writing of this dissertation.

# Table of Contents

<b>1</b>	<b>Introduction and aims</b> .....	<b>1</b>
1.1	Introduction.....	1
1.2	Aims and objectives.....	2
<b>2</b>	<b>Literature review</b> .....	<b>5</b>
2.1	Epoxy resin systems.....	5
2.2	Glass fibre manufacture.....	6
2.3	Coupling agent.....	7
2.4	Resin impregnation.....	8
2.4.1	Models to predict the behaviour of the impregnation process.....	8
2.4.1.1	Permeability coefficient.....	10
2.4.1.2	Pressure gradient.....	13
2.4.2	Impregnation monitoring.....	14
2.5	Fibre spreading.....	16
<b>3</b>	<b>Experimental</b> .....	<b>18</b>
3.1	Impregnation monitoring.....	18
3.1.1	Materials.....	18
3.1.1.1	Resin system.....	18
3.1.1.2	Fibres.....	19
3.1.1.3	Camera stand and the lightning system.....	20
3.1.1.4	Software to enable real-time monitoring of impregnation, and software calibration.....	23
3.1.1.5	Calibration of the cameras.....	25
3.1.1.6	Image analysis process description.....	26

3.1.1.6.1	Upper CMOS camera.....	26
3.1.1.6.2	Bottom CMOS camera.....	29
3.1.2	Monitoring fibre spreading.....	30
3.1.2.1	Image analysis and measurement system .....	35
3.1.2.2	Tow width measurement algorithm .....	36
<b>4</b>	<b>Results and discussion.....</b>	<b>38</b>
4.1	Impregnation monitoring .....	38
4.1.1	UV resin viscosity .....	38
4.1.2	Calibration of the dispensed UV resin .....	39
4.1.3	Measurement methodology validation and maximum error definition.....	39
4.1.3.1	Top camera - error calculation.....	42
4.1.3.2	Bottom camera - error calculation .....	45
4.1.4	Impregnation results.....	46
4.1.4.1	Variation in the width of the samples used in the tests.....	48
4.1.4.2	XY-impregnation .....	49
4.1.4.3	Through-thickness impregnation .....	53
4.1.4.4	Comparison of the global averages.....	55
4.1.4.5	Permeability calculations .....	58
4.1.5	“Freezing” the resin flow .....	60
4.2	On line-monitoring of the thickness of the tow .....	62
4.2.1	Airtightness of the pneumatic system .....	62
4.2.2	Load-cells calibration.....	63
4.2.3	Correlation between the measured force and the thickness of the tow .....	63
4.2.4	Thickness and width measurement using Hybon 2026 Tex 2400.....	66

4.2.4.1	Thickness variation: external-draw experiments .....	71
4.2.4.1.1	External layer .....	72
4.2.4.1.2	Centre layer .....	73
4.2.4.1.3	Internal layer .....	74
4.2.4.1.4	Summary of the external-draw experiments .....	75
4.2.4.2	Thickness variation in the tow: centre-pull experiments .....	75
4.2.4.2.1	External layer .....	76
4.2.4.2.2	Centre layer .....	77
4.2.4.2.3	Internal layer .....	78
4.2.4.2.4	Summary of the centre-pull experiments .....	79
4.2.4.3	Thickness comparison between centre-pull and external-draw .....	80
4.2.4.4	Width variation in the tow: external-draw experiments .....	81
4.2.4.5	Width measurement: centre-pull experiments .....	83
4.2.4.6	Width comparison between both unwinding methods .....	85
4.2.5	Tension measurements .....	86
<b>5</b>	<b>Conclusions .....</b>	<b>88</b>
<b>6</b>	<b>Future work .....</b>	<b>91</b>
<b>7</b>	<b>References .....</b>	<b>92</b>

# List of Figures

Figure 1 Structure of: (i) DGEBA; and (ii) TGDDM.....	5
Figure 2 Main reactions that can take place during the cross-linking process: primary (i) and secondary (ii) amine-epoxy addition; and (iii) etherification [10].....	6
Figure 3 Longitudinal and transversal permeability obtained by Gebart's equation for different levels of porosity.....	11
Figure 4 Definition of the relative positions of the creel: external layer top/medium/bottom, central layer top/medium/bottom and internal layer top/medium/bottom.....	20
Figure 5 Schematic illustration of an isometric perspective (a) and a frontal view (b) showing the fixtures for housing the two CMOS-microscope cameras, the fibre bundle and the LED-based illumination system.....	21
Figure 6 A magnified view of the platform for housing the fibre bundle, imaging and illuminating systems for the impregnation studies.....	23
Figure 7 Screen-shot depicting the user interface for the two CMOS cameras when (i) and (ii) show the top and bottom real image respectively, and (iii) and (iv) show the top and bottom image (again respectively) after the image analysis. The calculated values are inserted in the (v), and the controls shown in (vi) allows us to take a picture of the dry tows and to start the test. Finally (vii) shows the remaining test time and (viii) is the test stop.....	24
Figure 8 Examples of typical images captured by the: (i) top; and (ii) bottom CMOS cameras.....	26
Figure 9 Detail of axial or capillary impregnation recorded by the top USB microscope.....	27

Figure 10 Illustration of the image-subtracting process. Image of the: (i) as-received bundle; (ii) resin on the bundle; (iii) computer-generated image after the subtraction process which isolates the resin drop.....	28
Figure 11 Illustration of the software-based extraction of the “wet” area and analysis: (i) black and white image of the resin drop; (ii) software-based computation process.....	29
Figure 12 Images captured from the camera positioned at the bottom and the subsequent image processing routines: (i) a typical image captured from the camera positioned below the bundle; (ii) shows the image after the subtraction operation; and (iii) is the result after image processing and the threshold application. ....	30
Figure 13 Schematic illustration of the rig that was designed and built to study the various parameters that influence the degree of fibre spreading. ....	31
Figure 14 Schematic illustration depicting the adjustability of the inner frame. ....	31
Figure 15 Schematic illustration of the construction of the internal frame showing the adjustability of the pair of rollers. (i) Representation of the slots in the internal frame for guiding the internal bridge and the 3 kg load-cell which attach the internal platform to the floor of the external platform. Illustrations (ii) and (iii) show the pneumatic cylinder in inactive and active positions respectively.....	32
Figure 16 Details of the software interface: (i) general overview and location of the three main areas (tab control with the configuration menus, bottom area and data visualisation); (ii) Different options which can be found in the tab menu (iii) Bottom area with sampling rate indicator and test start/stop, data logging and zone of the creel under testing; (iv) Data visualisation area. ....	35

Figure 17 Detail of the relative positions of the two cameras on the rig, where the different clamps used with the cameras have been removed for simplification purposes: (i) isometric perspective where the tow moves from left-to-right; and (ii) top view. ....	36
Figure 18 Edges location perpendicular to the tow movement direction; the detection line is indicated. ....	37
Figure 19 Dynamic viscosity profiles for the NOA63 photo-curable resin as a function of temperature. The data presented are for the as-received and pigmented photo-curable resin (0.5 weight %). ....	38
Figure 20 20x macro-image of the impregnation developed on bottom face of the tow. This image represents a collage of 300 micrographs. ....	42
Figure 21 Results of an impregnation test carried out on a PPG tow obtained from the centre/bottom portion of the creel. ....	43
Figure 22 Details of the image analysis with the top camera. ....	44
Figure 23 Comparison between the image analysis carried out using the manual inspection over the 20x image (images on the left) and the automatic analysis done by the software using the bottom microscope (images in the right). ....	46
Figure 24 Typical example of an impregnation experiment with the definition of each parameter measured during the tests: (i) X and Y-impregnation length, and XY-impregnated area monitored by the upper camera; (ii) Z or through-thickness impregnation monitored by the bottom camera. ....	48
Figure 25 Statistical analysis of the width of the samples used in the impregnation tests: (i) the average and standard deviation of each experiment detailed in Table 6 attending to the segment of the creel in the as-received material (the data are presented in sets of two	

columns showing the average on the left and the standard deviation on the right); (ii) average fibre bundle widths for the spread and as-received PPG fibre bundles and the as-received Owens-Corning fibre bundles.....	49
Figure 26 Evolution of the XY-impregnation for the as-received and spread PPG fibres. The different colours for the as-received fibres correspond to their relative positions from within the creel: (i) shows the full length of the test (200 seconds); (ii) presents an expanded view of the first 25 seconds. The dotted line in Figure 26 (i) represents the average initial slope. ....	51
Figure 27 Evolution of the XY-impregnation for the as-received and spread PPG fibres. The different colours for the as-received fibres correspond to their relative positions from within the creel. The dotted line represents the initial slope.....	52
Figure 28 Through-thickness impregnation for PPG spread and as-received fibres.....	54
Figure 29 Through-thickness impregnation evolution for the Owens Corning as-received fibres. ....	55
Figure 30 Averaged XY-permeation versus time for each different group of fibres: Owens-Corning fibres (blue), as-received PPG fibres (red) and spread PPG fibres (green). The dotted lines (a) and (b) represents the initial slopes.....	56
Figure 31 Averaged through-thickness impregnation evolution versus time for: Owens-Corning fibres (blue); as-received PPG fibres (red); and spread PPG fibres (green). The black dotted lines represent the slopes of the evolution of the through-thickness impregnation area; (a) and (b) show the two different slopes presented by the spread PPG fibres; and (c) shows the slope of the as-received PPG fibres. ....	56

Figure 32 Transversal permeability values for the PPG spread and as-received fibres calculated by Equation 4, with a comparison with the values obtained by Gebart’s model; all the transversal permeability coefficients are calculated for the two considered values of porosity and shown two different colours (44% of porosity in the blue columns and 48% porosity in the red columns), with the standard deviation represented by an error bar..... 59

Figure 33 Illustration of the permeation profile of the pigmented cross-linked photo-curable resin on sample number-4: (i) 10x image of the sample; (ii) 20x image showing the left area of the sample; and (iii) 20x image of the central area of the sample. Due to the nature of the microscope used in conjunction with the camera, it was not possible to obtain a scale bar..... 61

Figure 34 Display of the force monitored by the load-cell over 1200 seconds to establish the pressure-retention capacity of the pneumatic device. .... 62

Figure 35 Representation of the increases of the force measured in the load-cell for the different initial forces and for the different thicknesses of the feeler gauges. .... 65

Figure 36 Detail of the unwind method using with the PPG Hybon 2026 Tex 2400 creels: (i) centre-pull; and (ii) external-draw. .... 66

Figure 37 Example of the typical measurements obtained during the experiments: (i) thickness measurements via the pressure load-cell; and (ii) the tow width measurements obtained by analysing the images taken by the input and output cameras. .... 68

Figure 38 Magnification of the superposition of the data, after adding and subtracting the temporal offset from the input and output cameras respectively: (i) a section of the tow

with steady changes in the width/thickness; meanwhile the graph (ii) illustration of a twisted section..... 70

Figure 39 Summary of the thickness of a tow where the bundle was unwound using external-draw. Figure 39 (i) shows the thickness variation for the full experiment. Figure 39 (ii), (iii) and (iv) represents the thickness variation in the top, middle and bottom zones for the external layer of the creel. Figure 39 (v) shows the mean and the standard deviation for the thickness variation for each zone in the external layer of the creel..... 72

Figure 40 Summary of the thickness of a tow where the bundle was unwound using external-draw. Figure 40 (i) shows the thickness variation for the full experiment. Figure 40 (ii), (iii) and (iv) represents the thickness variation in the top, middle and bottom zones for the middle layer of the creel. Figure 40 (v) shows the mean and the standard deviation for the thickness variation for each zone in the centre layer of the creel..... 73

Figure 41 Summary of the thickness of a tow where the bundle was unwound using external-draw. Figure 41 (i) shows the thickness variation for the full experiment. Figure 41 (ii), (iii) and (iv) represents the thickness variation in the top, middle and bottom zones for the inner layer of the creel. Figure 41 (v) shows of the mean and the standard deviation for the thickness variation for each zone in the inner layer of the creel..... 74

Figure 42 Summary of the external-draw experiments where four sets of data are shown with the mean (coloured columns) and the  $\pm$  standard deviation (error bar): the first

dataset compares all the points for each layer, and the next three datasets compare the widths for the top, middle and bottom layers. ....	75
Figure 43 Summary of the thickness of a tow where the bundle was unwound using centre-pull. This dataset represents the outer zone of the creel. Figure 43 (i) shows the thickness variation for the full experiment. Figure 43 (ii), (iii) and (iv) represents the thickness variation in the top, middle and bottom zones for the external layer of the creel. Figure 43 (v) shows the mean and the standard deviation for the thickness variation for each zone in the external layer of the creel.....	76
Figure 44 Summary of the thickness of a tow where the bundle was unwound using centre-pull. This dataset represents the mid zone of the creel. Figure 44 (i) shows the thickness variation for the full experiment. Figure 44 (ii), (iii) and (iv) represents the thickness variation in the top, middle and bottom zones for the mid layer of the creel. Figure 44 (v) shows the mean and the standard deviation for the thickness variation for each zone in the mid layer of the creel. ....	77
Figure 45 Summary of the thickness of a tow where the bundle was unwound using centre-pull. This dataset represents the inner zone of the creel. Figure 45 (i) shows the thickness variation for the full set of experiments. Figure 45 (ii), (iii) and (iv) represents the thickness variation in the top, middle and bottom zones for the inner bore layer of the creel. Figure 45 (v) shows the mean and the standard deviation for the thickness variation for each zone in the inner layer of the creel. ....	78
Figure 46 Summary of the centre-pull experiments where four datasets are shown with the mean (coloured columns) and the $\pm$ standard deviation (error bars). The first dataset	

compares all the points for each layer. The remaining three datasets compare the widths of the tow in the top, middle and bottom positions of the creel. ....	79
Figure 47 Measured thickness of the tow as a function of the method of un-winding technique. The data are presented in two datasets which shown the mean (colour-coded columns) and the $\pm$ standard deviation (error bars). ....	80
Figure 48 Summary of the relative tow widths measured by the tow input and the output cameras for a creel of Hybon 2026 Tex 2400 (PPG). Here the tow was unwound by external-draw. Figure 48 (i) and (ii) show the distribution of the tow widths for the external layer. Figure 48 (iii) and (iv) show the distribution of the readings in the centre layer; and Figure 48 (v) and (vi) show the distribution of the readings in the internal layer. ....	82
Figure 49 Consolidated data tow width for the various layers and zones for the creel. The histograms represent data acquired by the input and output cameras as the tow enters and leaves the pair of rollers. This dataset is for the a creel of PPG Hybon 2026 Tex 2400, unwound using the external-draw method. ....	82
Figure 50 Summary of the relative tow widths measured by the tow input and the output cameras for a creel of Hybon 2026 Tex 2400 (PPG). Here the tow was unwound by centre-pull. Figure 50 (i) and (ii) show the distribution of the tow widths for the external layer. Figure 50 (iii) and (iv) show the distribution of the readings in the centre layer; and Figure 50 (v) and (vi) show the distribution of the readings in the internal layer. ....	84
Figure 51 Consolidated data tow width for the various layers and zones for the creel. The histograms represent data acquired by the input and output cameras as the tow enters	

and leaves the pair of rollers. This dataset is for a creel of PPG Hybon 2026 Tex 2400, unwound using the centre-pull method..... 84

Figure 52 Width comparison by layers for the two unwind methods showing; (i) the width as measured by the input camera or before passing through the rig; and (ii) the width as measured by the output camera or after passing through the rig. The columns show the means, and the error bars represent the  $\pm$  standard deviation. .... 85

Figure 53 Superposition of the readings of the pressure load-cell (red, with scale on the right) and the tension load-cell (blue, with scale in the left) during 150 seconds. .... 86

## List of Tables

Table 1 Summary of selected models for axial and transverse permeability. Compiled from references [18, 22-24], where $P_c$ is the capillary pressure, $\varepsilon$ is the porosity, $a_h$ is the gradient of velocity against distance and $k$ is the Kozeny constant.....	12
Table 2 Summary of data obtained for from the digital calliper and the cameras using “reference” objects. Table (a) shows the data obtained using a metallic disc and (b) a plastic cylinder.....	25
Table 3 Mass of each drop of the pigmented resin dispensed from the micro-pipette.....	39
Table 4 Error analysis obtained in the six experiments performed, comparing the manual results with the ones obtained by the software. ....	44
Table 5 Error associated with the bottom camera. ....	45
Table 6 Summary of the number of tests, materials, condition of the fibres and their relative positions within the creel for the impregnation monitoring studies. ....	47
Table 7 Summary of the averages and the standard deviations for the increases in the force measured by the load-cell as a function of the thickness of the feeler gauges. ....	64
Table 8 Summary of the tow length tested as a function of the position of the tow into the creel for centre-pull and outside-draw methods for unwinding. These experiments were carried out on Hybon 2026 Tex 2400 (PPG). ....	67

# **1 Introduction and aims**

## **1.1 Introduction**

Composites consist of three constitutive components: the matrix, the interface and the reinforcement. They can be found in nature and are engineered to meet the design and end-use requirements for a broad range of industrial applications. A primary attraction of fibre reinforced composites is their high specific properties (ratio of the property of interest to the density) and hence, they are desired materials in applications where weight is at a premium. This is one reason why they are used extensively in the aerospace, marine and automotive sectors.

A wide range of production techniques are available for manufacturing composites including, filament winding [1], pultrusion [2], resin transfer moulding [3], tape-laying [4], or hand layup [5]. Although these production techniques are different, they have some common requirements. For example, the reinforcement has to be impregnated and this applies to both thermoset and thermoplastic-based matrices.

Various techniques can be used to aid the impregnation process including, lowering the viscosity of the resin by dilution or increasing the temperature, using a lower fibre tex or injecting the resin into the fibre bundle under pressure. Another approach that can be taken to accelerate the impregnation process is to spread the filaments in the bundle. A method for enabling the lateral spreading of the filaments in E-glass was demonstrated recently [6]. The factors that were identified in that study as contributing to the ease with which the filaments could be spread were as follows: (i) the binder content on the fibres and the homogeneity of its distribution; (ii) the uniformity of the dimensions of the as-received fibre bundle and the

degree of compaction of the filaments; (iii) the tension (during fibre spreading); and (iv) the degree of twists in the bundle. Apart from the intrinsic twists in the bundle due to the manufacturing of the fibres (E-glass), in manufacturing processes such as pultrusion, the fibre bundle is drawn from the centre of the creel creating a twist in the bundle every time a complete revolution is unwound ( $360^\circ$ ).

The principle objectives of this project were to develop a low-cost and practical technique to monitor the relative dimensions of fibre bundles during processing and also to monitor the relative impregnation rates for as-received and spread fibre bundles. This was achieved by splitting the research effort into two distinct areas.

The first part of the project involved the deployment of a pair of low-cost CMOS (complementary metal-oxide semiconductor) microscope cameras (£24 each) to monitor the impregnation process when a constant volume of 40  $\mu\text{l}$  of resin was pipetted, from a known height and angle, on to the centre of a bundle. The camera on the top was used to monitor the axial and transverse motion of the drop of liquid. The second camera was positioned at the bottom of the bundle and the through-thickness permeation time was estimated.

The second aspect of this study was associated with the design, construction and evaluation of an instrumented rig to measure the tension on the fibres during the spreading process, and to detect the variation in the thickness and in the width in real time.

## **1.2 Aims and objectives**

The key aims and objectives of this study were:

- (i) To design and construct a rig to house a pair of CMOS microscope cameras and a fibre bundle, in order to enable real-time monitoring of the impregnation process.

This objective involved building a platform to house a pair of off-the-shelf CMOS-microscope cameras in a fixed position. An enclosure was also built to eliminate ambient light from interfering with the measurements.

- (ii) To deploy the above-mentioned system for monitoring in real-time the flow-front (axial, transverse and through-thickness) of a drop of a photo-curable resin that was deposited on the surface of a fibre bundle.

A major motivation for spreading the filaments in a bundle is to accelerate the rates of impregnation in the axial, transverse and through-thickness directions. The same CMOS-microscope camera system mentioned previously, was used to monitor the relative positions of the liquid-front. Here, a known volume of a photo-curable resin was dispensed from a pipette on to the top-surface of a fibre bundle. The relative positions of the liquid-front were tracked in real-time using the CMOS-microscope camera and custom-written image analysis software. This study was carried out on as-received and spread fibres from PPG Industries (UK), and on as-received fibres from Owens Corning for comparing the obtained results. In addition, tests were carried out in different sections of the creel for understanding if there were any differences depending on their position in the creel.

- (iii) To deploy an existing fibre spreading station to spread 2400 Tex E-glass fibres (bundles supplied by PPG) and to repeat the experiments detailed in (ii).

The author was involved in a recent publication where a custom-designed rig was used to demonstrate a semi-automatic technique to spread the filament in a bundle of E-glass fibres [7].

- (iv) To design, construct and calibrate a rig to monitor the tension and to detect the relative thickness of the fibre bundle, and the width before and after fibre spreading.

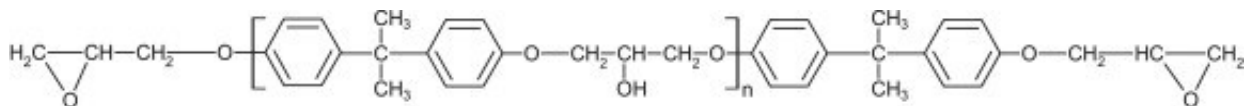
The rig consisted of a pneumatic cylinder to apply the desired force on the bundle as it traversed between a pair of rollers. The rollers were instrumented with a pair of load-cells to monitor the tension and lateral forces on the fibre bundle as it is hauled-off. This facility enables the relation between the tension and the degree of spreading to be correlated. The rig was also used to investigate if the dimension of the fibre bundle was dependent on its relative position on the creel using some fibres from PPG Industries (UK).

## 2 Literature review

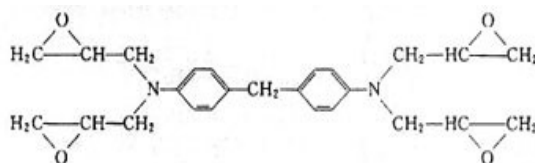
The literature review carried out covered the subjects of interest in this project including, the resin, reinforcement, impregnation modelling and monitoring, and fibre spreading methods.

### 2.1 Epoxy resin systems

The epoxy resins are used extensively for applications such as coatings, adhesives and matrices in composites. There is a broad range of epoxy-based resin systems that can be selected for composite materials, where the most commonly used is the diglycidyl ether of bisphenol-A (DGEBA) [8]. Another typical resin system that is used when high temperature resistance is required is tetraglycidyl-4,4'-diaminodiphenylmethane (TGDDM) [9]. These structures are shown in Figure 1.



(i) Structure of diglycidyl ether of bisphenol-A (DGEBA) [8].



(ii) Tetraglycidyl-4,4'-diaminodiphenylmethane (TGDDM) [9].

Figure 1 Structure of: (i) DGEBA; and (ii) TGDDM.

With reference to the initiation of the cross-linking or polymerisation reactions, several curing agents can be used according to the desired properties. One of the most common curing agents or hardeners are amines. With reference to Figure 2, it is generally accepted that two

main reactions can occur: the primary (i) and the (ii) secondary amine-epoxy addition reactions. However, if the epoxide groups are present in excess, a third reaction can take place known as etherification (iii), where a secondary amine reacts with the epoxy ring leading in the formation of the tertiary amine group [10]. The generalised reactions are shown in the Figure 2.

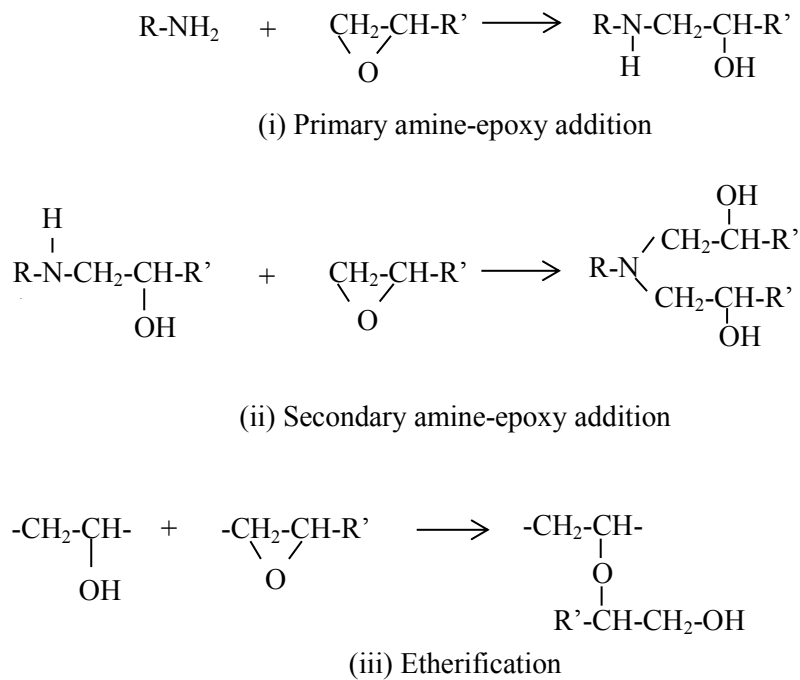


Figure 2 Main reactions that can take place during the cross-linking process: primary (i); secondary (ii) amine-epoxy addition; and (iii) etherification [10].

## 2.2 Glass fibre manufacture

The manufacture of glass fibres is a process which can be divided in five different steps as follows [11]: batching, melting, fibrerisation, coating and drying/packageing .

The batching consists of formulating and mixing the proper proportions of different components of the glass fibre. In the case of E-glass, the main components are SiO<sub>2</sub>, Al<sub>2</sub>O<sub>3</sub>, CaO and MgO [11]. After mixing the components, the mixture is melted in a furnace which is

divided into three areas. The first one is about 1400 °C where the glass is melted and uniformed. The second one called refiner where the temperature is approximately 1370 °C. The last section is where the glass is drawn forming the filaments [7, 11].

The fibre drawing stations of the furnace are formed by bushings made of an erosion-resistant alloy. These bushing plates have very fine orifices (ranging from 200 to as many as 8,000, depending of the desired number of filaments). The temperature within the bushing is controlled electronically to maintain a constant glass viscosity. When the filaments exit from the bushings at around 1204 °C, air-cooling and fine water-mist jets are applied in order to quench the molten “filaments”. In a subsequent station, the filaments are coated with a fluid (typically 0.5 to 2 weight % solution) which contains several compounds including the coupling agent and lubricants. Downstream, the filaments are then gathered and wound on to a cardboard mandrel to form the creel. The manufacturing process is capable of producing a nominal fibre diameter in the range 4-20 µm by controlling a number of processing parameters including the fibre haul-off rate [7]. Finally, the creels are dried in an oven prior to packaging.

### **2.3 Coupling agent**

The coupling agent is necessary because of the lack of chemical affinity of the E-glass surface with the epoxy or amine groups in the resin [12]. In other words, coupling agents are used to enable chemical bonding between the matrix and the surface of the glass fibres. Silane-based materials, generally referred to as organo-silanes are used commonly with reinforcing glass fibres. The principle of these coupling agents is that they have two different functional groups. The first group can react with the glass surface and/or with other molecules of

coupling agent. The second functional group reacts with the matrix creating covalent bonds [12].

## **2.4 Resin impregnation**

The first part of this review considers models that have been used to monitor the impregnation process; due to the large number of models reported in the literature to predict the impregnation process based on the Darcy equation, the parameters associated with this equation such as the permeability coefficient and the pressure gradient will be discussed. The second part of this review will describe some of the techniques that have used for monitoring the impregnation process and for calculating the permeability. Finally, the different approaches which have been used for fibre spreading will be described briefly and discussed.

### **2.4.1 Models to predict the behaviour of the impregnation process**

The impregnation process is dependent on a number of factors including the permeability of the preform. The modelling of this process has to take into consideration the anisotropy in the preform, the variability of the pores size and the uniformity of the binder concentration. These non-uniformities across the reinforcement will influence the way the matrix will permeate through it.

The motion of fluids can be described using the second degree differential equation of Navier-Stokes as shown in Equation 1,

$$\rho \cdot \left( \frac{\partial v}{\partial t} + v \cdot \nabla v \right) = -\nabla p + \mu \cdot \nabla^2 v + f \quad \text{Equation 1 [13]}$$

where  $\rho$  is the fluid viscosity,  $v$  is the flow velocity,  $\mu$  is the dynamic viscosity,  $t$  is time,  $p$  is the pressure, and  $f$  represents the forces (such as gravity) acting on the fluid. Assuming

incompressible Newtonian fluids with a Reynolds number much smaller than 1 (and hence the prevalence of viscous forces over the inertial), a simplified version of Equation 1 can be obtained, as shown in Equation 2.

$$\nabla p = \mu \cdot \nabla^2 v + f \quad \text{Equation 2 [13]}$$

Two different approaches have been used for modelling the flow of a resin through the preform [14]: the Stokes equation to describe the flow through the inter-tow region and the Darcy's equation to describe the intra-tow resin permeation.

Solving Stokes equation in a porous media requires the introduction of a structure at the pore-level as the input [14-16]. This is normally done by the use of virtual models and simplifications. The degree of complexity of the utilised geometrical models will depend on the available computational power.

Darcy's equation has been used by a number of researchers to model the impregnation process [16-18]. A common form of Darcy's equation is presented in Equation 3, where  $Q$  is the volumetric flow rate,  $K$  is the permeability,  $u$  is the velocity of the fluid,  $A$  is the cross-sectional area of the reinforcement,  $\mu$  is the dynamic viscosity of the fluid,  $L$  and  $\Delta p$  are the thickness and the correspondent pressure drop measured in the fluid movement direction through the reinforcement.

$$Q = K \cdot \frac{A}{\mu} \cdot \frac{\Delta p}{L} \rightarrow u = \frac{dL}{dt} = \frac{K}{\mu} \cdot \frac{\Delta p}{L} \quad \text{Equation 3 [16, 18]}$$

The integration of Equation 2 under certain conditions (considering the factor  $\Delta p/L$  constant during the impregnation process) gives Equation 4, which can be used to estimate the through-thickness impregnation of a fibre bundle [19]. The analysis of the different factors in

Equation 4 can be used for understanding the basic parameters that influence the impregnation process. For example (i) the viscosity of the matrix, (ii) the thickness of the fibre bundle, (iii) the pressure gradient, (iv) the viscosity/molecular weight of the liquid and (vii) the permeability of the reinforcement.

$$t = \frac{\mu}{2K} \cdot \frac{L^2}{\Delta P} \quad \text{Equation 4 [19]}$$

#### 2.4.1.1 Permeability coefficient

The permeability of a porous media describes how well a fluid can penetrate through the pores or the interstices of the preform. Since porous media are usually anisotropic, the permeability is expressed as a tensor, which allows the calculation of the resin flow in any direction. The permeability using an orthogonal coordinate system (XYZ) is given by Equation 5 [15].

$$K_{i,j} = \begin{bmatrix} k_{xx} & k_{xy} & k_{xz} \\ k_{yx} & k_{yy} & k_{yz} \\ k_{zx} & k_{zy} & k_{zz} \end{bmatrix} \quad \text{Equation 5 [15]}$$

Gebart [16] obtained empirical values for the permeability of the reinforcement using the Darcy's equation. He assumed that the fibres were parallel and packed symmetrically in a quadratic or hexagonal array. The values obtained for the permeability (K) had two components  $K_x$  and  $K_y$  (parallel and perpendicular to the fibres respectively) as shown in the Equation 6 and Equation 7 [16] respectively:

$$K_x = \frac{8R^2}{c} \cdot \frac{(1-V_f)^3}{V_f^2} \quad \text{Equation 6 [16]}$$

$$K_y = C_1 \cdot \left( \sqrt{\frac{V_{fmax}}{V_f}} - 1 \right)^{\frac{5}{2}} \cdot R^2 \quad \text{Equation 7 [16]}$$

where  $C_1$  and  $V_{fmax}$  depends on the fibre arrangement (quadratic or hexagonal),  $c$  is a constant which depends on the geometry and on the arrangement of the reinforcement,  $V_f$  is the fibre volume fraction,  $V_{fmax}$  is the maximum volume fraction (when the fibres are touching each other) and  $R$  is the radius of the filaments. A simulation of the axial and transverse permeability as a function of the fibre volume fraction using Equation 6 and Equation 7 is presented in Figure 3.

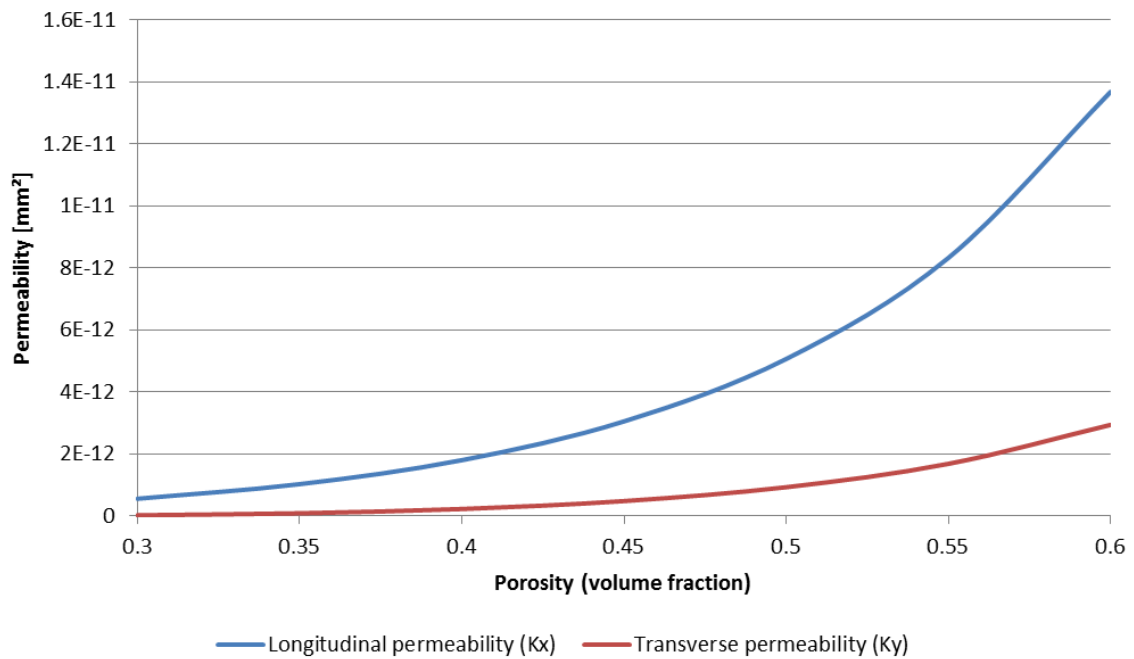


Figure 3 Longitudinal and transversal permeability obtained by Gebart's equation for different levels of porosity.

A selected summary of other relevant equations for modelling the axial and transverse permeability using the Darcy's equation are summarised in Table 1. These equations also assume a a symmetrical hexagonal or quadratic arrays of fibres [20, 21].

Table 1 Summary of selected models for axial and transverse permeability. Compiled from references [18, 22-24], where  $P_c$  is the capillary pressure,  $\varepsilon$  is the porosity,  $a_h$  is the gradient of velocity against distance and  $k$  is the Kozeny constant.

<i>Authors</i>	<i>Axial permeability</i>	<i>Transverse permeability</i>
Amico and Lekakou [24]	$K_x = \frac{\mu\varepsilon}{P_c} \cdot a_h$	—————
Carman-Kozeny [22]	$K_x = \frac{R^2}{4k} \cdot \frac{(1 - V_f)^3}{V_f^2}$	—————
Cai and Berdichevsky [23]	$K_x = \frac{R^2}{8V_f} \cdot \left[ \ln\left(\frac{1}{V_f^2}\right) - (3 - V_f)(1 - V_f) \right]$	$K_y = \frac{R^2}{8V_f} \cdot \left[ \ln\frac{1}{V_f} - \frac{1 - V_f^2}{1 + V_f^2} \right]$
Bruschke and Advani [18]	—————	$K_y = \frac{R^2}{3} \cdot \frac{(1 - I^2)^2}{I^3} \cdot \left( 3IB + \frac{I^2}{2} + 1 \right)^{-1}$ $I^2 = \frac{4}{\pi} V_f$ $B = \frac{\arctan\left(\sqrt{\frac{(1+I)}{(1-I)}}\right)}{\sqrt{1 - I^2}}$

With regard to the use of numerical methods and the Stokes equation, Chen *et al.* [25] solved the Stokes equation assuming a 2-D (the geometry was assumed not to change in the fibre direction) randomly oriented bundles generated by the Monte Carlo method. The axial flow for porosities from 0.45 to 0.90 in the volume fraction were investigated. The results were validated through comparison with theoretical predictions and previously published computational results. Nabovati, Llevelling and Sousa [15] used the lattice Boltzmann method for the fluid flow simulation and Darcy's equation to calculate the permeability of the medium in a 3-D computerised model. Differents levels of porosity with cylindrical fibres in random orientations were simulated to compute the permeability; their simulated data matched with their experimental data. Chen *et al.* [14] obtained the main permeability

components  $k_{xx}$ ,  $k_{yy}$  and  $k_{zz}$  across several geometrical patterns with different levels of porosity. They combined the computerised solution of Stokes's equation with the use of Darcy's equation. Their predicted results were in good agreement with published experimental data.

#### 2.4.1.2 Pressure gradient

The components of the pressure involved in a generic composite manufacturing process can be expressed by Equation 8 [26]:

$$P_t = P_m + P_g + P_v + P_c \quad \text{Equation 8}$$

where  $P_t$  is the total pressure,  $P_m$  represents the applied mechanical force,  $P_g$  introduces the effect of gravitational forces,  $P_v$  is the force exerted by the vacuum pressure and  $P_c$  is the capillary pressure. The mechanical and vacuum terms are known and depend on the process variables, whilst the gravitational pressure (normally much smaller than the other terms) depends on the density of the resin and the geometrical factors. Regarding the capillary pressure, in a low-pressure injection-base manufacturing processes, it may be a bigger contributor than the other three terms. For some fibres alignment configurations and low injection pressure in a fibrous media, the capillary pressure can be calculated using the Young-Laplace equation as shown in Equation 9.

$$P_c = \frac{4\sigma\cos\theta}{D_e} = \frac{F}{D_c} \cdot \frac{(1-e)}{e} \cdot \sigma \cdot \cos\theta \quad [Pa] \quad \text{Equation 9 [26]}$$

where  $F$  is a form factor depending on the fibres alignment and the flow direction,  $e$  is the porosity of the reinforcing fibrous preform,  $D_c$  is the diameter of single filament (in metres),

$D_e$  is the equivalent diameter of pores in a fibrous form (in metres),  $\sigma$  is the surface tension of the wetting fluid (in Pa.m) and  $\theta$  is the contact angle between the liquid and the solid.

In the particular case of an epoxy resin permeating through an unidirectional E-glass preform, Amico and Lekakou [24] stated the form factor “F” to be 4 or 2 for resin flow along or perpendicular to the fibres direction respectively. In addition, the value of the contact angle and the surface tension were calculated as  $57^\circ$  and 0.044 N/m.

#### **2.4.2 Impregnation monitoring**

The experiments carried out by previous researchers for obtaining data on the impregnation process are described briefly in this section. The techniques employed can be summarised as electrical, ultrasonic, optical fibre sensors, visual methods and a combination of them.

The changes in the electrical characteristics of the media as the capacitance or the resistivity is one of the methods used for monitoring the impregnation in resin transfer molding (RTM). Schab *et al.* [27] reported a discrete multi-point sensor system based on the change of the conductivity in each node as a sensing method. This methodology was improved by Luthy *et al.* and Matsuzaki *et al.* [28, 29] who designed a continuous measurement method based on the conductivity of two wires along the impregnation direction or on the use of an array of sensors mounted on a thin polyimide film as a bottom layer of the laminate respectively. Yenilmez and Sozer [30] used a grid of 50 sensors for measuring the changes in the capacitance produced by the resin, obtaining information on the flow of the resin and the curing of the matrix.

Another method reported for measuring permeability involved monitoring the resin flow into the reinforcement for a constant inlet pressure [26, 31]; this allows the application of Darcy’s

equation to deduce the through-thickness permeability. However, consideration was not given to the influence of anisotropy of the media on the flow characteristics of the resin.

Ultrasound-based techniques have been used to monitor the through-thickness impregnation of glass and carbon fibre fabrics [32, 33]. This involves monitoring the changes in the wave velocity as the resin permeates into the reinforcement.

Partially de-clad optical fibres have been used for monitoring the resin-front during impregnation by tracking the changes in the transmitted light intensity [34, 35]. Optical fibre sensors have also been used to monitor the variation of other physical parameters such as the reflection index [10, 36, 37], which also gives an indication of the evolution on the cross-linking process. Optical fibres sensors have also been combined with visual techniques for monitoring the impregnation process [38].

The use of Fourier transform near-infrared spectroscopy (FTIR) by a non-contact scanning methodology and statistical data analysis was demonstrated to be capable of monitoring prepreg manufacturing processes [39, 40]. Information on the resin content, volatile content or the degree of pre-curing of the material was extracted using different statistical methods.

Image analysis-based techniques have been used extensively for obtaining experimental data on the permeability of fabrics. The use of the cameras in conjunction with transparent mould covers have been reported for tracking the liquid-front of infused resin (under vacuum) through glass fabrics [41, 42]; the data obtained were used to calculate the permeability. Schell *et al.* [43] used a custom-designed transparent mould where a glass fibre tow was fixed in different orientations. Visual analysis of the liquid-front as a function of time was used for calculating the permeability in specified directions. Another approach for monitoring the through-thickness impregnation is the use of coiled tows and/or fabric tape [44] Here, the

resin was injected into the preform under a constant injection pressure and the evolution of the liquid-front monitored using a simple camera system. The micro-impregnation phenomena at the bundle level, using a single tow with a pigmented fluid were tracked using a CMOS camera mounted on a microscope [45].

Visual methods have been combined successfully for a complete study of the impregnation process. The use of a camera under controlled inlet pressure [38] using a transparent cover for the injection chamber and a 3-D array of intensity based optical fibre sensors, allowed the monitoring of the X-Y flow-front of the resin on the surface and the evolution through the thickness. Finally, an approach was developed using a combination of thermocouples and image analysis [46]. Thermocouples were installed for temperature-control purposes during the resin permeation process; image analysis was used to monitor the changes in the light diffraction by the projection of a fringe pattern on the laminate surface.

## **2.5 Fibre spreading**

A large number of techniques have been reported in the patent literature for spreading the filaments in a fibre bundle [47]. These methods can be divided into four general categories: mechanical, electrostatic, vibration/acoustic and pneumatic/vacuum methods.

Mechanical-based techniques generally involve the use of pins, convex rollers and systems of rollers for spreading the fibres [48-51]. These methods demonstrate good spreading but excessive angles or contact points can cause fibre damage. A basic mechanism for the spreading of fibre bundles was recently proposed by Irfan *et al.* [6].

In the electrostatic methods, an electrical potential is applied to fibre bundles where the charge on the individual filaments results in its separation [52-55]. A limitation of

electrostatic-based techniques for spreading the filaments is that they are not suitable for use with inflammable resins and solvents. Another disadvantage of these techniques is that the concentration of the binder on the fibre bundle can have a significant influence.

The use of vibrations at specified frequencies and amplitudes has been reported to be able to achieve some degree of spreading [56-58]. Vibration-based techniques will not be considered any further in this report as they are not applicable to fibre bundles with high binder contents.

Finally, there are some technological developments that are well described in some patents considering fibre spreading using pneumatic and vacuum methods [59-61]. All of these techniques have in common the use of gas jet systems or the change in the pressure in order to achieve spreading of the fibres. The study reported by Newell [62] is of special interest, where a high degree of spreading of the fibres was achieved by combining Venturi pipes with pressure rolls at the beginning and at the end of the spreading process. However, airborne contamination is a potential disadvantage of this technique.

## 3 Experimental

### 3.1 Impregnation monitoring

The technique that has been developed by the author involves the use of a photo-curable thermosetting resin to enable it to be “frozen” at some point as it impregnates the fibre bundle for software calibration purposes. A pair of USB (Universal Serial Bus) microscopes equipped with a 2 Megapixel CMOS lens (interpolated) was used to track the flow-front of the resin at 1 Hz, and the data were logged in the computer using custom-written software. A rig was designed and built for securing the two CMOS-microscopes in position (above and below the fibre bundle). The same rig was also used to accommodate a micro-pipette in the required position; the micro-pipette was used to dispense a drop of a photo-curable resin of a known volume on the surface of the fibre bundle. A light-proof enclosure was constructed from cardboard to isolate the cameras and the fibre bundle from external light. This therefore dictated the need for a lighting system to be designed and built to enable the “motion” of the photo-curable resin on the fibre surface to be tracked in real-time. A LED lightning system was designed and constructed.

#### 3.1.1 Materials

##### 3.1.1.1 Resin system

The photo-curable resin used in this study was NOA63 (Norland Co., USA). It was cross-linked or cured using a UV light source, model UV75 Light (Thorlabs, UK). The emission wavelength was in the range of 350-500 nm. Since the UV resin system was optically clear, it was not easy to use the software to track the flow-front using the standard vision system. Thus

to solve this problem, a red pigment Araldite Colouring Paste (Huntsman, UK) was used to enhance the contrast between the resin and the fibre. However, the nature of the pigment in concentration as low as 0.5 weight % was found to have an influence on the cure time and the viscosity. Therefore, the viscosity of the photo-curable resin, with and without the red pigment was determined using a parallel-plate rheometer model Ares (Rheometric Scientific, USA).

A drop of the photo-cure resin was dispensed from a height of 2 cm at an angle of 30° to the horizontal plane via a mechanical micro-pipette model Mline (Biohit, UK) on to the centre of the E-glass fibre bundle. In a separate experiment the mass of each drop dispensed was measured using a four-digit analytical balance model PA214 (Ohaus, UK).

The drop of resin on the fibre bundle was permitted to permeate into the fibre for 200 seconds. The flow-front of the resin over the top of the bundle was monitored using the upper CMOS-camera, and the through-thickness impregnation was detected and quantified using the bottom CMOS-Camera. The laboratory temperature was in the range of 18-23 °C.

### ***3.1.1.2 Fibres***

The fibres used in this study were as-received and spread Hybon 2026 Tex 2400 (PPG Industries, UK) and as-received fibres Advantex T30 R25H2400 (Owens Corning, UK). For the PPG fibres, in order to obtain data for different zones of the creel, it was segmented into nine clusters representing the relative height (top, middle or bottom) and the layer (internal, centre and external layers), as shown in Figure 4.

The three layers were defined as cylinders with their external and internal diameters as follows: external layer from the creel nominal exterior diameter to 220 mm of diameter, the

central layer from 220 mm to 175 mm of diameter, and the internal layer from 175 mm to the nominal internal diameter of the creel. In addition and as explained above, three zones were defined according to the relative height from the bottom surface of the creel: bottom (first 25% of the height of the creel), middle (from the first 25% to the 75% of the total height of the creel) and top (last 25% of the height of the creel).

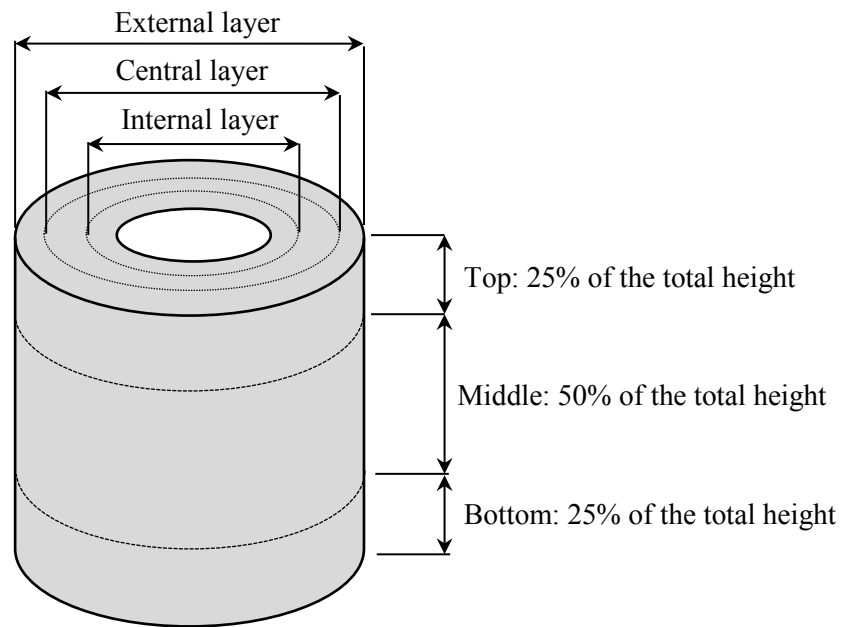


Figure 4 Definition of the relative positions of the creel: external layer top/medium/bottom, central layer top/medium/bottom and internal layer top/medium/bottom.

### 3.1.1.3 Camera stand and the lightning system

A schematic illustration of the rig for holding the two CMOS-microscope cameras is presented in Figure 5. It consists of two vertical aluminium rods where two rectangular platforms were positioned to house the cameras. In addition, three further support platforms were located on the rig: one in the middle for supporting the fibre bundle, and one upper and lower platforms to hold the lightning system.

Significant experimentation was used to identify the optimum lighting conditions. This was necessary in order to obtain repeatable and consistent results.

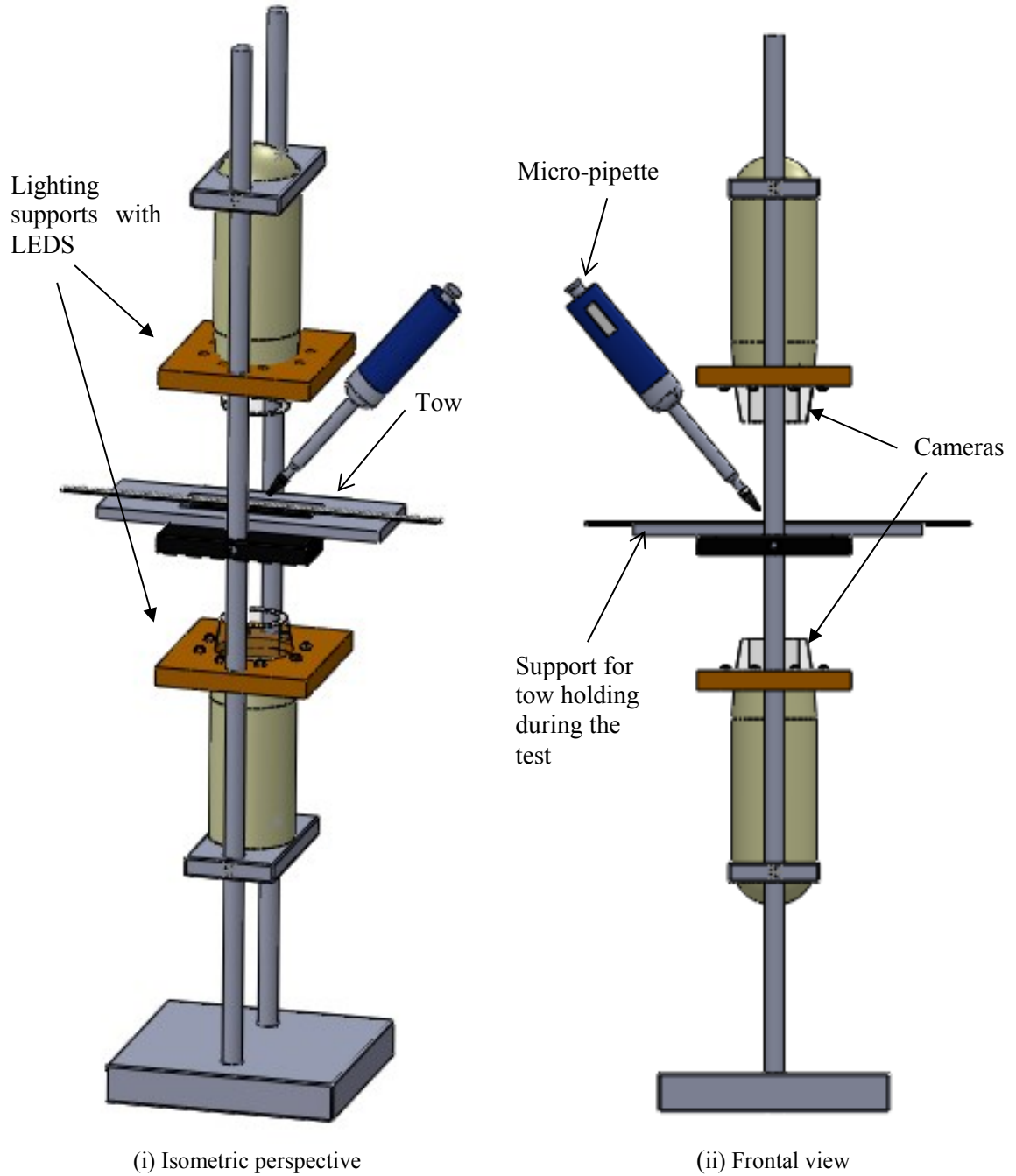


Figure 5 Schematic illustration of an isometric perspective (a) and a frontal view (b) showing the fixtures for housing the two CMOS-microscope cameras, the fibre bundle and the LED-based illumination system.

An enclosure was built from cardboard to isolate the cameras and the sample from external light. The inside of the enclosure was covered with a black mat surface using black cardboard. A number of off-the-shelf lighting systems were evaluated to illuminate the top and the bottom surfaces of the fibre bundle. However, these illumination sources were found to be unsuitable for the following reasons: (i) it was necessary to have a broad range of intensity of illumination for calibrating the system; (ii) difficulty in sourcing a illumination source specifically for the fixture shown in Figure 5; and (iii) ensuring that the dimensions of the lighting assemblies did not interfered with the introduction of the photo-curable resin via the micro-pipette. Therefore, it was necessary to develop an appropriate lighting to enable the resin to be tracked by the CMOS-microscopes. Since it was necessary to ensure that the lighting system did not heat up the resin, a LED lightning system with an adjustable luminance was designed and constructed. Two platforms were constructed and installed as illustrated in Figure 5. Each platform contained an array of eight LEDs equally spaced around a circumference of diameter 50 mm. The LED diodes (Seoul Semiconductor, RS, UK) emitted white light, and had a diameter of 5 mm with 15° of beam-angle. Each of the platforms was controlled independently via custom-built circuits. The light intensity in each platform was adjustable independently through a potentiometer. This enabled uniform illumination of the top and bottom surfaces of the fibre bundle during the impregnation experiments. After several trials using different light intensities, the optimum lighting conditions were found that corresponded to the minimum intensity level in the top LED platform (potentiometer setting 0) and with a higher intensity in the bottom LED platform (potentiometer position number 6).

A magnified perspective of the platform is shown in Figure 6. With reference to the micro-pipette, an orifice was introduced on one side of the light-tight enclosure and the CMOS

camera was used to position the tip of the micro-pipette on the centre of the fibre bundle as required. This enabled the resin to be delivered from the exterior of the enclosure without altering the lighting conditions.

The relative positions of the various devices were fixed to enable the experiments to be repeated under identical conditions.

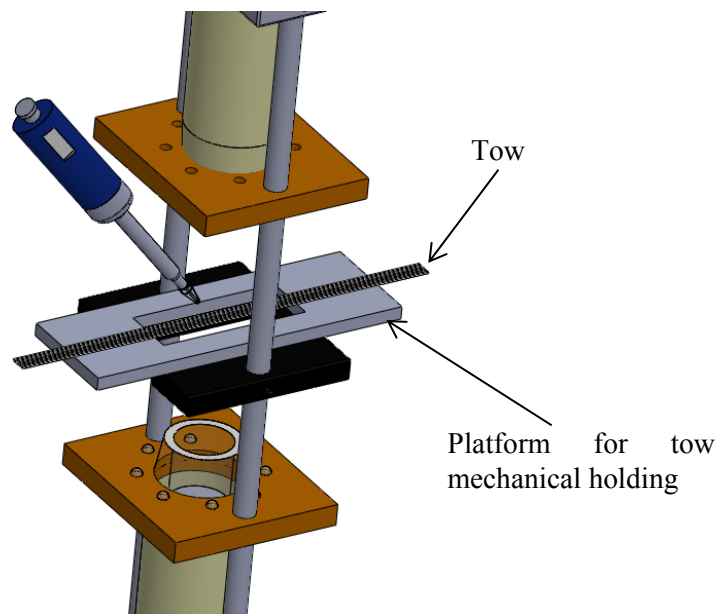


Figure 6 A magnified view of the platform for housing the fibre bundle, imaging and illuminating systems for the impregnation studies.

#### ***3.1.1.4 Software to enable real-time monitoring of impregnation, and software calibration***

Custom-written LabVIEW-based software was developed and used to track the flow-front of the resin using the USB microscopes as shown in Figure 6. The camera positioned on the top of the fibre bundle was used to monitor the flow of the resin in the axial and transverse directions and to quantify the evolution of the impregnated area. The camera placed at the opposite face was used to infer the through-thickness impregnation.

The software was capable of operating at 1 Hz per CMOS camera and this was used to track the fluid-front in the x, y and through-thickness directions. A screen-shot of the software user interface is presented in Figure 7.

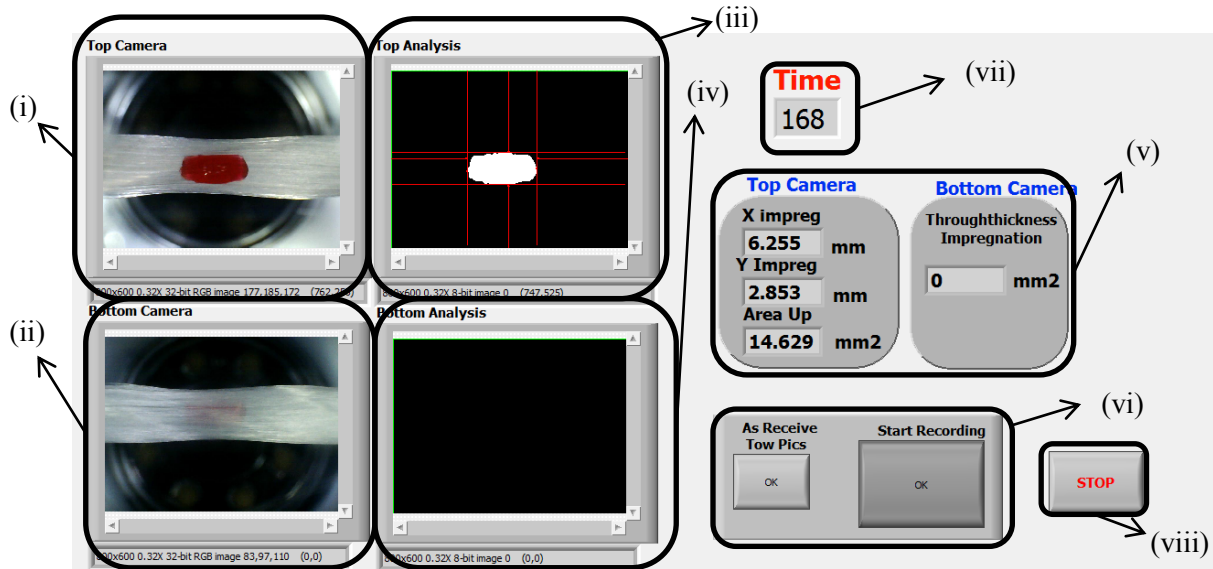


Figure 7 Screen-shot depicting the user interface for the two CMOS cameras when (i) and (ii) show the top and bottom real image respectively, and (iii) and (iv) show the top and bottom image (again respectively) after the image analysis. The calculated values are inserted in the (v), and the controls shown in (vi) allows us to take a picture of the dry tows and to start the test. Finally (vii) shows the remaining test time and (viii) is the test stop.

Before starting the test, it is necessary to input the following relevant data in a drop-down menu: (a) test time (200 seconds); (b) file name where the data will be logged; and (c) other relevant information such as fibre type, test temperature and relative humidity.

The results of the test are stored in a file along with the temperature and humidity, time and date, test time, iteration number and the iteration time. In addition, all the acquired images are stored in individual files of 24-bits RGB (picture representation methodology, using arrays with the combinations of the primary colours red, green and blue) with a resolution of 800x600 pixels, creating a library with all the images of each test.

### 3.1.1.5 Calibration of the cameras

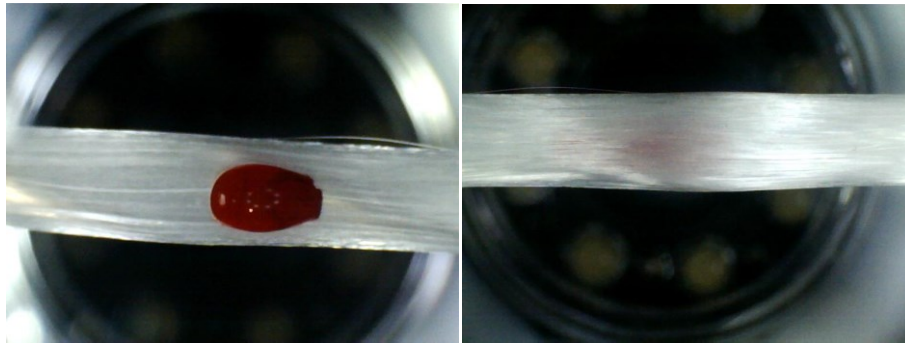
The cameras were calibrated using a 1 mm square-grid graph paper and the “Points Coordinate Calibration” method [63]. It involves using at least 4-points, one for each corner of the image, with known relative distances (measured using a digital calliper). The introduction of these specified distances allows the system to correct for any camera angle distortion and to correlate the pixels of the images to quantifiable units. After the calibration process, tests were performed to calculate the errors associated with the measurements using two different objects: a flat metallic disc of 6.45 mm of diameter and a plastic cylinder with a width of 5.22 mm. The test method involved comparing the measurements in different sections of each object obtained via the digital calliper (the same procedure was used for the calibration of the cameras) and by the camera system. The results are summarised in Table 2 where the difference between the measurements obtained by the digital calliper and the camera system are lower than 0.1 mm with a small variability in the readings as demonstrated by the relatively low standard deviation.

Table 2 Summary of data obtained for from the digital calliper and the cameras using “reference” objects. Table (a) shows the data obtained using a metallic disc and (b) a plastic cylinder.

(a) Metallic disc - Diameter [mm]				(b) Plastic Cylinder - Width [mm]			
<i>Test</i>	<i>Calliper</i>	<i>Top Camera</i>	<i>Bottom Camera</i>	<i>Test</i>	<i>Calliper</i>	<i>Top Camera</i>	<i>Bottom Camera</i>
<b>1</b>	6.46	6.44	6.53	<b>1</b>	5.22	5.32	5.25
<b>2</b>	6.46	6.43	6.52	<b>2</b>	5.22	5.32	5.27
<b>3</b>	6.44	6.44	6.53	<b>3</b>	5.23	5.33	5.25
<b>4</b>	6.45	6.44	6.52	<b>4</b>	5.24	5.32	5.26
<b>5</b>	6.47	6.44	6.53	<b>5</b>	5.23	5.32	5.28
<b>Average</b>	6.456	6.438	6.526	<b>Average</b>	5.228	5.322	5.262
<b>St. Dev.</b>	0.0114	0.0045	0.0055	<b>St. Dev.</b>	0.0084	0.0045	0.0130

### 3.1.1.6 Image analysis process description

The basis of an artificial vision system is the analysis and correlation between the image and the pixels, and the spectral analysis for distinguishing, analysing or measuring physical objects. In the current case, the requirement was to identify the area of a coloured (red) resin against a white background of the E-glass fibres or any other object that appear in the image. An example of typical images of the resin as viewed by the top and bottom cameras is presented in Figure 8 (i) and (ii) respectively.



(i): Image capture by the top camera.

(ii): Image captured by the bottom camera.

Figure 8 Examples of typical images captured by the: (i) top; and (ii) bottom CMOS cameras.

#### 3.1.1.6.1 Upper CMOS camera

Whilst it was relatively straightforward to track the resin-front in the initial stages of the impregnation process, it was found that after a time (dependant on the tow architecture but normally after 30-40 seconds) the flow of the resin decreased and the contrast in the perimeter or the resin on the surface of the fibre bundle becomes diffused. This phenomenon was caused by the reduction of the resin “height” of the resin as it permeates in the axial, transverse and through-thickness directions as a function of time. The net effect of this is a decrease in the

contrast between the “red” resin and the white tow along the perimeter or boundary. The typical image of a diffused resin-front is shown in Figure 9.

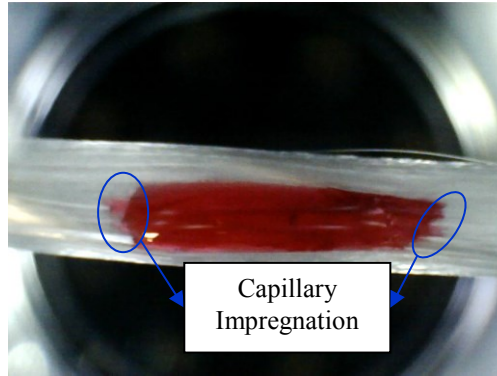


Figure 9 Detail of axial or capillary impregnation recorded by the top USB microscope.

After several trials, the following algorithm was developed:

- a. Image subtraction “A-B”: This is similar to an arithmetical subtraction but it is undertaken pixel-by-pixel using as minuend and subtrahend for each individual operation pixels of identical positions in image “A” and in image “B”; this operation will conclude when all the pixels have been used. For each test, “A” is always the image of the dry tow taken just before the start of the experiment and B is the image taken in each iteration. Since the images are 24-bit colour RGB, which consists in three superposed planes of 8-bits each (red, green and blue), this operation is repeated three times (the red plane from the image A minus red plane of the image B, and the same for the green and blue planes). Due to fact that the coding of each plane is done with 8 bits (8 bits each for red, 8 for green and 8 for blue, which are the 24 bits of the image), this arithmetic operation will result in a “new” image assembled of three planes of RGB; here the values of the pixels in each of planes range from 0 (black or no colour) to 255 (saturation). In the subtraction process, a non-zero value is obtained where the resin is detected, giving a clear and stable

image of the geometry of the drop. An illustration of the subtraction process is shown in the Figure 10.

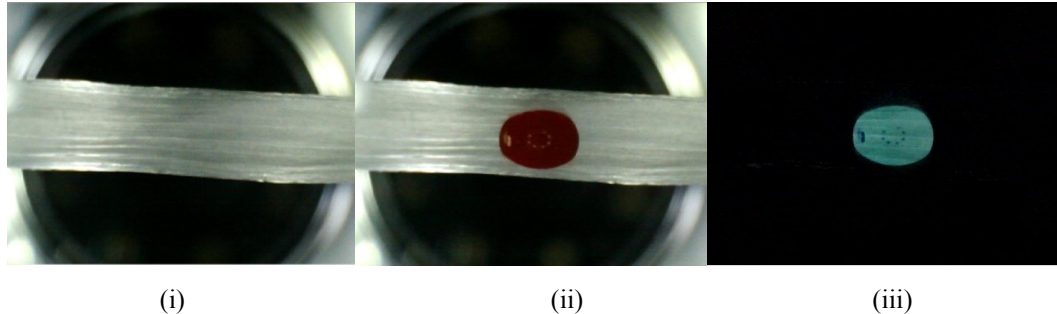


Figure 10 Illustration of the image-subtracting process. Image of the: (i) as-received bundle; (ii) resin on the bundle; (iii) computer-generated image after the subtraction process which isolates the resin drop.

- b. The second step is the conversion of the colour image from 24-bits RGB (8 for each one of the three basic colours) to an 8-bit grey scale image (just one colour, from 0 – black – to 255 – white, having different tones of grey in the middle) extracting the HSV plane (representation of the hue, the saturation and the brightness in cylindrical coordinates). The reason for this is because the analysis in grey scale is easier and more robust.
- c. The third step involves the definition of the boundary of the resin drop. The software was able to discriminate the area of the drop of the resin (different levels of grey) from the background (black) using threshold levels from 30 to 255 (the pixels with values from 0 to 29 covered the different tonalities of “black” from the background, meanwhile values above 29 contained areas with resin). After applying the threshold, the image consisted of pixels with two possible values: white (area with resin) or black (background); this is illustrated in Figure 11.
- d. Finally, the black and white image was used for measuring the length, width and area, the scale factor was applied (in other words, the scaling factor for the number of pixels required to define 1 mm) and the data were logged to a file.

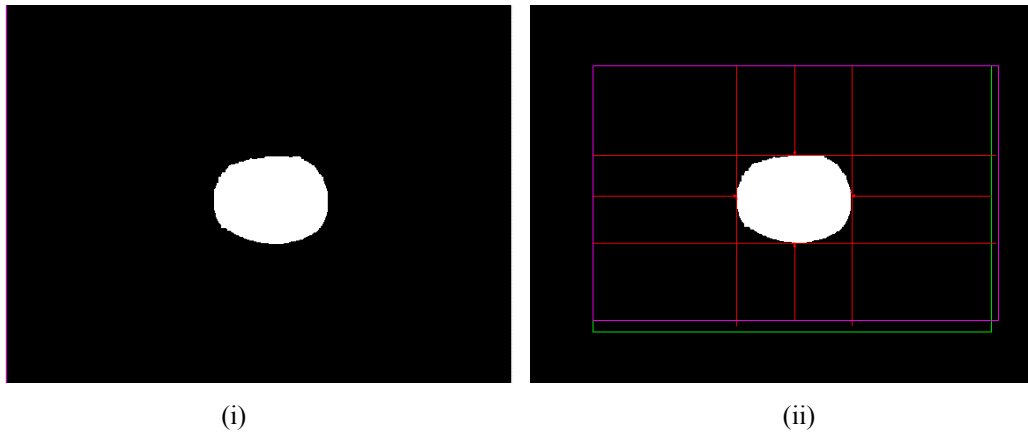


Figure 11 Illustration of the software-based extraction of the “wet” area and analysis: (i) black and white image of the resin drop; (ii) software-based computation process.

### 3.1.1.6.2 Bottom CMOS camera

Due to the poor definition of the resin-front as it diffuses through the fibre bundle, the detection of the through-thickness impregnation via the CMOS-microscope was far more challenging.

A series of experiments were conducted where the lightning conditions, image conditioning and the threshold levels were changed in a systematic manner. Finally, an optimal algorithm was developed.

- a. Image subtraction: The procedure described in Section 3.1.1.6.1 was performed with the result showed in the Figure 12.
- b. Brightness: The contrast enhancement was adjusted to 70%. This gave a clearer image when it was converted to the grey scale.
- c. Grey scale conversion: This was done extracting the HSV plane and converting the image from 24 to 8-bits, as described in 3.1.1.6.1.b.
- d. Boundary definition, as detailed in section 3.1.1.6.1.c, was done applying a threshold level on the image. The optimum level was found to be in the range from 40 to 255.

- e. Area measuring using the black and white image, applying the scale factor to convert from pixels to mm<sup>2</sup>.
- f. Logging the results to a file.

Figure 12 shows the image before and after manipulation using the procedures described above.

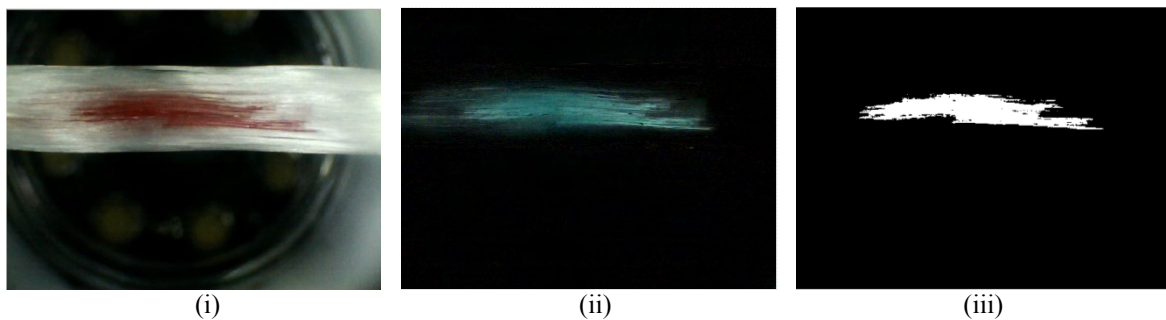


Figure 12 Images captured from the camera positioned at the bottom and the subsequent image processing routines: (i) a typical image captured from the camera positioned below the bundle; (ii) shows the image after the subtraction operation; and (iii) is the result after image processing and the threshold application.

### 3.1.2 Monitoring fibre spreading

The instrumented rig presented in Figure 13 was designed, constructed and assembled for monitoring the degree of fibre spreading. It consisted of an articulated platform where two load-cells were installed. The load-cells allow the monitoring of the tension in the tow and the changes in the pressure applied by a pneumatic cylinder over the tow via two rollers. In addition, two CMOS cameras were installed for monitoring the width of the tow automatically before and after the tow passed through the rig.

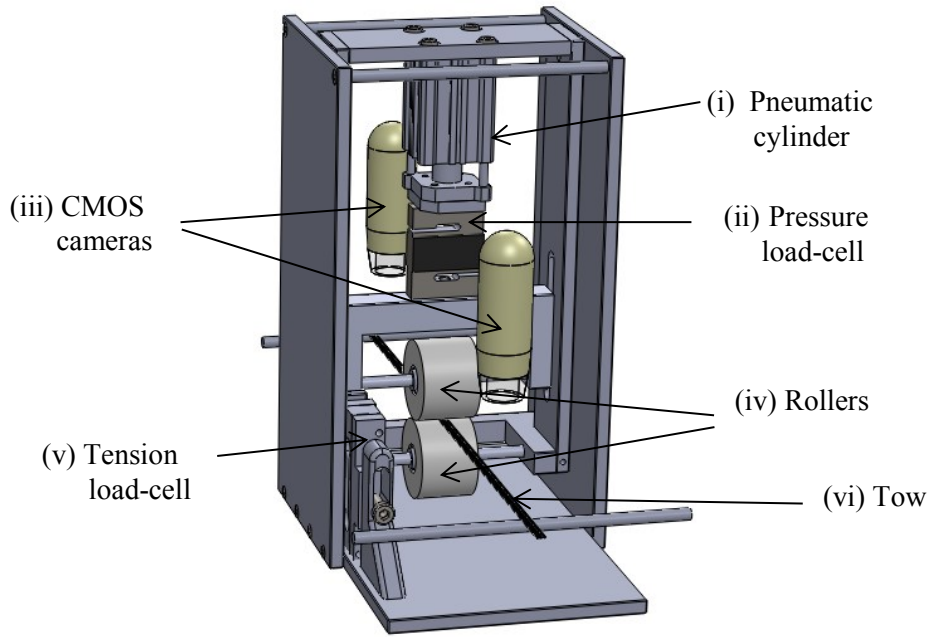


Figure 13 Schematic illustration of the rig that was designed and built to study the various parameters that influence the degree of fibre spreading.

The rig was articulated using an external frame which held an internal mobile platform. The external frame consisted of a floor-plate with a frame and an axle which is used for attaching the internal platform, and it provided a facility for the internal platform to be swung, as illustrated in Figure 14.

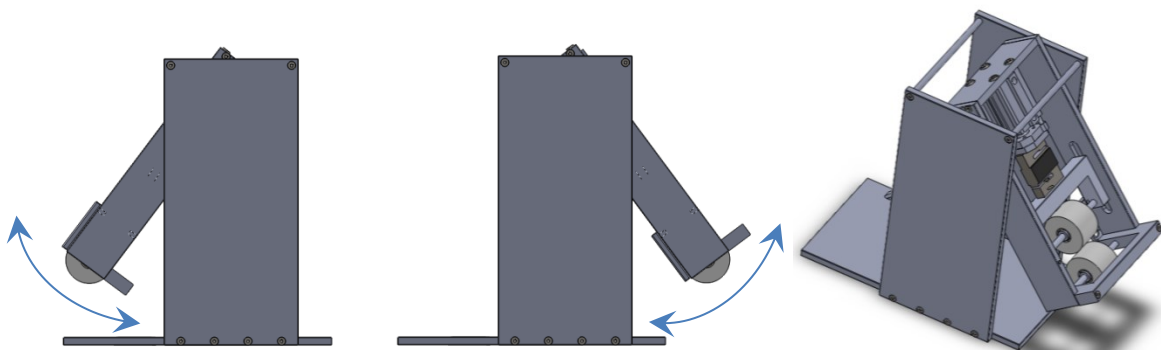
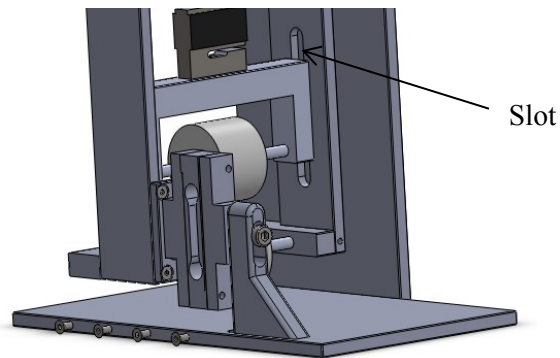


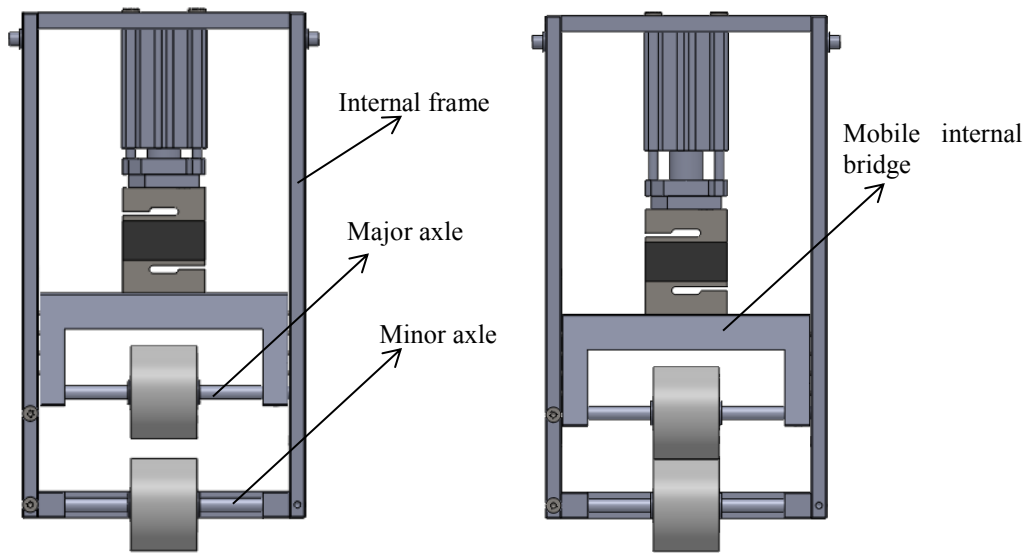
Figure 14 Schematic illustration depicting the adjustability of the inner frame.

In order to lock this relative movement, this internal platform was secured to the external platform floor-plate using a support that was attached to a 3 kg load-cell (model Tede-

Huntleigh 1022); this mechanism which is detailed in Figure 15 (i), allows the tension in the tow to be monitored between the haul-off equipment and pair of “nip” rollers. The data from the load-cell were acquired and digitised using a channel of a National Instruments DAQ (digital-to-analogue converter) card model NI-9219. This device is also used to provide a stable excitation voltage to the load-cell.



(i) Detail of the load-cell and mechanism for measuring the tension in the tow.



(ii) Cylinder in the “rest” position.

(iii) Cylinder pressurised position.

Figure 15 Schematic illustration of the construction of the internal frame showing the adjustability of the pair of rollers. (i) Representation of the slots in the internal frame for guiding the internal bridge and the 3 kg load-cell which attach the internal platform to the floor of the external platform. Illustrations (ii) and (iii) show the pneumatic cylinder in inactive and active positions respectively.

The internal frame was used for attaching the pneumatic cylinder and the rollers to enable a defined pressure to be applied to the tow. Figure 15 shows how the cylinder was attached to

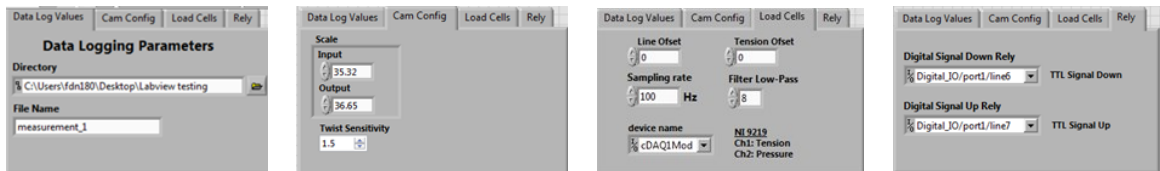
the internal platform: the minor axle was fixed horizontally and the major axle was attached to the mobile internal bridge. The mobile bridge has two nylon plates enclosed in the slots machined in the internal frame; this allowed its position in the vertical plane to be maintained while it was translated up or down. The bridge was attached to the pneumatic cylinder via a 50 kg Tedeo-Huntleigh 614 grade G load-cell and custom-designed aluminium adaptors. A channel on the previously mentioned NI 9219 DAQ card was used for reading the signals and for exciting the load-cell. The cylinder was initially loaded using a 5-ports solenoid valve (model SMC SY5320-5DZ-01F-Q-S) where a TTL digital signal was generated from a USB I/O device from National Instruments (model NI USB-6501). This device was able to manage the 24-volts dc of the valve using a series of two relays: the first relay was operated at 5-volts and was used for energising the second relay, which managed the 5-port solenoid valve. After the initial pressure loading, the valve was closed and the variations of the force in the 50 kg load-cell monitored. The sensing principle was that depending on the “thickness” of the tow being traversed between the rollers, the changes in the thickness of the bundle will be translated to the cylinder via the load-cell. When the top-roller is pushed up, since the volume of air in the cylinder is constant, the pressure in the cylinder housing will be increased and consequently the force recorded by load-cell will increase. When the shaft of the cylinder moves down (corresponding to decrease in the thickness of the tow), the pressure in the cylinder decreases and hence, the force recorded by the load-cell decreases.

Customised software was designed and written using LabVIEW for: (i) controlling the pneumatic cylinder; (ii) establishing the initial pressure setup; (iii) collecting the data from the load-cells; (iv) extracting the images from the cameras; and (v) logging the data in a file. Due to the technical limitations of the camera, the data from the load-cells were acquired at 100 Hz but the image analysis was limited to 5 Hz. The data generated in these tests were written

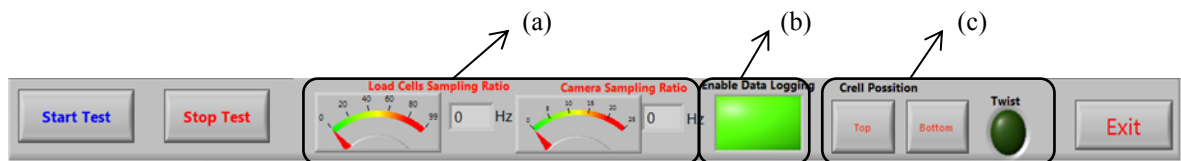
automatically to a file. Since the sampling rates for the load-cells and for the cameras were different, the data were time-stamped.



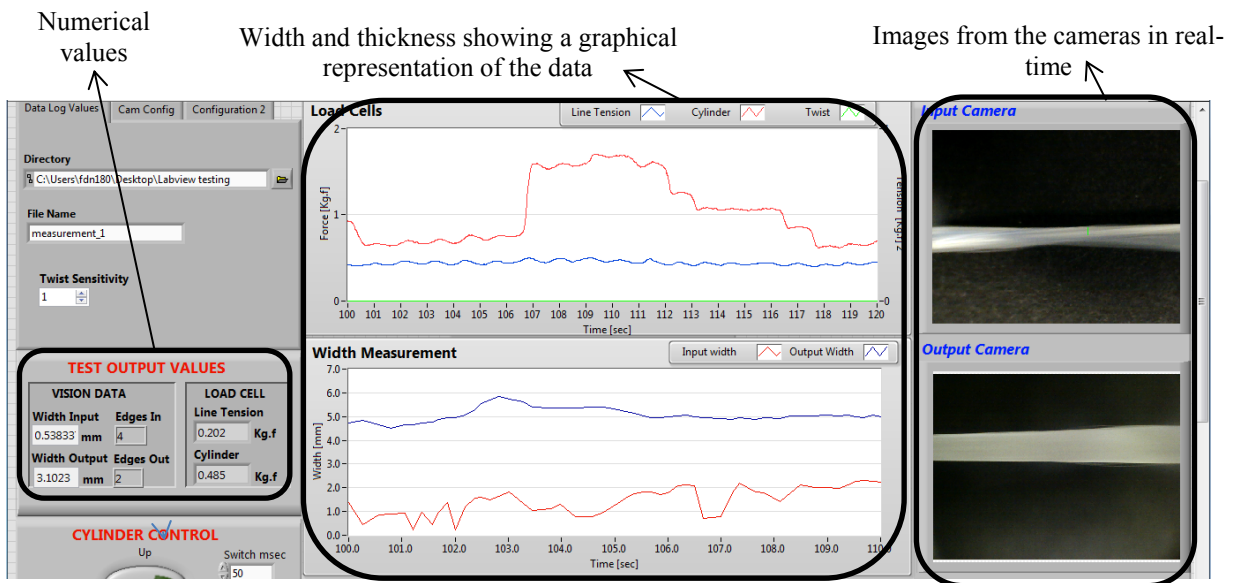
(i) Screen-shot of the control display panel.



(ii) Details of the menus and the corresponding tabs for configuration purposes.



(iii) Bottom screen-shot illustrating the: (a) average sampling rate indicators; (b) controls for starting the data logging; (c) data input in the measurement file to specify the position of the tow within the creel.



(iv) Area for data visualisation

Figure 16 Details of the software interface: (i) general overview and location of the three main areas (tab control with the configuration menus, bottom area and data visualisation); (ii) Different options which can be found in the tab menu (iii) Bottom area with sampling rate indicator and test start/stop, data logging and zone of the creel under testing; (iv) Data visualisation area.

### 3.1.2.1 Image analysis and measurement system

A pair of USB microscopes equipped with 2 Megapixel CMOS lens (interpolated) was used to measure the thickness of the tow before and after passing between the pair of rollers as illustrated in Figure 17.

The positions of the cameras were secured using clamps and fittings. The relative distances from the tow to the two cameras, a key factor to ensure repetitive measurements, was fixed using aluminium bars. The details of this assembly can be seen in Figure 17. The readings of the cameras were found highly dependent on the external light conditions, and due to necessity for visual representation of the image it was not possible to use a physical enclosure to isolate the system. In order to address this problem, a black surface was positioned below

the tow to minimise reflections from metallic surfaces and to enhance the contrast (white over black).

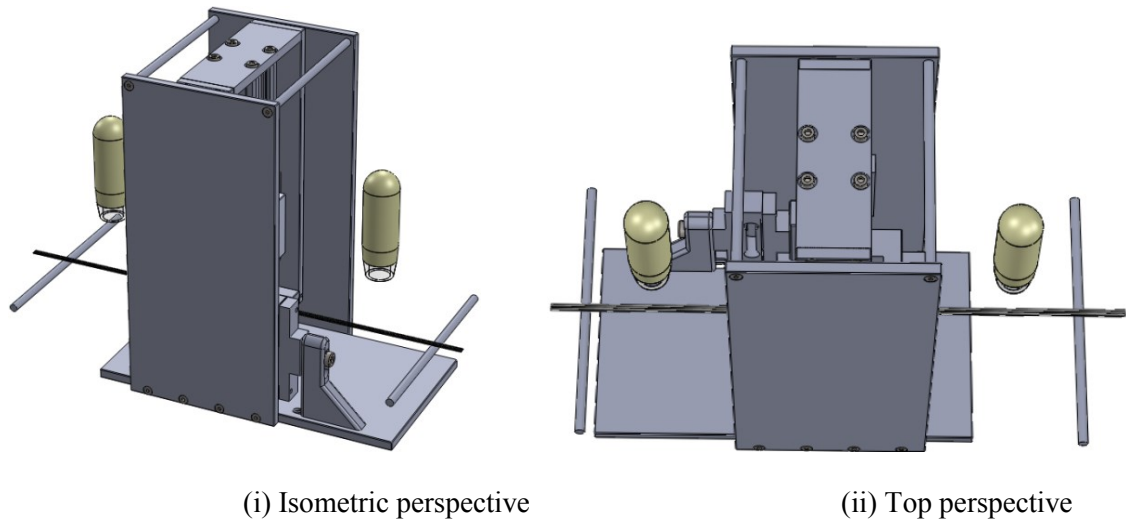


Figure 17 Detail of the relative positions of the two cameras on the rig, where the different clamps used with the cameras have been removed for simplification purposes: (i) isometric perspective where the tow moves from left-to-right; and (ii) top view.

With reference to the customised software, in each vision measurement iteration the computer acquires one RGB 32-bit 800x600 pixels image from each camera for analysis. The details of the algorithm applied for the width measurement of the tow are detailed below.

### ***3.1.2.2 Tow width measurement algorithm***

The algorithm designed for the tow width measurements was based on the edge detection method. Here, the changes in the pixels across a defined line (perpendicular to the tow) are analysed as shown in Figure 18. In order to improve the precision and reproducibility of the measurement (dependant on the intensity of the external light), the software allows the operator to configure several parameters to increase the accuracy of the readings. For example,

- Kernel size: this is the size of the matrix for the convolution Kernel or filtering for the image. It allows the the edges to be detected more clearly [64].
- Width: this defines the number of pixels averaged perpendicularly to the analysis direction for computing the edge profile strength at each point along the detection line [64-66].
- Interpolation type: zero order, bi-linear or bilinear fixed [64].
- Minimum edge strength: here the edge is located when a peak that is higher than the fixed minimum level is detected.

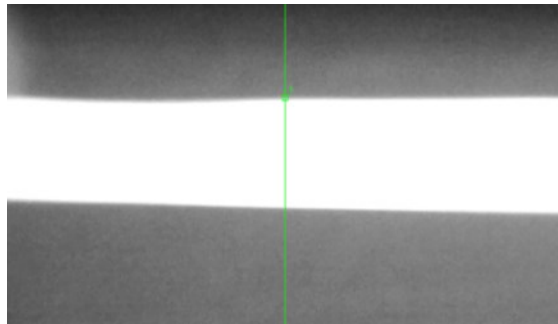


Figure 18 Edges location perpendicular to the tow movement direction; the detection line is indicated.

It was found by trial-and-error that the following values were the most appropriate for the lighting conditions in the laboratory where the experiments were carried out: “kernel size” = 13, “width” = 7 and zero order interpolation with minimum edge strengths of 30.

## 4 Results and discussion

### 4.1 Impregnation monitoring

#### 4.1.1 UV resin viscosity

The viscosity of the UV-curable resin (NOA63) was measured as a function of temperature, with and without the red pigment using a parallel-plate rheometer. It was observed that the pigmented resin (0.5 in wt %) had a slightly higher viscosity than the as-received resin. Since the room temperature in the rheometer laboratory was always above 20 °C it was not possible to cover the interval from 18 to 30 °C. Therefore a second order polynomial regression was applied with an  $R^2$  higher than 0.99 to extrapolate the data. The results of the two datasets (as-received and pigmented resin) are presented in Figure 19.

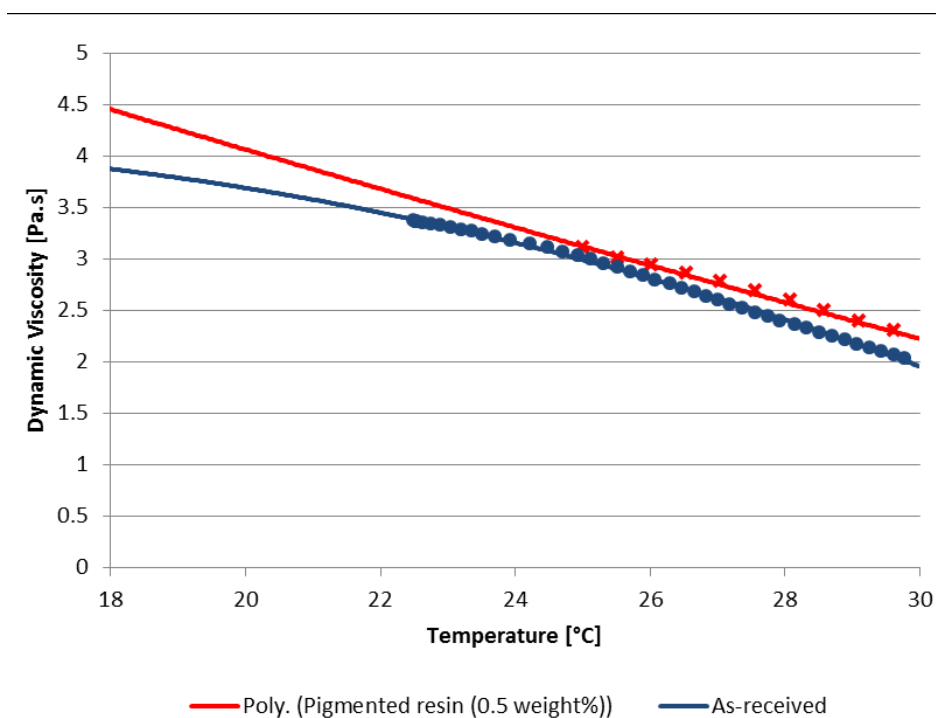


Figure 19 Dynamic viscosity profiles for the NOA63 photo-curable resin as a function of temperature. The data presented are for the as-received and pigmented photo-curable resin (0.5 weight %).

#### 4.1.2 Calibration of the dispensed UV resin

Since the volume of the resin used in each test was a critical parameter for the impregnation studies, the mass of resin dispensed by the micro-pipette was quantified ten times using a high precision scale. These experiments were carried out over a period of 5 minutes where the temperature in the laboratory was  $21 \pm 1$  °C. The results are shown in Table 3. Assuming a normal distribution, 68% of the data were within  $\pm\sigma$ , and the 95% within  $\pm 2\sigma$  where  $\sigma$  is the standard deviation.

Table 3 Weight of each drop of the pigmented resin dispensed from the micro-pipette.

Test	Weight [g]
1	0.01039
2	0.00987
3	0.01036
4	0.0102
5	0.01015
6	0.01118
7	0.01151
8	0.01078
9	0.01022
10	0.00985

Analysing the data in Table 3, it is seen that the average weight is 0.01045 g with a standard deviation of 0.00052 g. Applying the  $2\sigma$  criteria, the average weight of the drop of resin dispensed by the pipette is  $0.010 \text{ g} \pm 10\%$ . In other words, in 95% of the cases, the weight of the resin drop will be between 0.009 and 0.011 g.

#### 4.1.3 Measurement methodology validation and maximum error definition

The impregnation process is a dynamic process where the profile of the drop of resin on the fibre bundle is changing constantly. Thus it was necessary to develop a method to “freeze” the

impregnation process to enable correlation to be established between the impregnation profile in the three planes and the analysis obtained by the software.

A number of options were considered to freeze the spatial locations of the resin-front including lowering the temperature and using a fast-curable resin. It was decided that the photo-curable resin was capable of providing a practical solution. Hence, a UV photo-curable resin (NOA63, Thorlabs) was selected for two reasons: (i) its viscosity (3.5 Pa.s) was close to a commercial-available epoxy/amine resin system that is used in the research group at the University of Birmingham; (ii) it permitted the liquid-fronts to be frozen within the first 20 seconds of the application of the UV light; and (iii) it was possible to pigment the resin to enhance the contrast between the resin and the E-glass fibre bundle. The process that was adopted for the validation of the software and the maximum error calculations were conducted using six different experiments for each of the two cameras; details as follows.

- (i) The tow was fixed to the test fixture as shown previously in Figure 5 and Figure 6. Images were secured using the two cameras and these served as the “reference” for the prevailing lighting conditions.
- (ii) A drop of the UV-curable resin was dispensed on to the top-surface of the tow using the procedure described in Section 3.1.1.1. The sample was allowed to impregnate for a specified time whilst the software was operational, until a specified level of through-thickness impregnation was attained. The tip of the UV-light source was positioned at a distance of 20 and 30 mm from the bottom and the top-face of the tow respectively. The bottom and the top-faces were irradiated for two minutes and one minute respectively.
- (iii) After the bottom and the top faces of the tow were irradiated (to freeze the liquid front), the software was activated and the images of the two surfaces were recorded. The

software routine was used to analyse and compare this and the previous pairs of reference images.

(iv) An alternative manual analysis of the images was conducted using the following procedure:

- a. Top microscope: due to the fact that the resin was dropped on this side of the tow, the evolution of the resin front was clearly distinguished by the observation of the images, a direct analysis was conducted using the freeware software PhotoFiltre 6.5.1. The inspection process consisted of marking the perimeter of resin drop, after which, the area and longitudinal and transversal impregnation lengths were measured.
- b. Bottom microscope: due to the complexity of tracking the impregnated area using the images taken by the cameras, this process was performed externally after cross-linking the samples. The impregnated tows were extracted from the rig and a 20x macro-image of the bottom area was compiled using a collage of 300 micrographs as in shown in Figure 20. The macro-image was analysed using PhotoFiltre 6.5.1. The area where the resin had effectively passed through the thickness of the tow was highlighted and measured.
- c. The measurements obtained in the steps (a) and (b) were compared with the values obtained by the software in the previous step (iii) detailed above. The maximum error associated with the measurements obtained by the software in each experiment was determined.



Figure 20 20x macro-image of the impregnation developed on bottom face of the tow. This image represents a collage of 300 micrographs.

#### ***4.1.3.1 Top camera - error calculation***

It was found that the error in the readings of this camera regarding the longitudinal movement of the resin (in the fibre direction) and in the calculation of the area were negligible during approximately the first 60% of the test. This may be attributed to the resin drop having a sufficient volume for driving the permeation front by gravitational force. After some time, when capillary impregnation became the predominant phenomenon, it was noted that some error appeared in the longitudinal and transverse impregnated lengths. This error can be visualised in Figure 23 as a small variations in the data. However, in the transverse liquid-front (perpendicular to the fibres direction), due to small variations during the whole test, the capillary movement was detected since the beginning creating some instability in the measurement practically in the whole experiment. Nevertheless, due to the small variations in magnitude and hence the negligible contribution to the global error in the calculation of the area of the permeation front, it was assumed that the datasets were acceptable.

Figure 21 shows this phenomenon associated with the minor variations in the datasets. The upper area and longitudinal impregnation evolve with a smooth profile until the longitudinal capillary movement is the predominant mechanism (approximately after 120-130 seconds), when some undulations appear in the data.

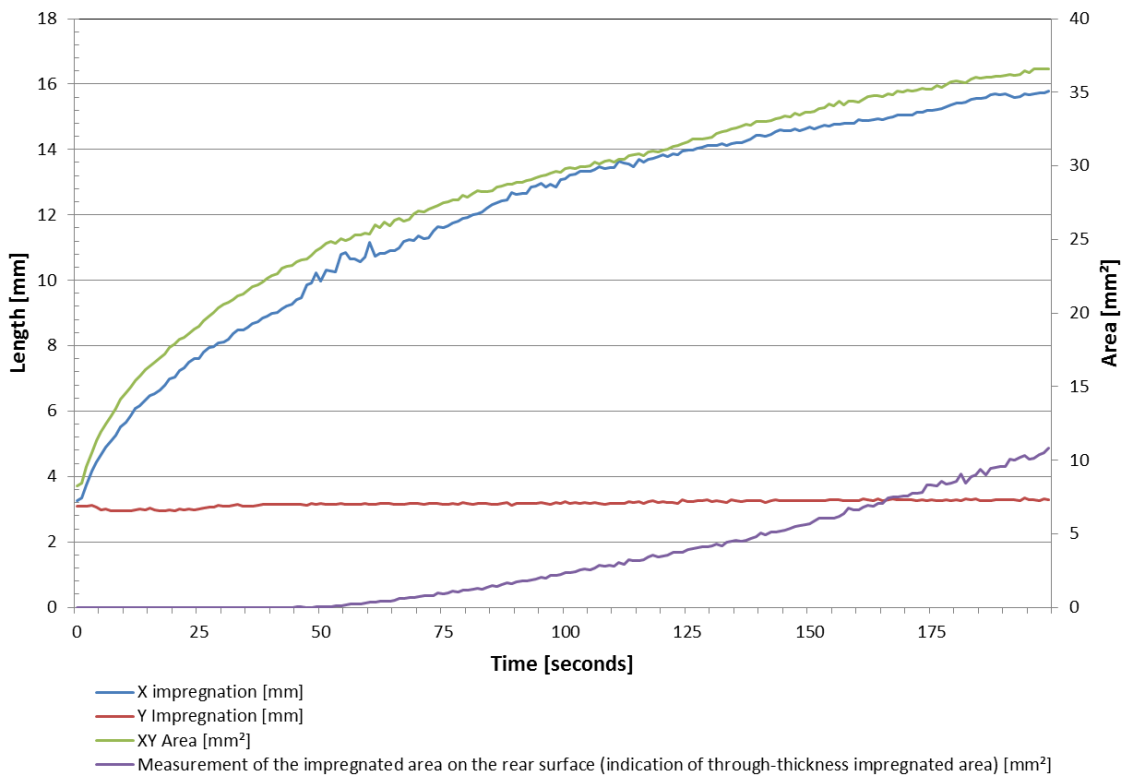


Figure 21 Results of an impregnation test carried out on a PPG tow obtained from the centre/bottom portion of the creel.

Following the methodology presented in section 4.1.3, six samples were analysed: four samples before applying the UV light after 100 seconds of the test when the effect of capillary movement was still small; and two samples after curing the resin by UV light where some degree of capillary movement was developed. After performing the previously defined signal processing methodology for the upper camera, a maximum error of 7% was found. A summary of the error analysis is presented in Table 4.

Table 4 Error analysis obtained in the six experiments performed, comparing the manual results with the ones obtained by the software.

Experiment	Details	Error		
		Area [%]	X impregnation [pixel]	Y impregnation [pixel]
1	Before UV curing	5%	4%	5%
2	Before UV curing	7%	3%	6%
3	Before UV curing	0%	2%	-1%
4	Before UV curing	-3%	3%	-4%
5	After UV curing	-3%	0%	4%
6	After UV curing	0%	-6%	7%

In addition, a comparison of the images analysed manually using PhotoFiltre and those done by the software showed a good degree of similarity, as shown in Figure 22.

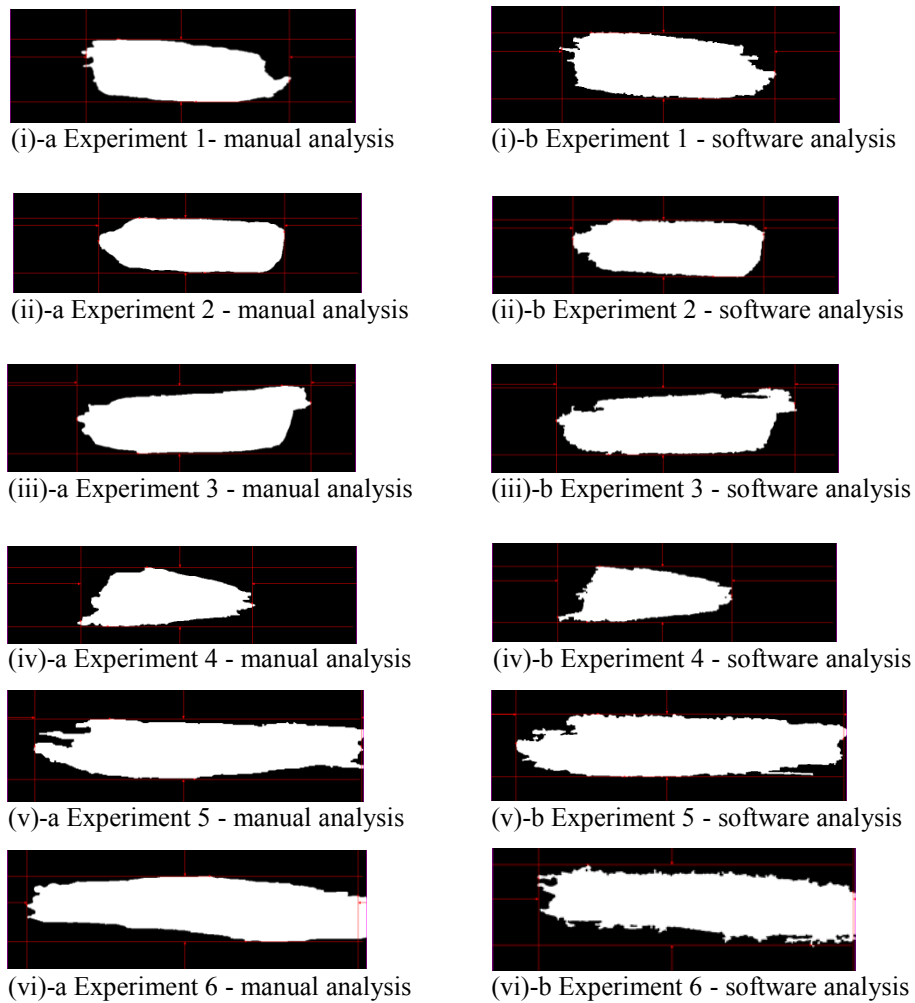


Figure 22 Details of the image analysis with the top camera

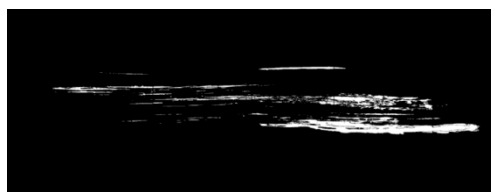
#### 4.1.3.2 Bottom camera - error calculation

The methodology described previously in Section 4.1.3 was followed to determine the error associated with the bottom camera. The results from this study are presented in Table 5, where a maximum error of 8% was found.

Table 5 Error associated with the bottom camera.

Experiment	Manual Measurements [mm]	Software Measurements [mm]	Error [%]
Test 4	7.20	7.29	1%
Test 5	10.36	10.78	4%
Test 7	16.21	16.47	2%
Test 8	12.93	13.95	8%
Test 9	24.02	25.53	6%
Test 10	32.19	33.5	4%

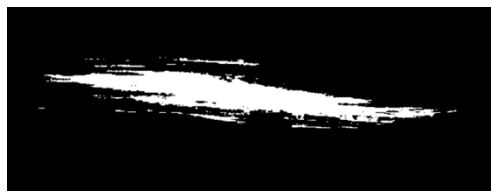
In addition, a comparison of the image analysis performed manually using PhotoFiltre and those performed by the software was carried out, as shown in Figure 23. On inspecting this Figure 23, it can be seen that the contours and geometry of the images obtained by the two methods are similar, despite the fact that the scale and the angle of the photographs on the right and on the left may be slightly different.



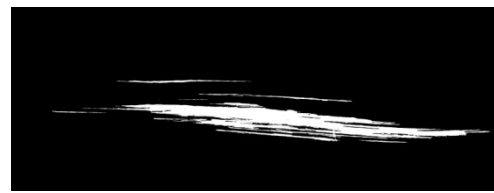
(i)-a Test 4 manual analysis



(i)-b Test 4 software analysis



(ii)-a Test 5 manual analysis



(ii)-b Test 5 software analysis

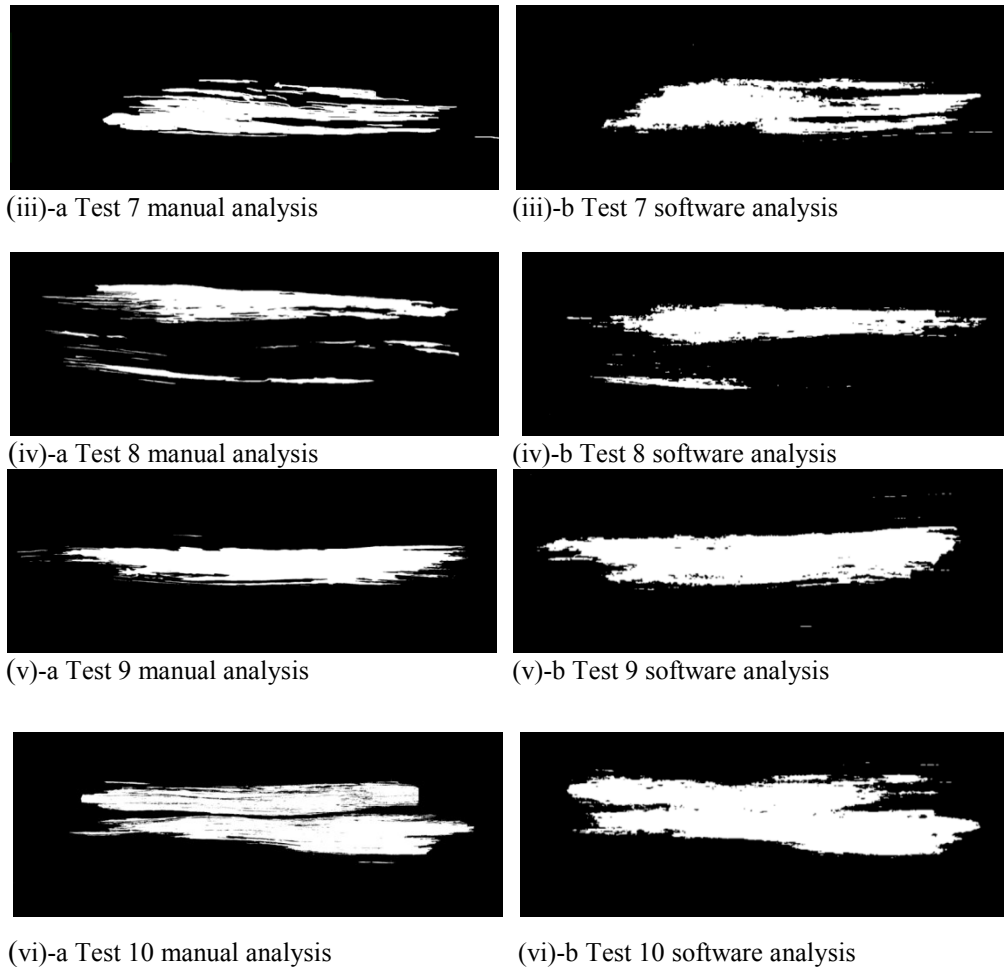


Figure 23 Comparison between the image analysis carried out using the manual inspection over the 20x image (images on the left) and the automatic analysis done by the software using the bottom microscope (images in the right).

#### 4.1.4 Impregnation results

The impregnation monitoring experiments were carried out using a creel of as-received PPG Hybon 2026 Tex 2400 fibres. The coding of the reel with regards to specified locations described in Section 3.1.1.2 was adopted. For comparison purposes, a limited number of spread fibres from PPG and as-received Owens Corning Avantex T30 R25H2400 were tested. Since the PPG spread fibres were subjected to a mechanical spreading process it was assumed that it would not be necessary to identify the position of the tow from within the creel. For the Owens Corning samples, due to the different creel dimensions and hence the difficulties in

comparing layer-by-layer with the PPG creel, only the information of the zone from they were extracted (top, middle, bottom) was tracked. A summary of the samples is presented in the Table 6.

Table 6 Summary of the number of tests, materials, condition of the fibres and their relative positions within the creel for the impregnation monitoring studies.

Experiment	Number of tests	Manufacturer	Characteristics	Layer	Zone
1	8	PPG	As-received	External	Top
2	8	PPG	As-received	External	Middle
3	8	PPG	As-received	External	Bottom
4	8	PPG	As-received	Centre	Top
5	8	PPG	As-received	Centre	Middle
6	8	PPG	As-received	Centre	Bottom
7	8	PPG	As-received	Internal	Top
8	8	PPG	As-received	Internal	Middle
9	8	PPG	As-received	Internal	Bottom
10	8	PPG	Spread	Not applicable	Not applicable
11	8	Owens-Corning	As-received	Not applicable	Top
12	8	Owens-Corning	As-received	Not applicable	Middle
13	8	Owens-Corning	As-received	Not applicable	Bottom

Each individual test was carried out for 200 seconds during which the images were acquired and analysed at 1 Hz (1 complete analysis per second) giving 200 rows of data. In each row, the X (longitudinal), Y (transverse) impregnation, and the XY (top area) and Z (through-thickness impregnation) impregnated area were recorded. An illustration of the relevant parameters is presented in Figure 24.

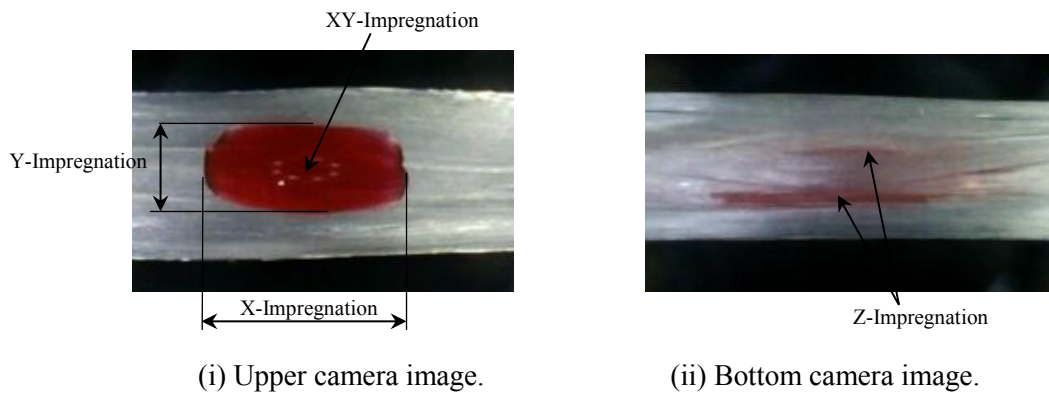
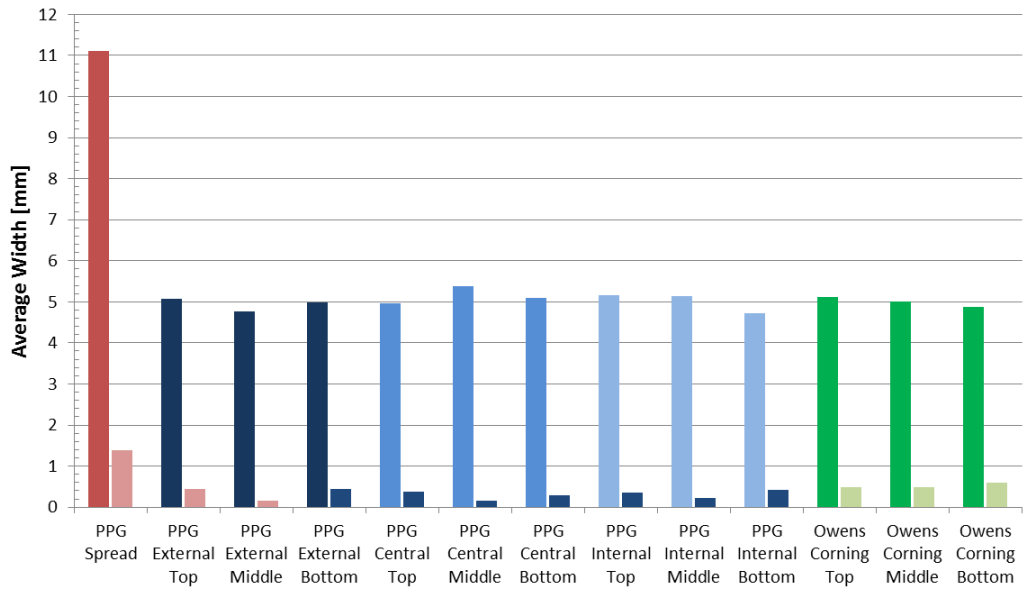


Figure 24 Typical example of an impregnation experiment with the definition of each parameter measured during the tests: (i) X and Y-impregnation length, and XY-impregnated area monitored by the upper camera; (ii) Z or through-thickness impregnation monitored by the bottom camera.

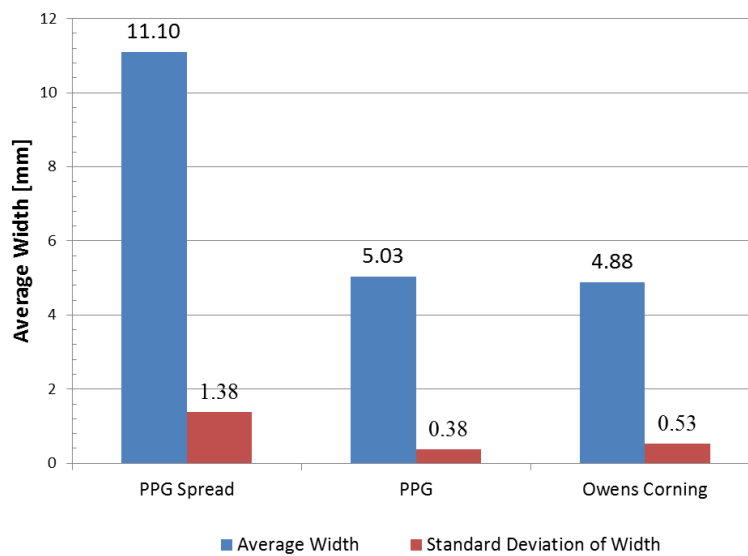
Due to the fact that the X and Y-impregnations are one-dimensional (maximum lengths in the X and Y-directions), consideration is given to the XY and the Z-impregnation profiles. The justification for this decision is: (i) their higher stability; (ii) the lower added error; and (iii) the impregnated area being a more representative representation of the impregnation process.

#### 4.1.4.1 Variation in the width of the samples used in the tests

Due to the relationship between thickness and impregnation time (see Equation 4), a statistical analysis (mean and standard deviation) of the thickness for all the samples involved in each impregnation experiment was performed. The results are presented in Figure 25, following the coding system for the creel that was presented previously in Figure 4.



(i)



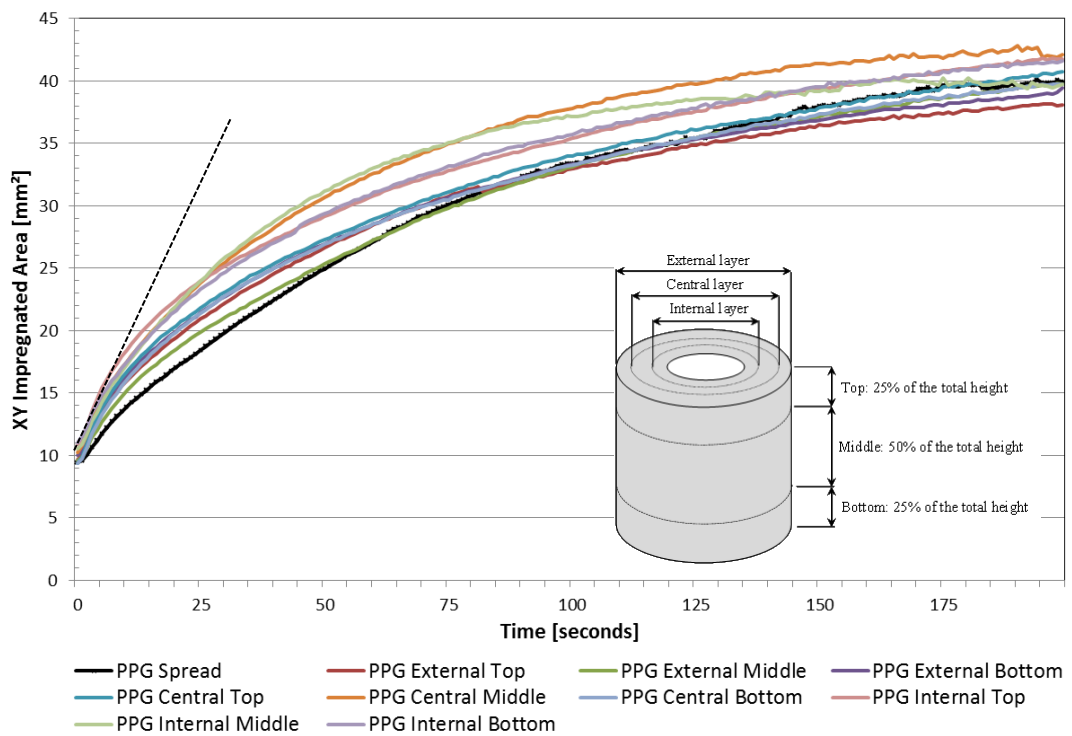
(ii)

Figure 25 Statistical analysis of the width of the samples used in the impregnation tests: (i) the average and standard deviation of each experiment detailed in Table 6 attending to the segment of the creel in the as-received material (the data are presented in sets of two columns showing the average on the left and the standard deviation on the right); (ii) average fibre bundle widths for the spread and as-received PPG fibre bundles and the as-received Owens-Corning fibre bundles.

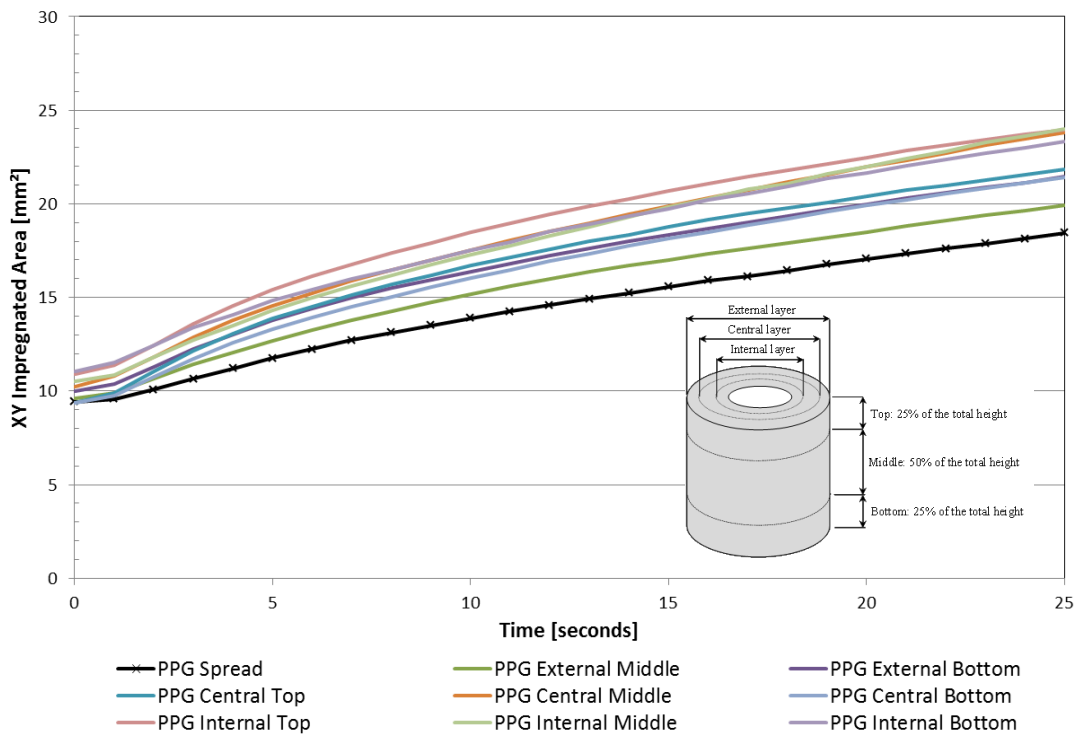
#### 4.1.4.2 XY-impregnation

The average (eight samples per batch) XY-impregnation data for the as-received/spread PPG and for the as-received Owens-Corning fibres are shown in Figure 26 and Figure 27

respectively; the 8 samples tested for each experiment were averaged for simplifying the visualisation of the data. It is apparent that the permeation of the drops of resin over the surface of the PPG fibres (as-received and spread) follows polynomial trajectories. Moreover, the spread PPG fibres have a different starting slope than that observed for the as-received fibres which have a more steady increase. This behaviour can be explained by the more uniform, flat and horizontal shape of the spread fibres in comparison with a highly irregular geometry of the as-received fibres.



(i)



(ii)

Figure 26 Evolution of the XY-impregnation for the as-received and spread PPG fibres. The different colours for the as-received fibres correspond to their relative positions from within the creel: (i) shows the full length of the test (200 seconds); (ii) presents an expanded view of the first 25 seconds. The dotted line in Figure 26 (i) represents the average initial slope.

With reference to the as-received Owens-Corning fibres, the experiments showed a linear increase in the impregnation area for the first ten seconds and after a short transition, they changed to a linear trend but with a smaller slope. This is notably different to the behaviour that is observed with the as-received PPG fibres.

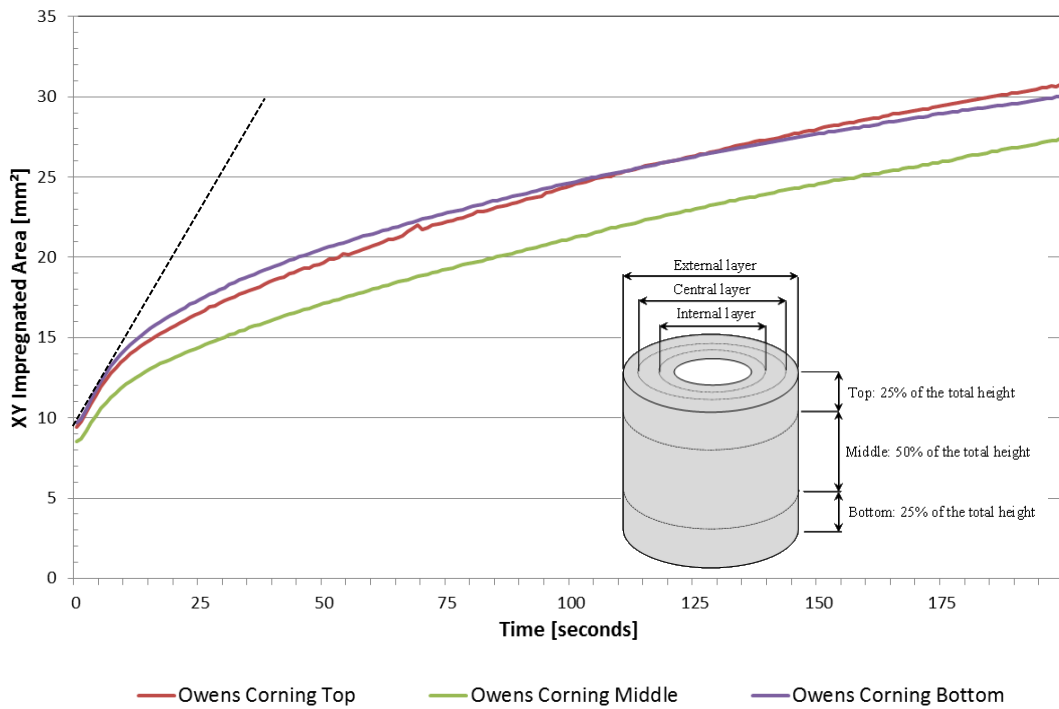


Figure 27 Evolution of the XY-impregnation for the as-received and spread Owens-Corning fibres. The different colours for the as-received fibres correspond to their relative positions from within the creel. The dotted line represents the initial slope.

With reference to Figure 26 (i) and Figure 27, the XY-liquid-front for the as-received PPG fibres and Owens-Corning fibres show substantial differences with regard to the areas that are covered after 200 seconds. In the as-received PPG fibres, the impregnated area is contained in the interval from 37 to 42 mm<sup>2</sup>. In the case of the as-received Owens-Corning, the impregnated area ranged from 27 to 31 mm<sup>2</sup>. Besides, the initial slope (dotted lines) was found much higher in the as-received PPG fibres than in the Owens-Corning fibres, with values of 0.88 and 0.59 respectively.

#### ***4.1.4.3 Through-thickness impregnation***

Figure 28 shows the through-thickness impregnation for as-received and spread PPG fibres, and Figure 29 presents the same for the Owens-Corning as-received fibres. As with the previous case, the eight samples used in the experiments were averaged.

The magnitude of through-thickness impregnation was defined as the area of resin which effectively permeated through the thickness of the sample, as measured by the bottom camera.

It can be appreciated that the spread fibres displayed by far the fastest through-thickness impregnation rate. For example, after around 15 seconds, the resin had effectively permeated through the tow and then commenced to evolve with linear speed at a decreasing rate. However, in the case of the as-received PPG fibres, all the graphs had a common starting point at approximately 25 seconds when some degree of impregnation was obtained, followed by a period of acceleration before the rate decreased. After the aforementioned starting point of 25 seconds, the subsequent trends at different locations of the creel were found to be different. It is proposed that this may be due to the intrinsic variability in the architecture of the bundle.

It is interesting to note that the as-received PPG fibres obtained from the central layer and centre zone of the creel (see Figure 28) have a faster impregnation characteristic. This can be explained by inspecting Figure 25 where it is seen that this bundle had the biggest width (and hence the lowest thickness) of the as-received fibre bundles, which may have had a significant effect on the through-thickness impregnation rate. Visual observation of the as-received fibre bundles has also indicated that the following additional reasons may be contributing factors:

- (i) the degree of segmentation in the as-received fibre bundle;

(ii) the concentration/distribution of the binder;

(iii) the degree of waviness (a function of the tension during the production of the creel); and

(iv) the compaction of the fibre bundle and hence the micro-porosity within the filaments.

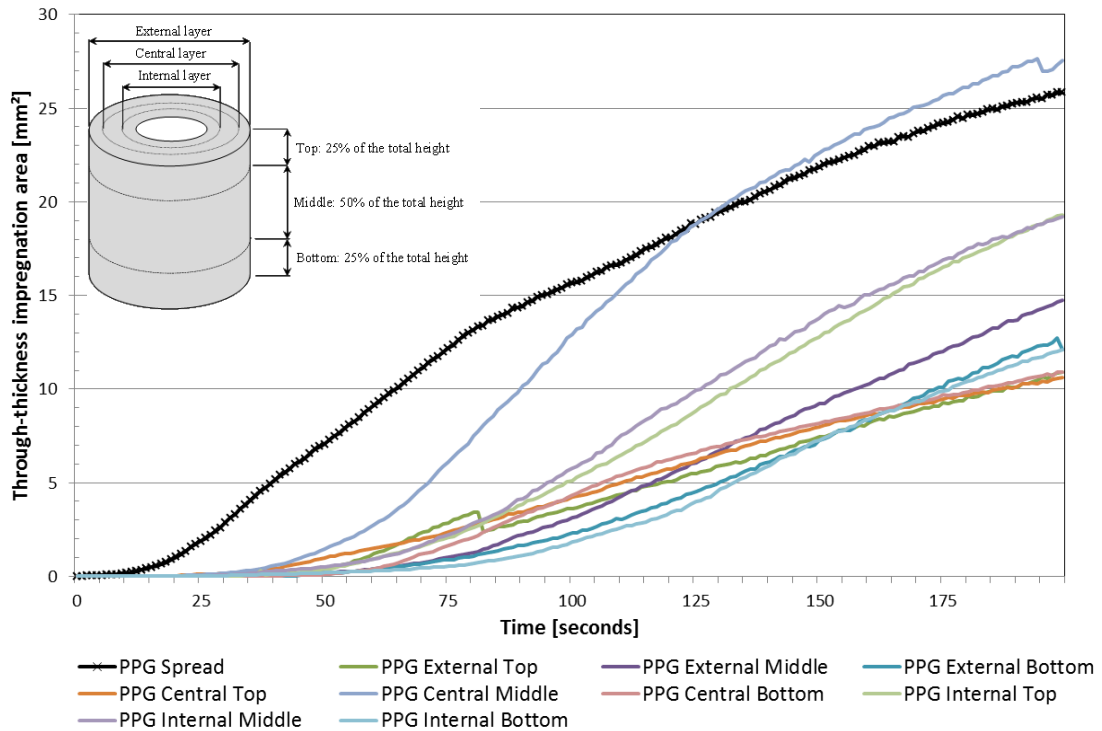


Figure 28 Through-thickness impregnation for PPG spread and as-received fibres.

Surprisingly, on inspecting Figure 29 it is seen that the through-thickness permeation of the resin through the as-received Owens-Corning fibres was negligible. Moreover, as a consequence, the signal-to-noise for this fibre type is low which results in a noise signal. It is speculated that if the test was to be extended past 200 seconds, the as-received Owens-Corning fibres will attain a similar equilibrium through-thickness impregnation characteristic as that observed for the as-received PPG fibres.

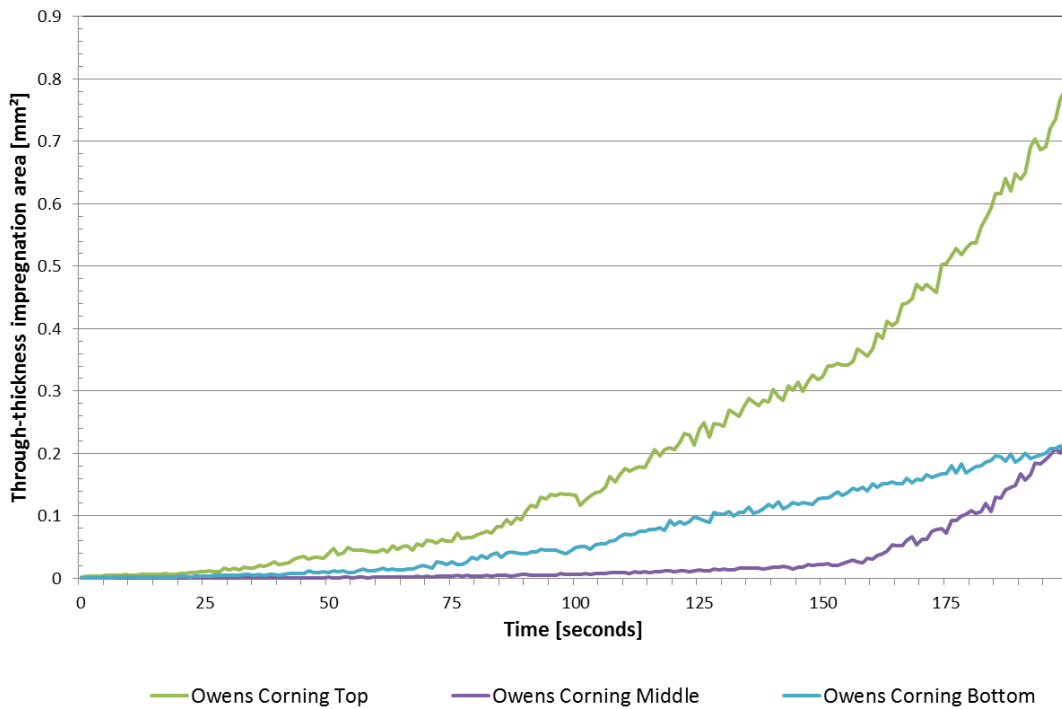


Figure 29 Through-thickness impregnation evolution for the Owens Corning as-received fibres.

In conclusion, it is notable that the average through-thickness area for the as-received Owens-Corning fibre was after 200 seconds much smaller than the as-received PPG fibres. It was observed for the as-received PPG fibres that the through-thickness area was not less than  $11 \text{ mm}^2$  after 50 seconds with most of the samples lying in the range  $11$  to  $20 \text{ mm}^2$ . However, the as-received Owens-Corning fibre did not surpass the value of  $0.8 \text{ mm}^2$ , with a corresponding impregnated area of around  $0.2 \text{ mm}^2$  in the majority of the samples.

#### 4.1.4.4 Comparison of the global averages

This section presents a brief discussion on the global averaged data for the three different groups of fibres: as-received PPG, spread PPG and as-received Owens-Corning. In this analysis, only one average curve for the XY-permeation and one for the through-thickness

impregnation was considered for each one of the above mentioned group of fibres. The results are shown in Figure 30 and Figure 31.

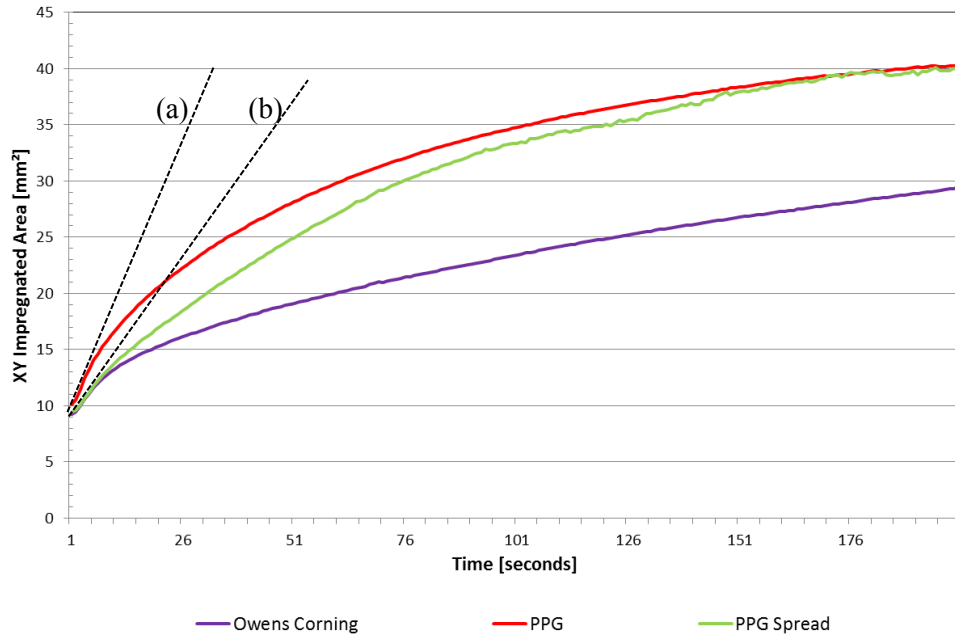


Figure 30 Averaged XY-permeation versus time for each different group of fibres: Owens-Corning fibres (blue), as-received PPG fibres (red) and spread PPG fibres (green). The dotted lines (a) and (b) represents the initial slopes.

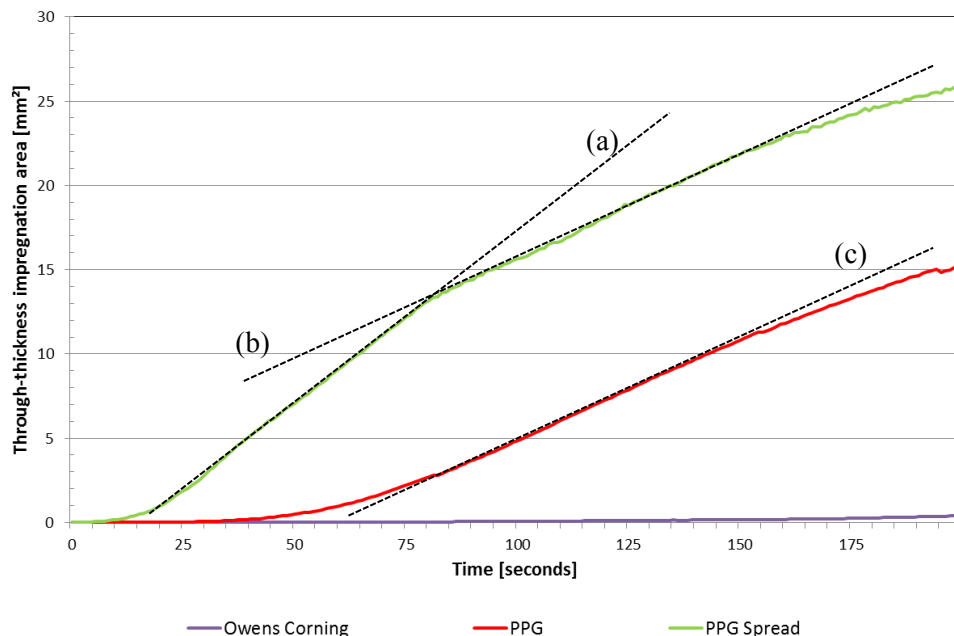


Figure 31 Averaged through-thickness impregnation evolution versus time for: Owens-Corning fibres (blue); as-received PPG fibres (red); and spread PPG fibres (green). The black dotted lines represent the slopes of the evolution of the through-thickness impregnation area; (a) and (b) show the two different slopes presented by the spread PPG fibres; and (c) shows the slope of the as-received PPG fibres.

Similar conclusions to those mentioned previously apply here:

- (i) The XY-impregnation for the as-received and spread PPG fibres shows a parabolic evolution with similar final asymptotic values. The Owens-Corning fibres start with a parabolic shape, but after approximately 10 seconds changes to linear trend.
- (ii) The XY-impregnation of the as-received PPG fibres have a higher initial slope of 0.20, represented in Figure 30 as a dotted line labelled as (a). The XY-impregnation for the Owens-Corning fibres and for the spread PPG, however, shows a similar initial slope of 0.63, labelled as (b) in Figure 30.
- (iii) The XY-impregnation achieved by the PPG fibres (both spread and as-received) is approximately 30% higher than the observed for the Owens-Corning fibres.
- (iv) Through-thickness impregnation was not observed in the as-received PPG fibres up to 30 seconds. After that point, the impregnation developed following a linear evolution with a slope of 0.12 until nearly the end of the test. This is shown in Figure 31 by the dotted line labelled as (c).
- (v) The through-thickness impregnation in the spread PPG fibres started after 5 seconds, having linear evolution with two different slopes, as is presented in Figure 31 by the dotted lines labelled as (a) and (b): a faster first part up to the 82-second with a slope of 0.20, followed by a second part when the impregnation is slower with a slope of 0.12. It is notable, as it can be observed in Figure 31, that this second slope of the spread PPG fibres is the same than the as-received PPG fibres, after approximately 82 seconds.
- (vi) The through-thickness impregnation of the as-received Owens Corning fibres showed negligible impregnation during the first 200 seconds of the test (below  $1 \text{ mm}^2$ ).
- (vii) During the first 50 second of test, the spread PPG fibres develop a 700% higher impregnation area than the as-received PPG fibres.

#### 4.1.4.5 Permeability calculations

The impregnation time can be calculated using the data presented in Figure 31. Here, impregnation time is defined as the period for obtaining a consistent reading for a through-thickness impregnated area of 0.1 mm<sup>2</sup>. Utilising the data obtained with the application of this criteria and rewriting Equation 4 (relation between impregnation time in Z-direction and permeability), Equation 10 was derived. In this equation the permeability K for the PPG fibres in Z-direction or through-thickness can be obtained as function of the dynamic viscosity  $\mu$ , the thickness L, the impregnation time (defined criteria of 0.1 mm<sup>2</sup> for the impregnated area) and the pressure gradient.

$$K = \frac{\mu}{2t} \cdot \frac{L^2}{\Delta P} \quad \text{Equation 10 [16]}$$

The dynamic viscosity is given in Figure 19 and the pressure gradient can be calculated using Equation 8. Since there was no vacuum or mechanical pressure involved in the test, the assumption is made that the contribution to the pressure is due to the gravitational force (weight of the resin) and capillary pressure. A further assumption is made that the evolution of the gravitational contribution can be taken in each moment as the mass of the resin drop divided by its XY-permeation area. The capillary pressure is calculated using Equation 8 with a form factor (F) of 2, a contact angle of 57° and surface tension 0.044 N/m, as reported in Section 2.4.1.2. With reference to the porosity, computer aided analysis was performed on the images of the same samples detailed in Section 4.1.3.2 where the porosity was estimated to be in the range of 44% to 48%.

With reference to Equation 8, L can be calculated assuming a rectangular cross-sectional area along with the manufacturer data for the number of fibres per tow (4000), the average

diameter (17  $\mu\text{m}$ ), and the porosity (44% and 48%) and the average width of the tow from Figure 25.

The results for the permeability obtained for both porosity levels are given in Figure 32. They are organised in pairs representing both porosities of 44% and 48% with the data presented in the following order: spread PPG fibres, PPG global average value (for all the 9 experiments), Gebart's theoretical values (Figure 3) for the specified porosity levels and the average value for each layer of PPG as-received fibres (exterior, centre and inner as seen in Figure 4):

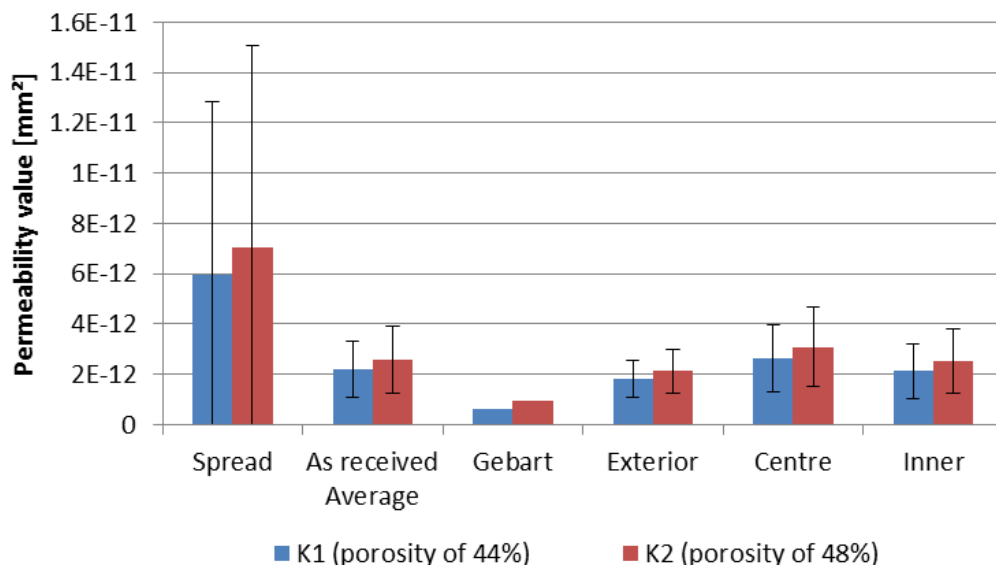


Figure 32 Transversal permeability values for the PPG spread and as-received fibres calculated by Equation 4, with a comparison with the values obtained by Gebart's model; all the transversal permeability coefficients are calculated for the two considered values of porosity and shown two different colours (44% of porosity in the blue columns and 48% porosity in the red columns), with the standard deviation represented by an error bar.

As can be appreciated the PPG spread fibres have increased the transverse permeability by nearly 250% in comparison with the as-received fibres; this means that spreading the fibres by an average value slightly higher than 200%, decreases the average transverse impregnation time by a factor of 2.5. Besides, there is a very high standard deviation in the calculated values and this may be due to one or more of the following reasons: (i) the spread fibres were

collected from different experiments and with different levels of spreading (from 8.62 mm to 12.30 mm); and (ii) some of the spread fibres had gaps or segmentation between the fibres (test 1 and test 7) and thus the impregnation process for these fibres with the previously assigned criteria of  $0.1 \text{ mm}^2$  was nearly instantaneous (a few seconds).

It is worth noting that the values obtained for the as-received fibres gave transverse permeability coefficients that were higher than the ones reported by the Gebart's equation. This observation may be attributed to the different conditions in which the tests were performed. For example, in the current work, consideration was only given to the capillary and the gravitational pressure where the fluid was a small and constant non-pressurised volume of resin. Moreover, Figure 33 shows that the appearance of macro-channels can increase the porosity and thus modify the capillary pressure and the impregnation time. It was also observed in the current study that the binder content was variable in sections of the tow. Finally, the permeability data reported here assumed the two calculated values of porosity. Visual observations suggested that the spatial architecture of the filaments was highly variable and different values of porosity would be obtained along different sections of the same impregnated volume. Therefore, this may account for the observed deviation from the Gebart's experimental data.

#### **4.1.5 “Freezing” the resin flow**

The methodology developed in this current study was based on tracking the motion of the fluid-front using cameras on the top and the bottom of the tow. Hence, the following experiment was performed to visualise the flow of the resin in the through-thickness direction. This study was also designed to validate through-thickness permeation data obtained via the cameras.

- a. The samples used for the bottom camera tests, number 4, 5, 7, 9 and 10 were cut at the centre of the cured resin profile and mounted in the transparent Epofix Cold Mounting Resin (Struers, UK).
- b. The surface was polished using conventional metallographic procedures.
- c. Micrographs were obtained using a CMOS camera model DCU224C (Thorlabs, UK).

With reference to Figure 33, it is proposed that the resin penetrated effectively through the thickness of the tow in two modes: macro-flow across macro-channels surrounding the clusters of fibres; and micro-flow within the clusters of filaments. This observation was found in the five samples that were analysed.

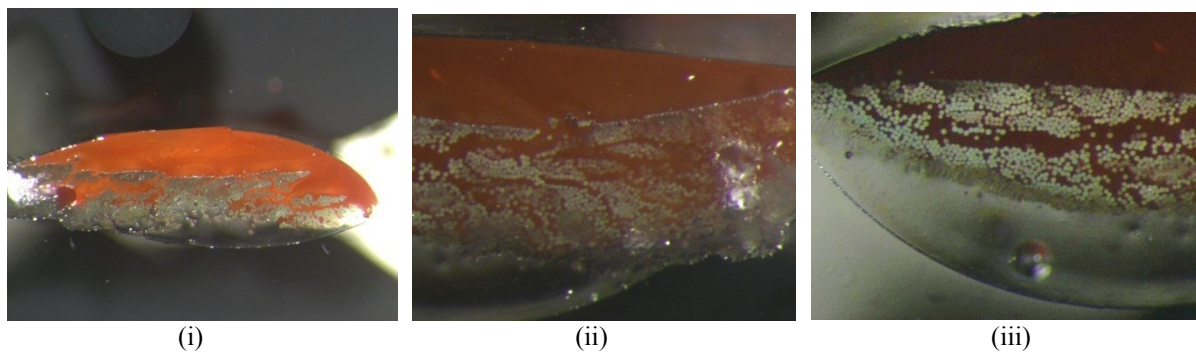


Figure 33 Illustration of the permeation profile of the pigmented cross-linked photo-curable resin on sample number-4: (i) 10x image of the sample; (ii) 20x image showing the left area of the sample; and (iii) 20x image of the central area of the sample. Due to the nature of the microscope used in conjunction with the camera, it was not possible to obtain a scale bar.

In conclusion, this last experiment provides sufficient justification to support the view that the evolution of the resin on the top and bottom face of the tow gives an accurate idea about how the resin permeates through the material. Thus, the estimations done by the software can be considered as a valid indication of the impregnation at both macro and micro-levels.

## 4.2 On line-monitoring of the thickness of the tow

### 4.2.1 Airtightness of the pneumatic system

Since the pneumatic equipment used in this study operated on the basis of a constant volume of air inside the cylinder, some tests were conducted with different applied pressure to establish the airtightness of the system. This consisted of the application of an initial pressure to the pneumatic cylinder and monitoring the changes in the forces measured by the load-cell as a function of time. This was used to estimate the magnitude of the pressure loss. As seen in Figure 34, for an applied load of 6.73 kgf recorded by the load-cell (higher than the maximum force expected during the tests), the reading after 1,200 seconds recorded a loss of 0.08 kgf. This represents a pressure loss of the order of 0.5%. It was noted that in the majority of the cases, the losses occurred during the first 200 seconds and hence was not considered to be significant.

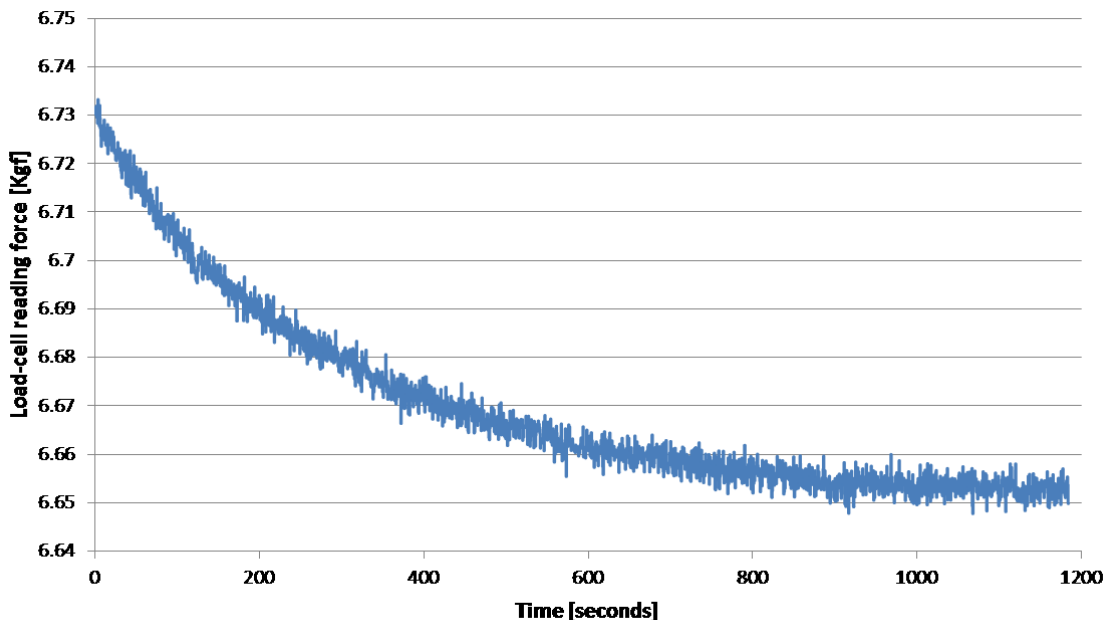


Figure 34 Display of the force monitored by the load-cell over 1200 seconds to establish the pressure-retention capacity of the pneumatic device.

#### **4.2.2 Load-cells calibration**

The load-cells were calibrated prior to their use in the rig. The method used was to compare the output of the load-cells by loading them with samples of known masses.

The first series of calibrations were used to enable a software-based correction to be made, based on the comparison between the measured and the mass of each applied load. This is justified on the basis that a correction is generally required in order to compensate and to minimise the error which is inherent in the load-cell. After this correction, the experiment was repeated and the measurement error of the system was established. In the case of the 3 kg load-cell, the maximum error was found to be in the range of 0.018%. In the case of the 50 kg load-cell the maximum error was found to be lower than 0.80%. This means that both load-cells will have an error in the range of use of  $\pm 0.00054$  kgf and  $\pm 0.040$  kgf for the 3 kg and 50 kg load-cells respectively.

#### **4.2.3 Correlation between the measured force and the thickness of the tow**

Tests were performed to establish the relationship between the initial applied pressure in the pneumatic cylinder and the output force read by the load-cell. This was done to enable correlation between the changes in force recorded by the load-cell with changes in the thickness of the tow as it traversed between the rollers (see Figure 13). These tests were carried out using four initial loads, 0.5, 0.6, 0.8 and 1.35 kgf, following the experimental method detailed below:

- (i) Pressurised air was introduced in the system closing the mobile internal bridge and thus, translating the upper roller down until it touched the bottom roller; this process was

stopped when the desired initial load was achieved in the load-cell that was attached to the cylinder (see Figure 15).

- (ii) Flat rectangular feeler-gauges (10 mm x 70 mm) with thickness of 0.04, 0.07, 0.1, 0.15 and 0.2 mm were introduced and removed periodically from between the rollers. Their introduction created an additional pressure in the cylinder and hence increased the force recorded by the load-cell. Each load/unload cycle was repeated four times for each of the thicknesses stated above.
- (iii) For each load/unload cycle (the term load means the insertion of the feeler-gauge in between the rollers, and the unload represents its removal), the difference between the load and unloaded forces were calculated. The averages and the standard deviation of these differences are presented in Table 7.

Table 7 Summary of the averages and the standard deviations for the increases in the force measured by the load-cell as a function of the thickness of the feeler gauges.

Thickness [mm]	Initial force								Median Average [kgf]
	0.5 kgf		0.6 kgf		0.8 kgf		1.35 kgf		
	Median	Stdev	Median	Stdev	Median	Stdev	Median	Stdev	
0	0	0.07	0	0.067033	0	0.064226	0	0.065727	0.00
0.04	1.65	0.10	1.4175	0.155	1.5025	0.146828	1.361	0.259663	1.48
0.07	2.72	0.22	2.817	0.174748	3.0175	0.362985	3.091	0.119024	2.91
0.1	4.13	0.12	4.2275	0.075	4.3325	0.131909	4.401	0.102794	4.27
0.15	5.29	0.05	5.0325	0.037749	5.3225	0.023805	5.016	0.022174	5.16
0.2	5.52	0.08	5.4475	0.031091	5.7475	0.040311	5.276	0.080829	5.50

With reference to Table 7, it was found that the output forces recorded by the load-cell were only dependent on the thickness of the feeler gauges, and independent of the initial pressures. Hence, it can be assumed that the output of the load-cell is independent of the initial pressure. In addition, the 4<sup>th</sup> order polynomial trend line for this dataset as indicated by Equation 11, was found to describe this behaviour with a  $R^2$  greater than 0.99.

$$y = 0.0012x^4 - 0.0108x^3 + 0.0278x^2 + 0.005x + 0.0001 \quad \text{Equation 11}$$

Therefore, this relationship can be used to correlate the forces recorded by the load-cell (kilograms) and the thickness (millimetres) of the material traversing between the rollers. This conversion is based on having an initial applied pressure below 1.35 kgf when the rollers are in contact with the sample at the start of the test. In addition, because of the thickness of this cross-section of the tow is unknown when the process starts (the rollers are closed and an initial pressure is applied), only the relative thickness of the tow can be obtained. Since the aim was to understand the variability in the thickness of the tows for different unwinding methods and different positions/layers in the creels, it was not necessary to add any additional step or hardware for measuring the initial thickness. Thus, the method developed here was capable of imparting data on the variation of the thickness of an as-received tow.

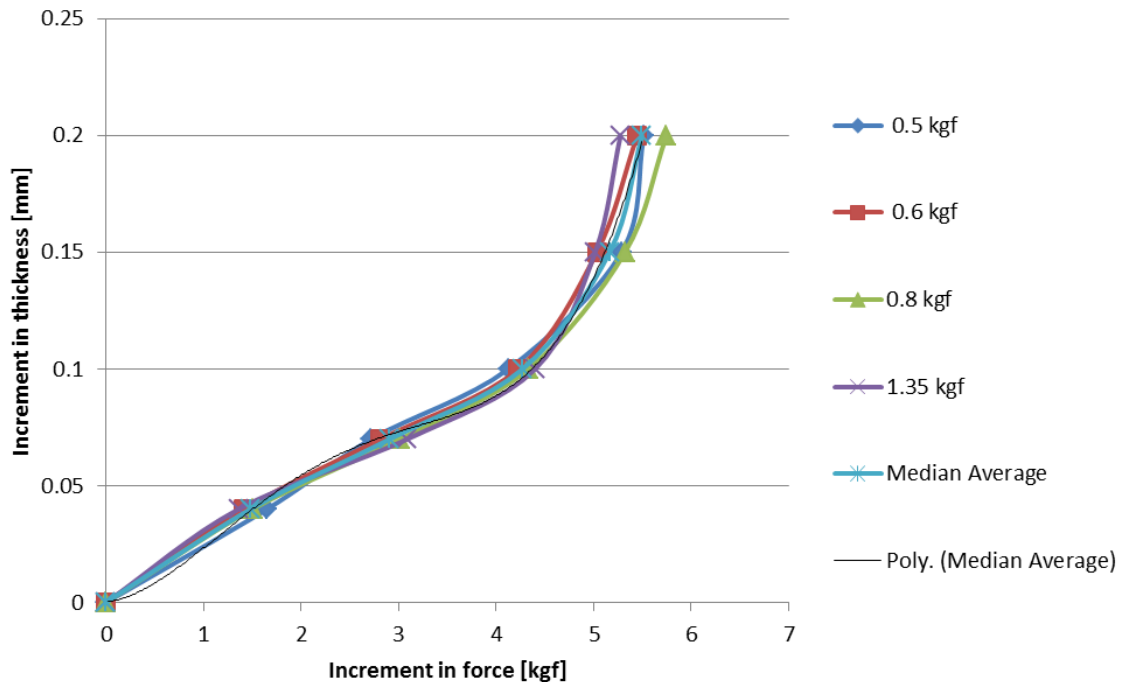


Figure 35 Representation of the increases of the force measured in the load-cell for the different initial forces and for the different thicknesses of the feeler gauges.

#### 4.2.4 Thickness and width measurement using Hybon 2026 Tex 2400

This experiment was performed with two creels from the same batch of PPG Hybon 2026 Tex 2400. However, two methods were used to draw the tow from the creel: centre-pull and external-draw; a schematic illustration of the two processes is presented in Figure 36.

The first creel was evaluated by extracting the tow from the inner bore (centre-pull). The advantage of this method to unwind the tow from the creel is that it can be performed without the help of any mechanical devices. However, centre-pull does introduce a twist to the line for each  $360^\circ$  extraction from the bore. The practical problem with twisting is that it results in lower spreading and a higher degree of irregularity in the thickness of the tow.

The second creel was secured on a rig and the tow was unwound manually by turning the handle of the creel stand. This external-draw or drawing method to unwind the creel does not introduce any additional twist into the tow but it does require the manual unwind of the creel. In practice, this method of payout requires motors and tension-controllers to unwind the creel.

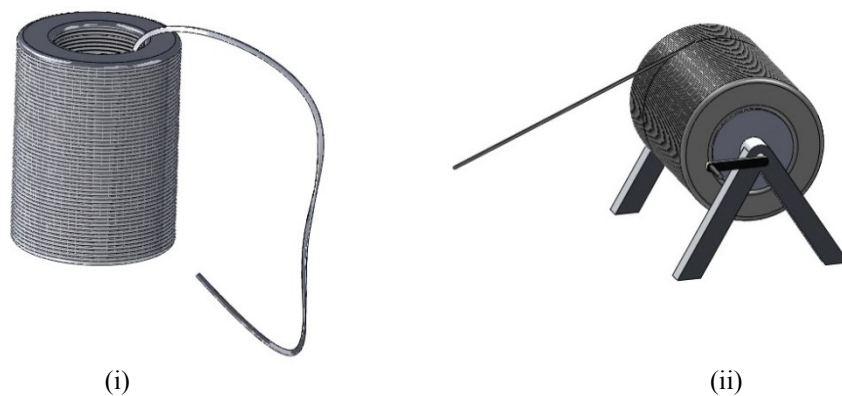


Figure 36 Detail of the unwind method using with the PPG Hybon 2026 Tex 2400 creels: (i) centre-pull; and (ii) external-draw.

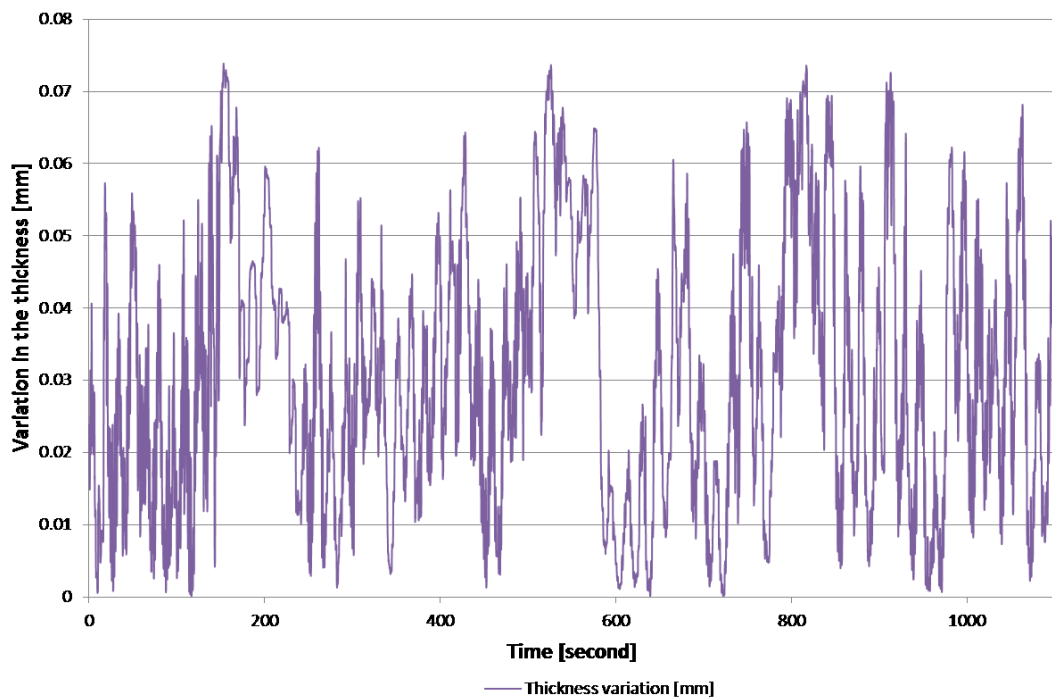
With the two techniques for unwinding the creels, the haul-off rate was fixed at 1,050 mm/minute. The data acquisition rates were 100 Hz for the load-cell and 5 Hz for each one of

the cameras. The 100 Hz sampling rate for the load-cell allowed the force generated by the tow (a function of its thickness) to be measured at 0.175 mm intervals. The sampling rate of 5 Hz for the cameras allowed the acquisition of the widths entering and exiting the pair of rollers at 3.5 mm intervals. The length of fibres tested for the two modes of unwinding is defined in Table 8. A schematic illustration defining the relative positions within the creel is shown in Figure 4.

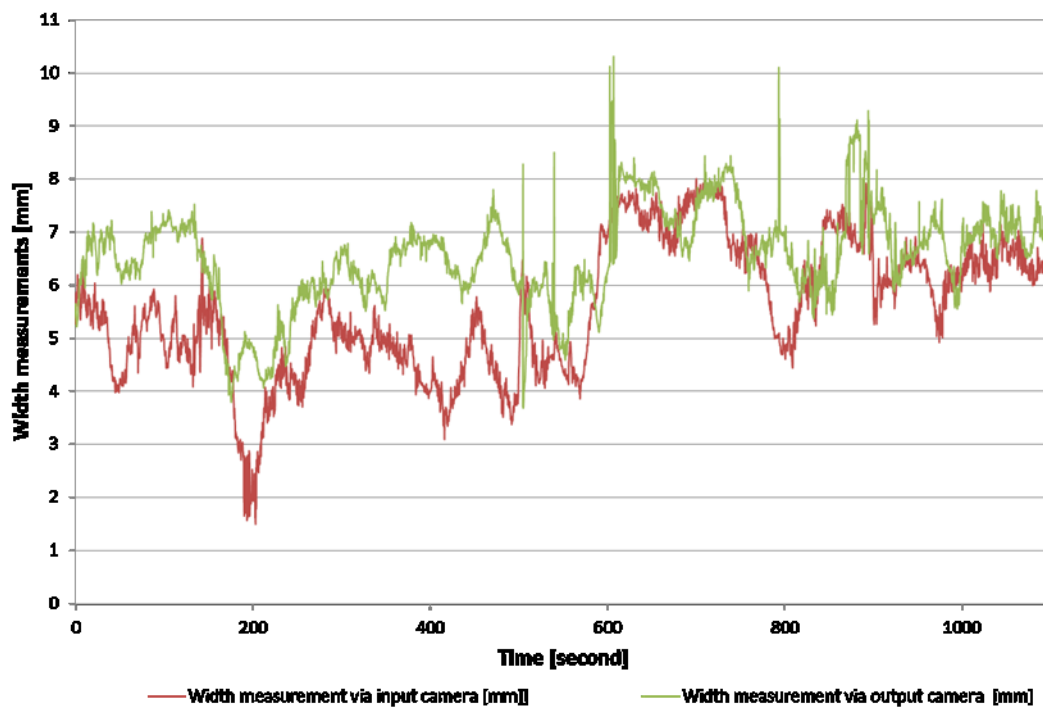
Table 8 Summary of the tow length tested as a function of the position of the tow into the creel for centre-pull and outside-draw methods for unwinding. These experiments were carried out on Hybon 2026 Tex 2400 (PPG).

Position	Centre-pull			External-draw		
	External layer	Central layer	Internal layer	External layer	Central layer	Internal layer
Top	5.16 m	5.56 m	5.00 m	6.14 m	5.75 m	5.35 m
Middle	10.12 m	9.42 m	10.19 m	10.66 m	12.35 m	10.37 m
Bottom	5.10 m	4.70 m	4.59 m	5.15 m	5.65 m	5.76 m
Total analysed length	20.38 m	19.67 m	19.78 m	21.95 m	23.75 m	21.48 m

A typical example of the width and thickness measurements via the cameras and the pressure load-cell as the tow traverses in between the pair of rollers is shown in Figure 37. The data of the load-cell were processed using Equation 11 for converting the force readings into the apparently thickness of the tow.



(i)

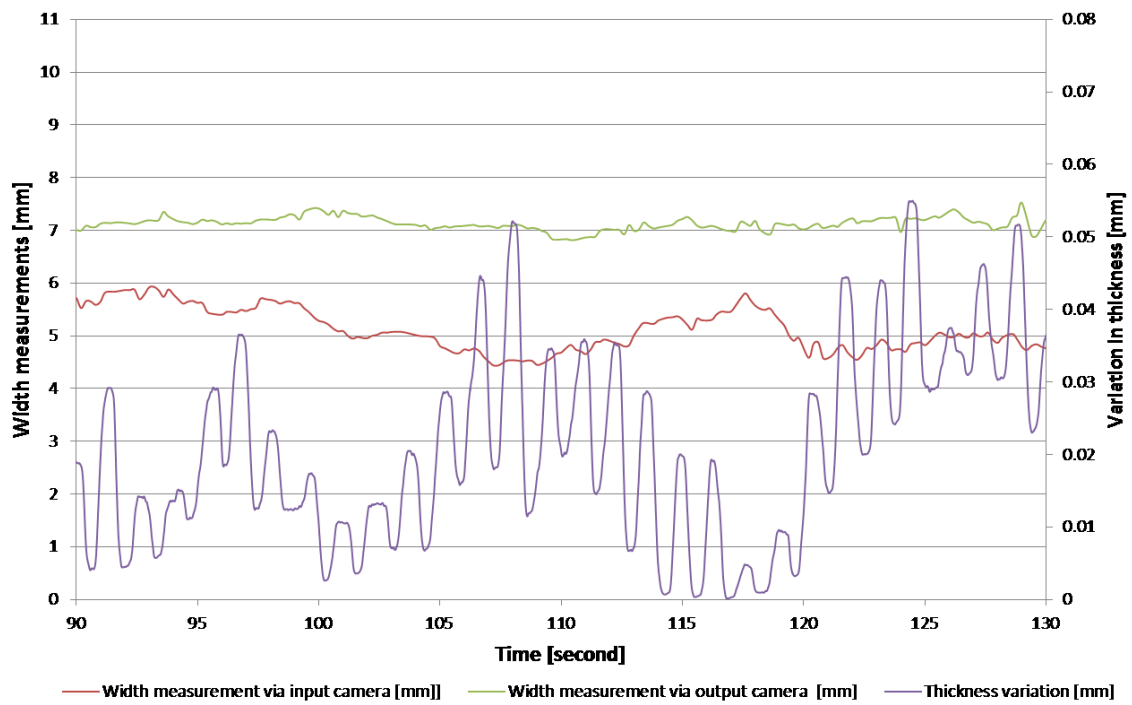


(ii)

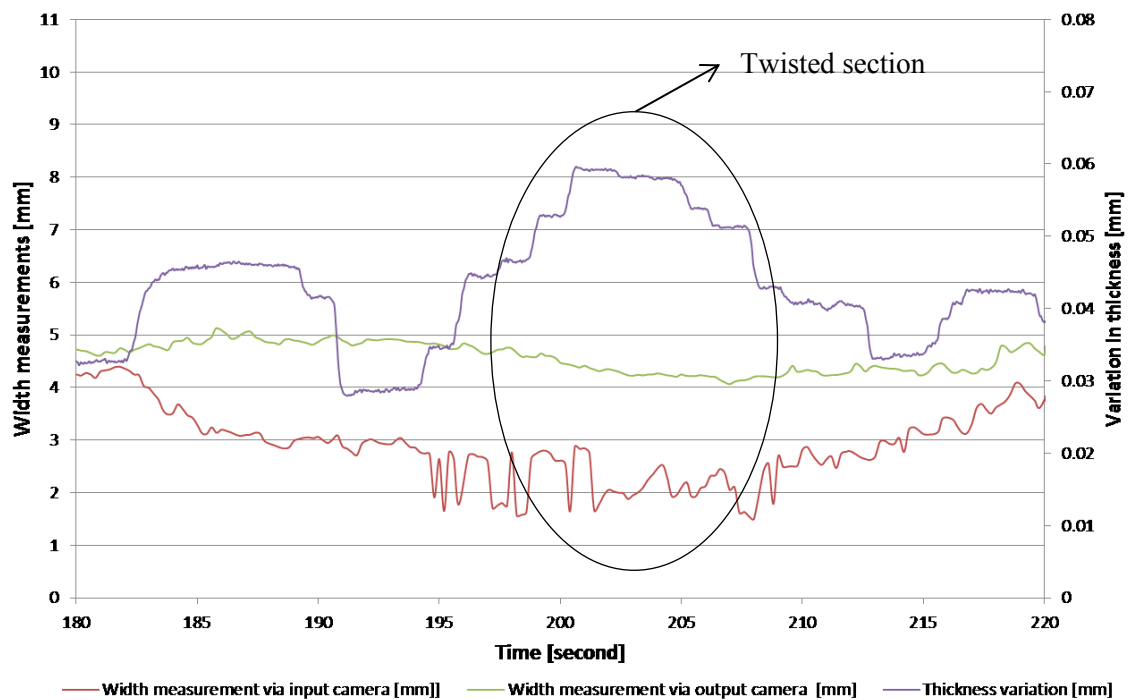
Figure 37 Example of the typical measurements obtained during the experiments: (i) thickness measurements via the pressure load-cell; and (ii) the tow width measurements obtained by analysing the images taken by the input and output cameras.

Since the data from the load-cells and cameras were measuring at three different spatial points, there was a temporal offset for the measurements of the width in, thickness and width out for each tested section of the creel. This temporal offset was calculated using the relative distances from the rollers to the cameras and the traversing speed of the tow. Because the data were time stamped, the addition and subtraction of this temporal offset to the camera input and output time stamps respectively enabled the possibility of representing the superposition of the three measurements of the same section of the creel. An example of this superposition is shown in Figure 38, where a correlation between the changes in the thickness and width can be observed.

It was found that in the experiments involving centre-pull, due to the existence of a much higher number of twists in the creel, the data from the cameras were not accurately correlated with the thickness measurements (after performing the addition and subtraction of the above mentioned temporal offset). This was attributed to the mechanical fixations deployed to drive the creel into the measurement rig, which made the twists tended to be concentrated below the camera-in section rather than traversing through the cylinders. This phenomenon caused non-accurate width measurements when the data were spatially-correlated by the temporal offset.



(i)



(ii)

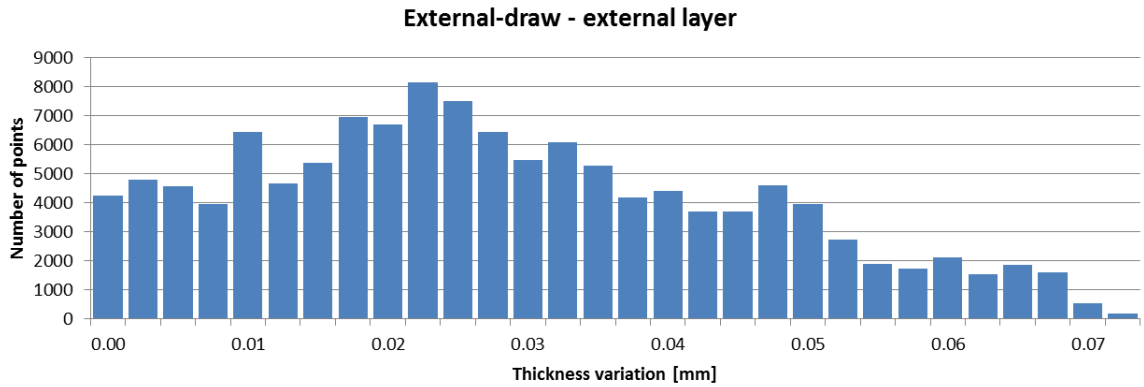
Figure 38 Magnification of the superposition of the data, after adding and subtracting the temporal offset from the input and output cameras respectively: (i) a section of the tow with steady changes in the width/thickness; meanwhile the graph (ii) illustration of a twisted section.

Due to the large number of points involved in the tests, statistical analysis was performed for each cluster using 30 equal intervals of data streams for classifying and calculating the mean and standard deviation.

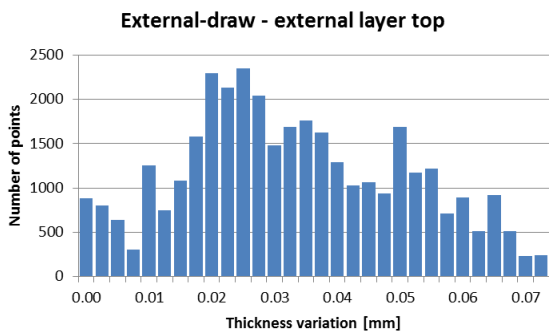
#### ***4.2.4.1 Thickness variation: external-draw experiments***

The data associated with the thickness of the tow from the creel for the external-draw experiments are shown in Figure 39, Figure 40 and Figure 41. The data for each Figure corresponds to a specific layer of the creel (external, centre and internal –see Figure 4) and includes the following information: (a) histogram of thicknesses for the specified layer of the creel; (b) histogram of the thicknesses for tows obtained from the top, middle and bottom zones of the layer under study; and (c) summaries of the mean and the standard deviation for the measured thicknesses. The reading “0”, which appears in all the histograms, corresponded to the minimum thickness measured in each experiment. As explained before, the data calculated were not absolute (the initial thickness was not measured) and hence, only relative changes of thickness were obtained.

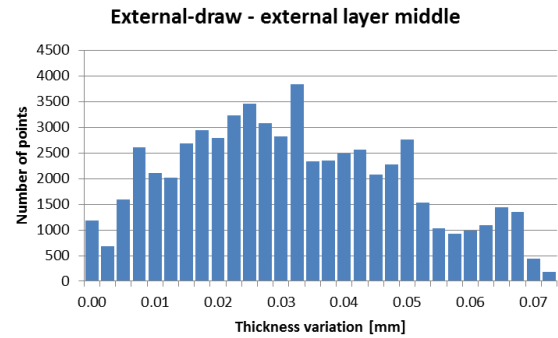
#### 4.2.4.1.1 External layer



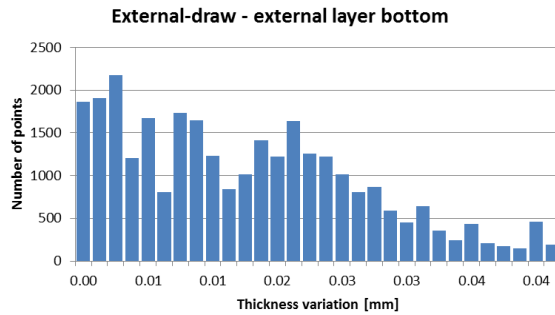
(i)



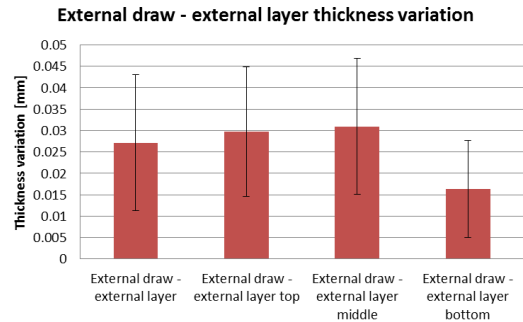
(ii)



(iii)



(iv)

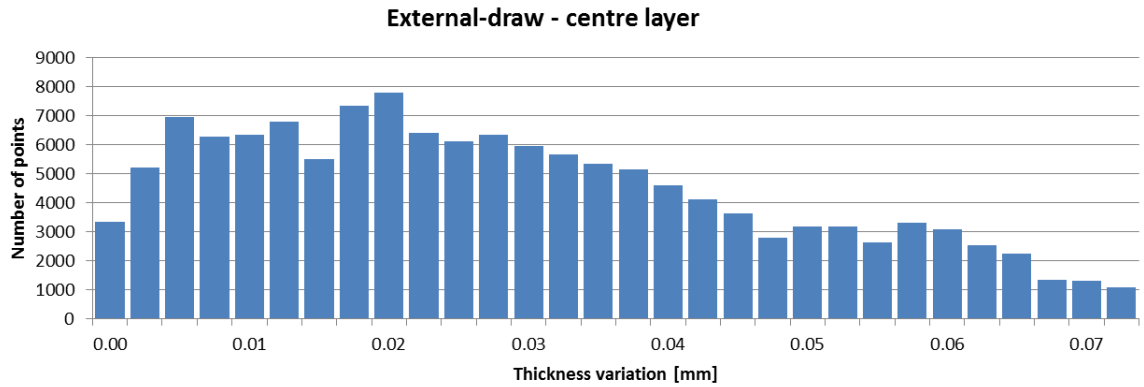


(v)

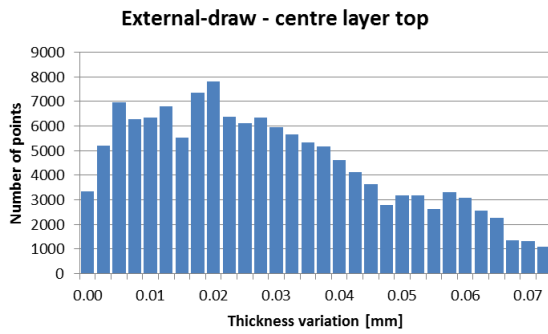
Figure 39 Summary of the thickness of a tow where the bundle was unwound using external-draw.

Figure 39 (i) shows the thickness variation for the full experiment. Figure 39 (ii), (iii) and (iv) represents the thickness variation in the top, middle and bottom zones for the external layer of the creel. Figure 39 (v) shows the mean and the standard deviation for the thickness variation for each zone in the external layer of the creel.

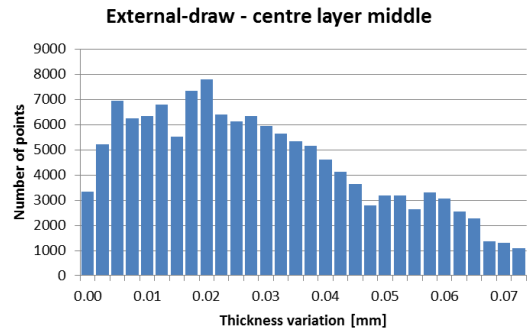
#### 4.2.4.1.2 Centre layer



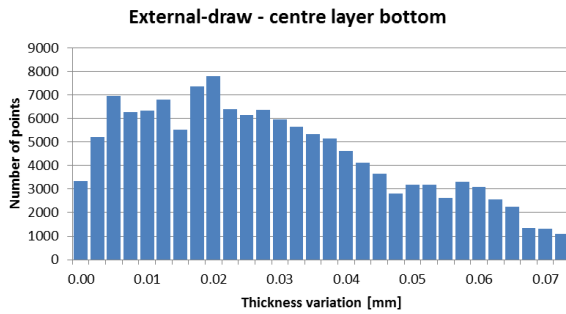
(i)



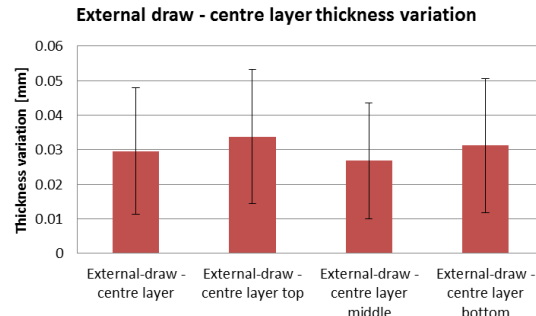
(ii)



(iii)



(iv)



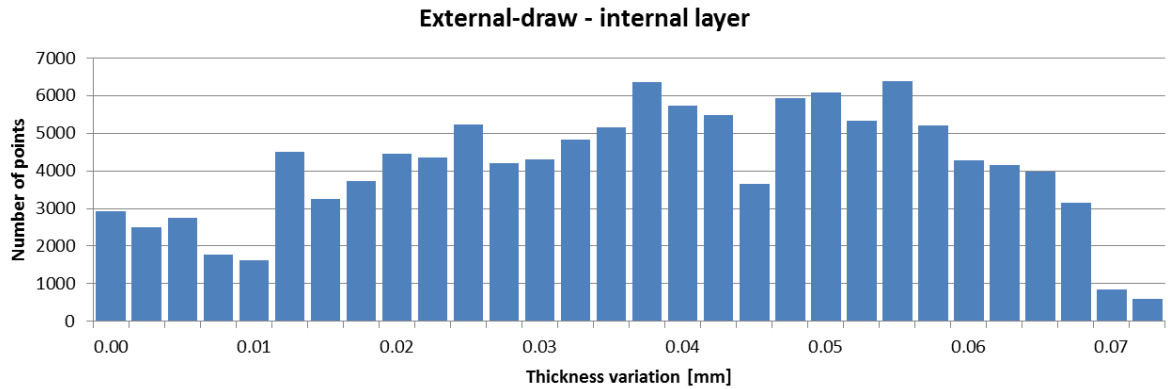
(v)

Figure 40 Summary of the thickness of a tow where the bundle was unwound using external-draw.

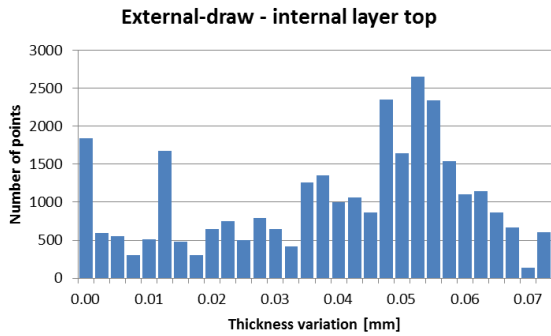
Figure 40 (i) shows the thickness variation for the full experiment. Figure 40 (ii), (iii) and (iv) represents the thickness variation in the top, middle and bottom zones for the middle layer of the creel.

Figure 40 (v) shows the mean and the standard deviation for the thickness variation for each zone in the centre layer of the creel.

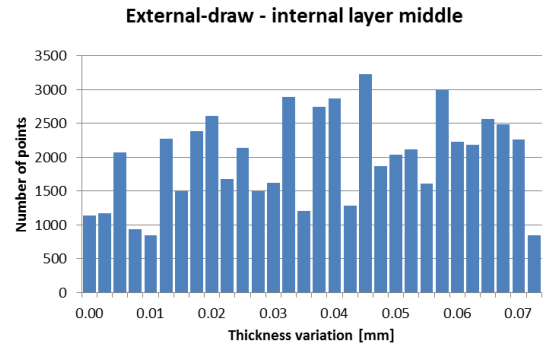
### 4.2.4.1.3 Internal layer



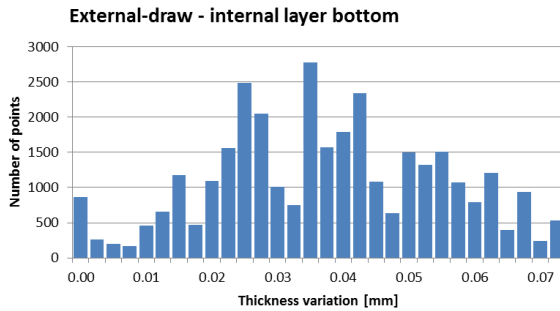
(i)



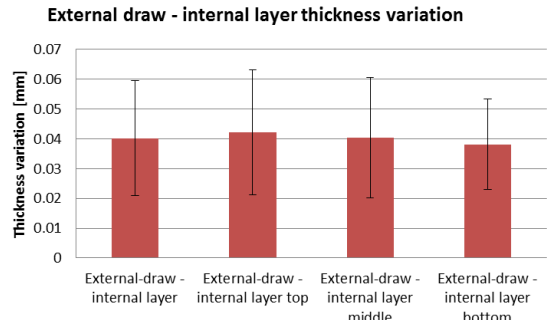
(ii)



(iii)



(iv)



(v)

Figure 41 Summary of the thickness of a tow where the bundle was unwound using external-draw.

Figure 41 (i) shows the thickness variation for the full experiment. Figure 41 (ii), (iii) and (iv) represents the thickness variation in the top, middle and bottom zones for the inner layer of the creel. Figure 41 (v) shows of the mean and the standard deviation for the thickness variation for each zone in the inner layer of the creel.

#### 4.2.4.1.4 Summary of the external-draw experiments

The mean and standard deviation shown previously in Figure 39, Figure 40 and Figure 41, have been consolidated in Figure 42. This gives a full description of the thickness variation for the centre-pull experiment. As before, the columns represent the mean and the error bars the  $\pm$  standard deviation.

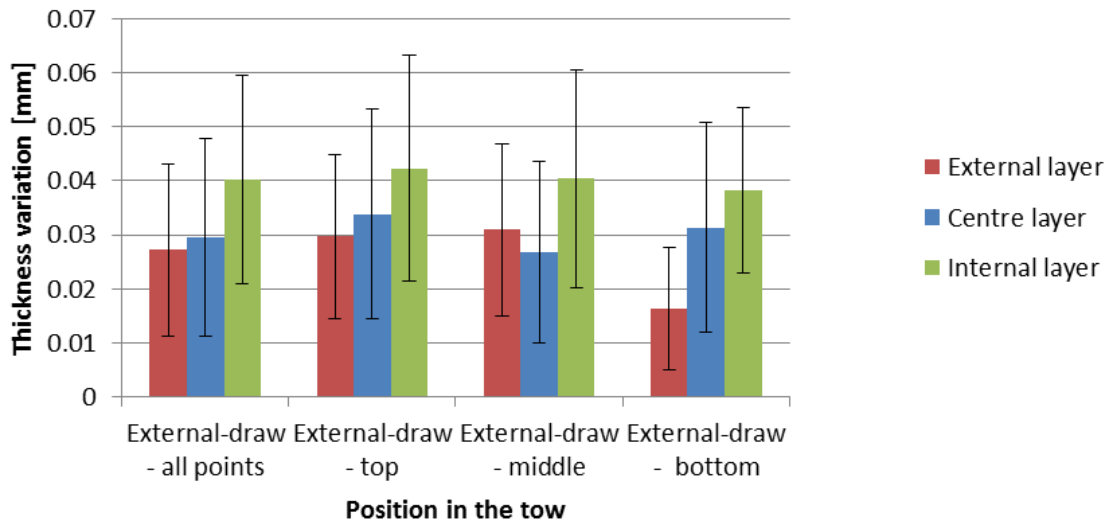


Figure 42 Summary of the external-draw experiments where four sets of data are shown with the mean (coloured columns) and the  $\pm$  standard deviation (error bar): the first dataset compares all the points for each layer, and the next three datasets compare the widths for the top, middle and bottom layers.

In summary, the highest thickness was found in the bore regions (top, mid and bottom) and this reduced accordingly as the diameter was increased (centre and external layers). However, this change in the thickness of the tow was not linear; it varies from 0.04 mm in the internal layer to approximately 0.029 and 0.027 in the central and external layers respectively.

#### 4.2.4.2 Thickness variation in the tow: centre-pull experiments

Figure 43, Figure 44 and Figure 45 show the data for the centre-pull experiments where the data are organised in the same format as in Section 4.2.4.1.

#### 4.2.4.2.1 External layer

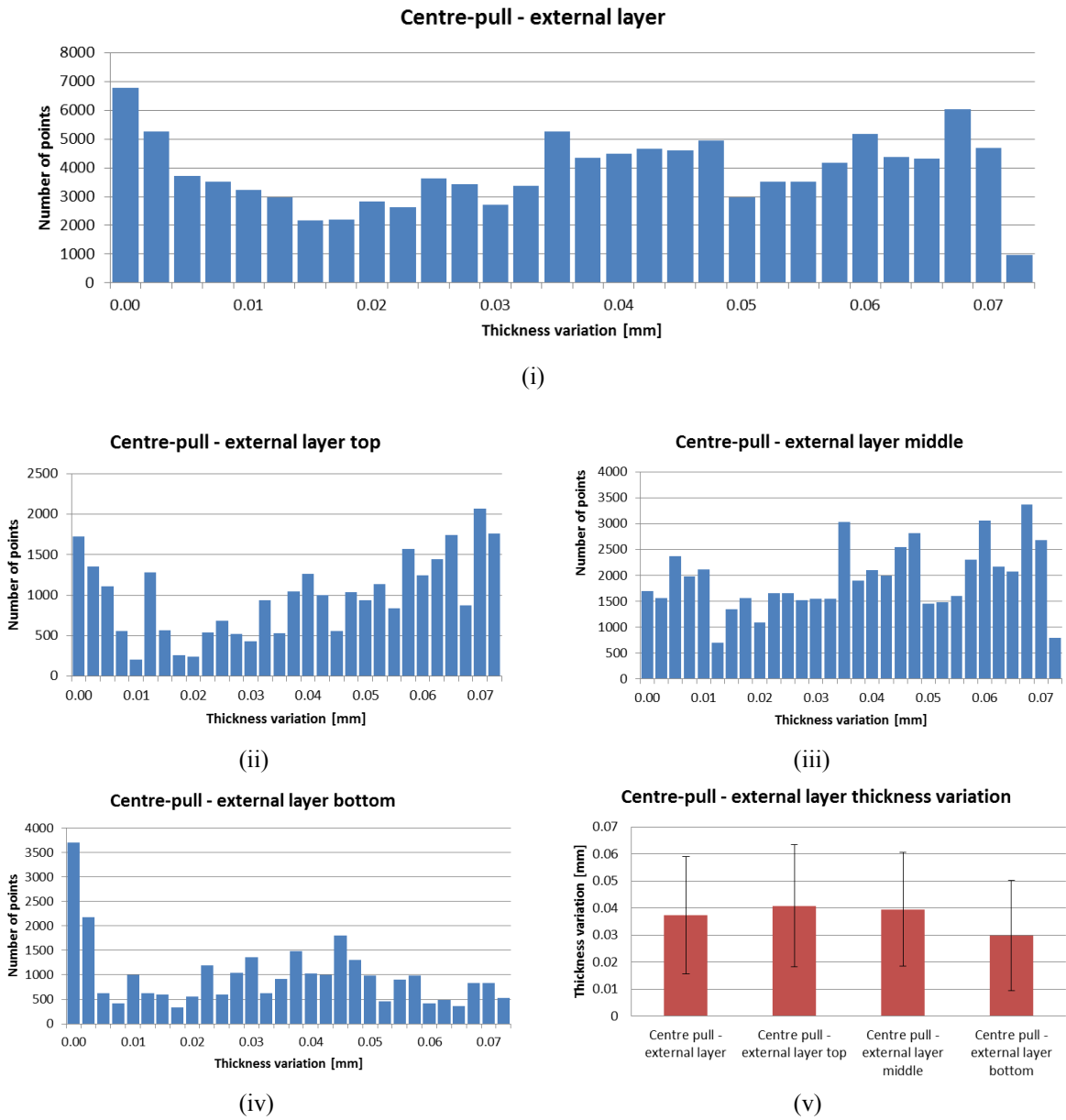


Figure 43 Summary of the thickness of a tow where the bundle was unwound using centre-pull. This dataset represents the outer zone of the creel. Figure 43 (i) shows the thickness variation for the full experiment. Figure 43 (ii), (iii) and (iv) represents the thickness variation in the top, middle and bottom zones for the external layer of the creel. Figure 43 (v) shows the mean and the standard deviation for the thickness variation for each zone in the external layer of the creel.

#### 4.2.4.2.2 Centre layer

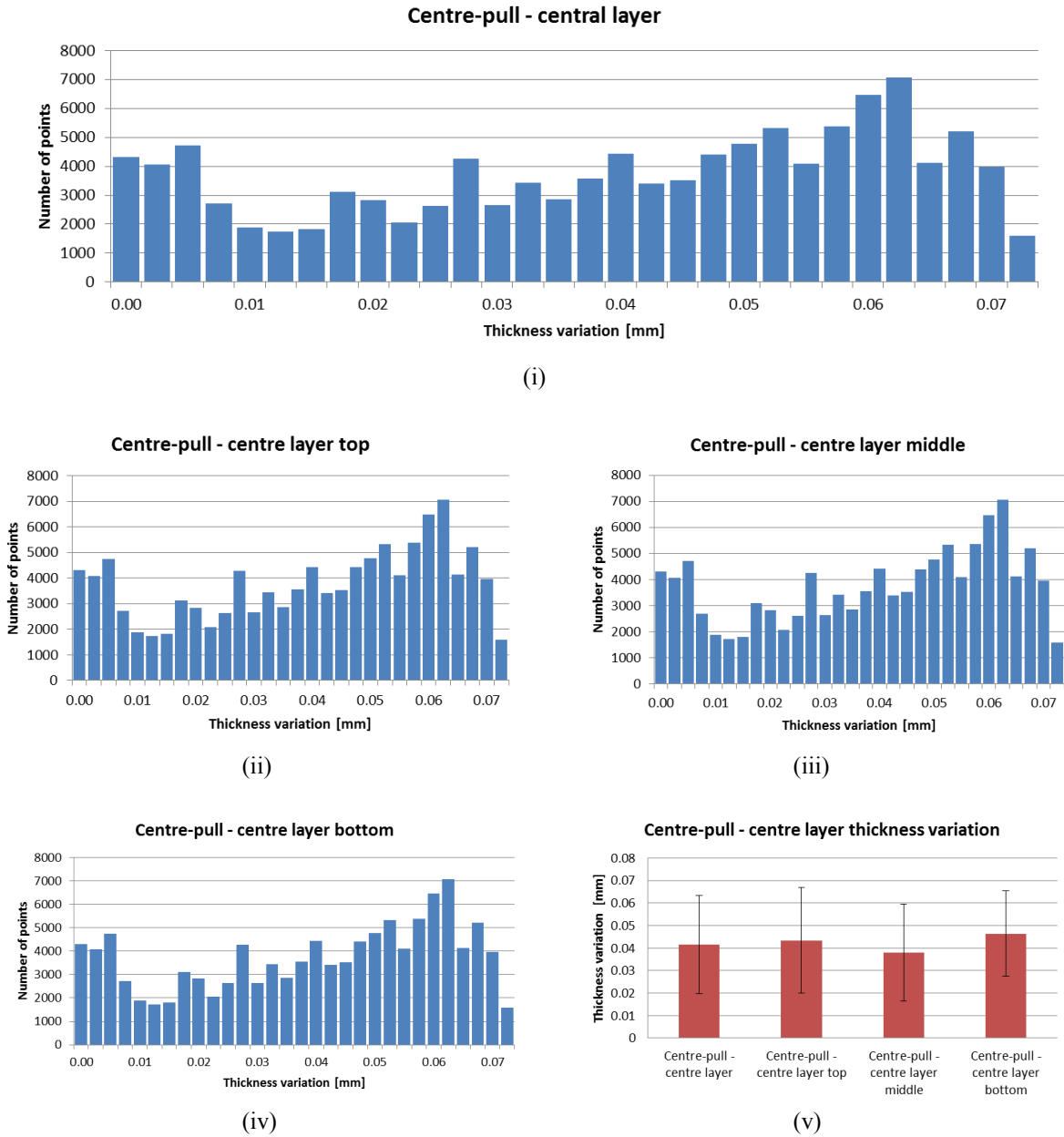
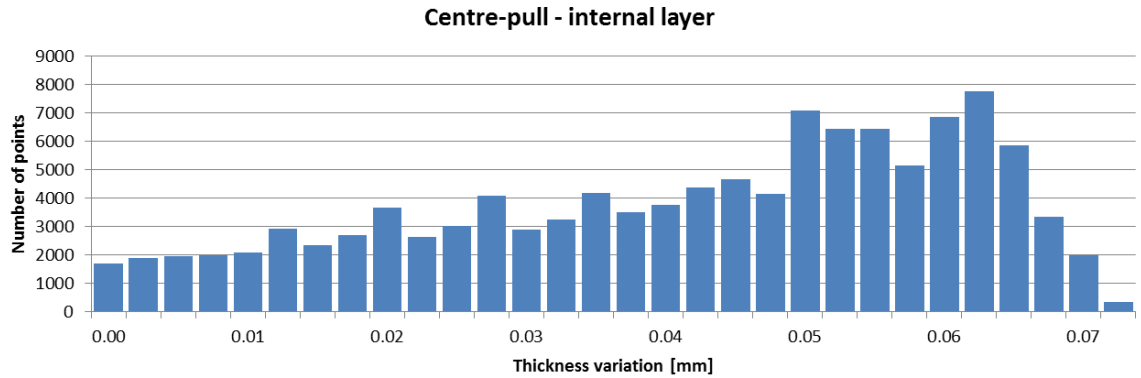
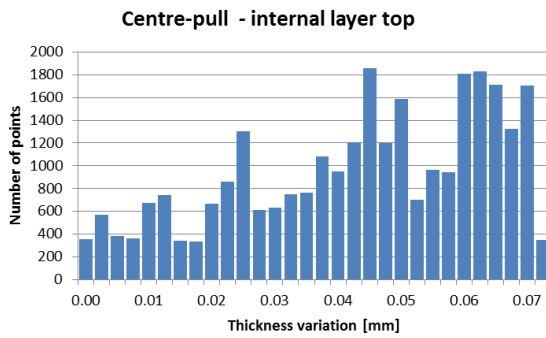


Figure 44 Summary of the thickness of a tow where the bundle was unwound using centre-pull. This dataset represents the mid zone of the creel. Figure 44 (i) shows the thickness variation for the full experiment. Figure 44 (ii), (iii) and (iv) represents the thickness variation in the top, middle and bottom zones for the mid layer of the creel. Figure 44 (v) shows the mean and the standard deviation for the thickness variation for each zone in the mid layer of the creel.

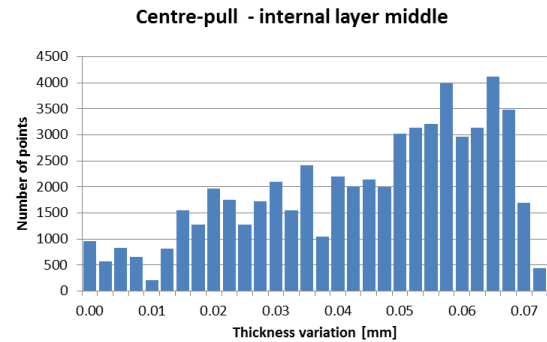
### 4.2.4.2.3 Internal layer



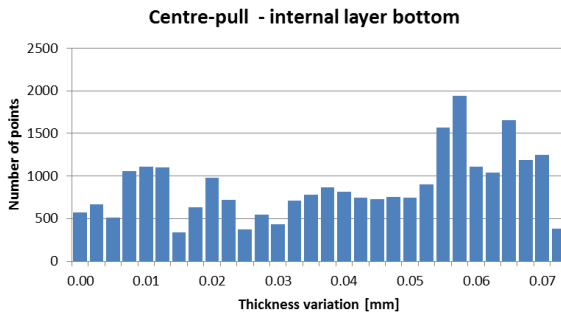
(i)



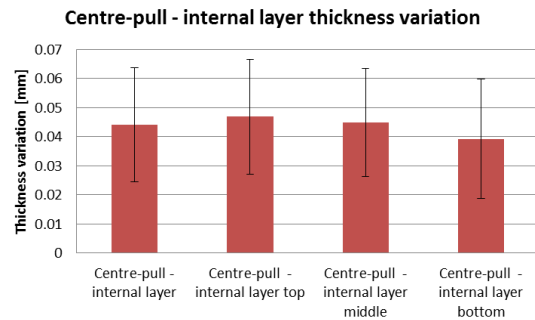
(ii)



(iii)



(iv)



(v)

Figure 45 Summary of the thickness of a tow where the bundle was unwound using centre-pull. This dataset represents the inner zone of the creel. Figure 45 (i) shows the thickness variation for the full set of experiments. Figure 45 (ii), (iii) and (iv) represents the thickness variation in the top, middle and bottom zones for the inner bore layer of the creel. Figure 45 (v) shows the mean and the standard deviation for the thickness variation for each zone in the inner layer of the creel.

#### 4.2.4.2.4 Summary of the centre-pull experiments

The means and standard deviation shown in Figure 43, Figure 44 and Figure 45 have been consolidated in Figure 46, summarising the full description of the thickness variation of the tows when they are unwound using the centre-pull method. As before, the columns represent the mean and the error the  $\pm$  standard deviation.

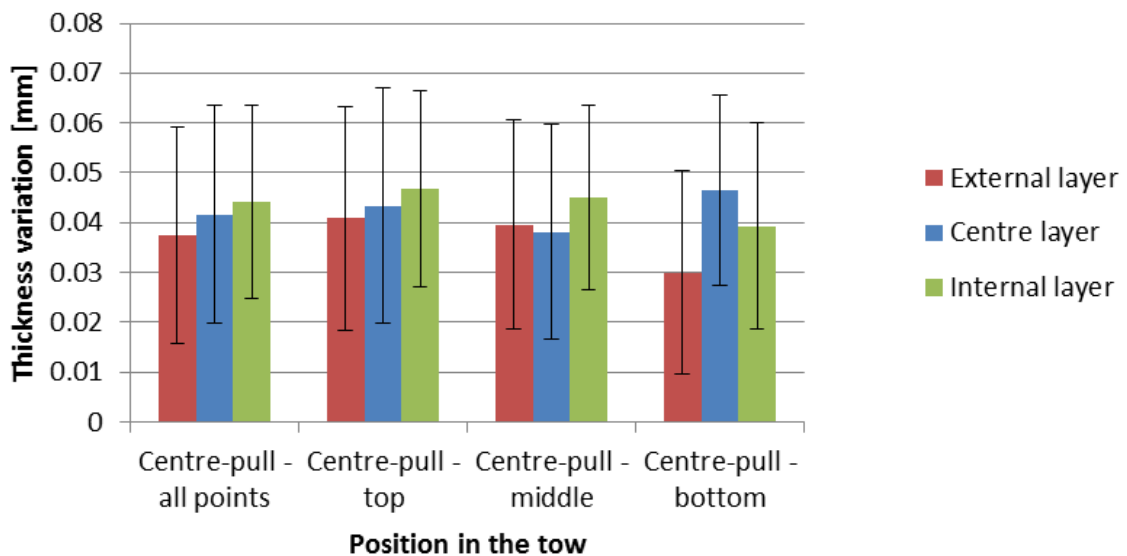


Figure 46 Summary of the centre-pull experiments where four datasets are shown with the mean (coloured columns) and the  $\pm$  standard deviation (error bars). The first dataset compares all the points for each layer. The remaining three datasets compare the widths of the tow in the top, middle and bottom positions of the creel.

As observed in the external-draw experiments, considering only the thickness variations with regards to the defined layers and without considering the position within the creel (top, mid, bottom), there is a trend where the higher thickness is located close to the core or bore of the creel. Besides, the thickness of the tows decreases when traversing to the outer layers of the creel. Considering the positions within the creel (top, mid, bottom), this trend is not consistent possibly due to the creation of twists as the fibre is unwound via centre-pull. This in turn causes significant variability in the thickness.

#### 4.2.4.3 Thickness comparison between centre-pull and external-draw

The comparison between centre-pull and external-draw is shown in Figure 47. It demonstrates that although the creels are from the same reference and batch numbers, as expected, there is a significantly higher variation, with a higher standard deviation, when the tow is unwound by centre-pull.

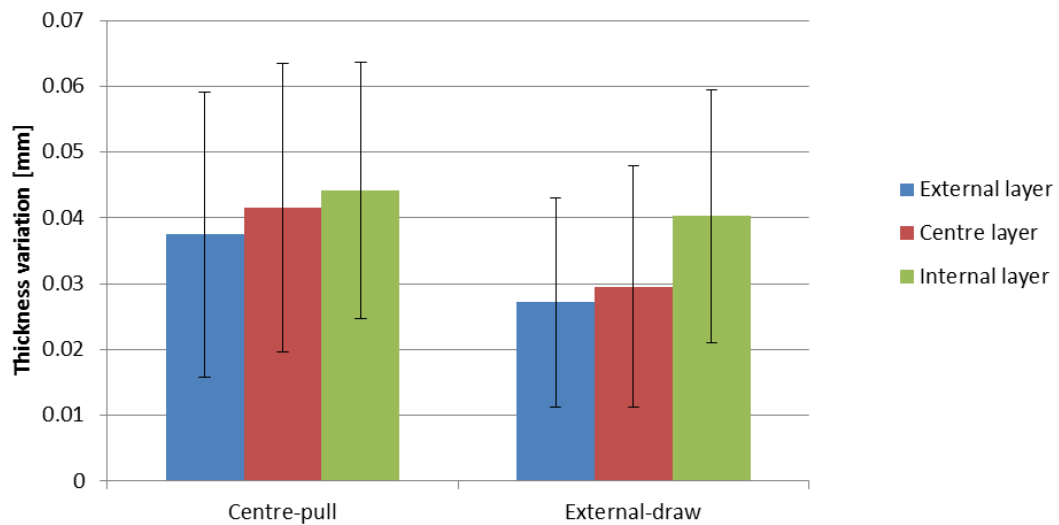


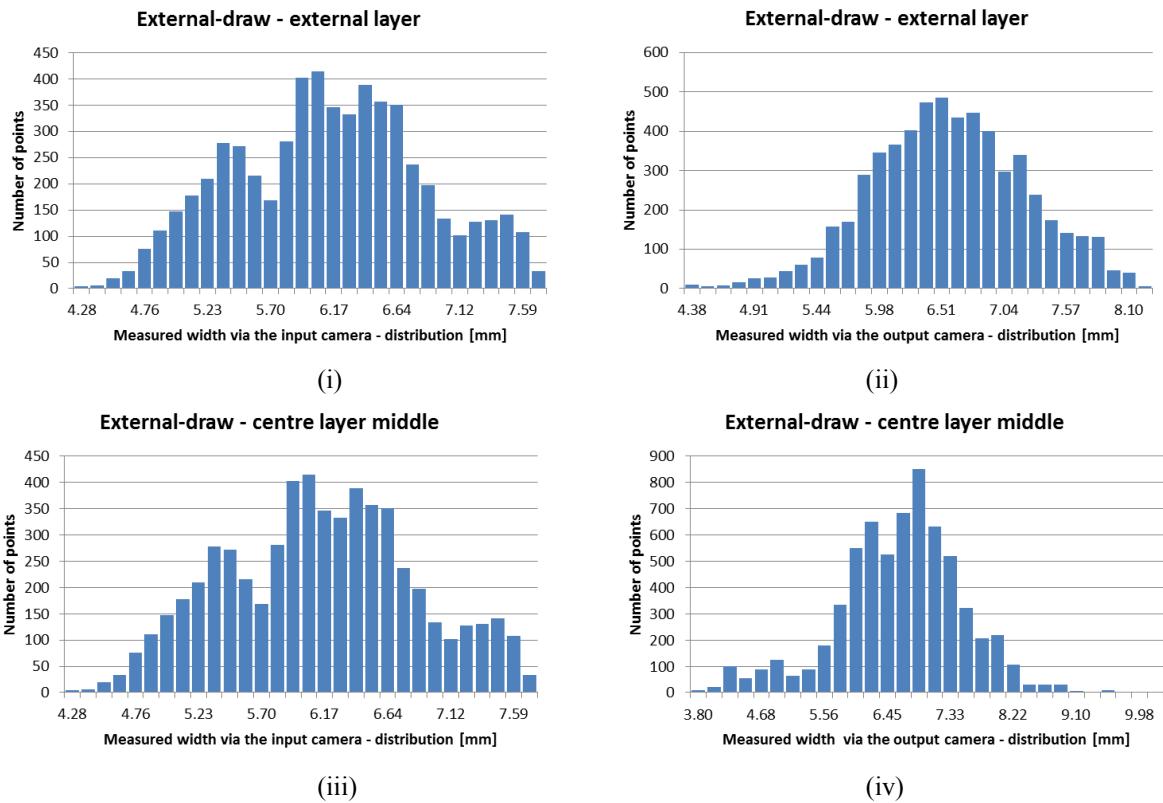
Figure 47 Measured thickness of the tow as a function of the method of un-winding technique. The data are presented in two datasets which show the mean (colour-coded columns) and the  $\pm$  standard deviation (error bars).

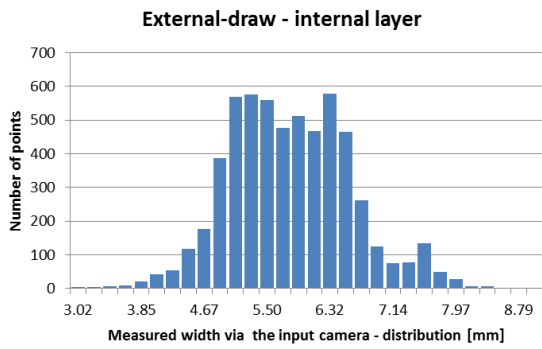
Both unwinding methods, without considering the pre-defined zones of the creel (top, middle or bottom), show that there is a clear trend where the thickness of the tow is higher in the bore, and it decreases when traversing to the outer surface. It is speculated that this trend is most likely due to the manufacturing method of the glass described in Section 2.2. In other words, this variation is probably caused by the differences in the tension when the fibres are wound to form the creel.

In addition, the external-draw method showed lower variations in the mean thickness of the tow along with lower standard deviations than when centre-pull is used. This effect can be explained via the introduction of twists when a centre-pull method of unwinding is used. The twist introduced a decrease in the width and thus an increase in the thickness; the random position of these twists created a higher variability in the readings.

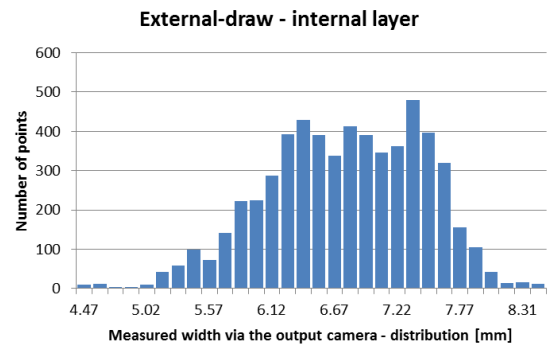
#### 4.2.4.4 Width variation in the tow: external-draw experiments

A summary of the widths obtained by the tow-input and output cameras for each one of the three layers is shown in Figure 48. The consolidated data for comparison purposes are presented in Figure 49.



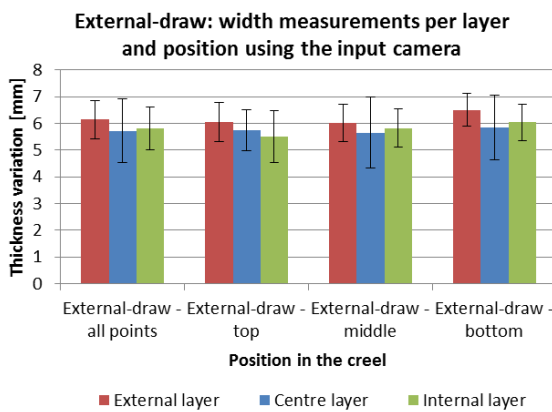


(v)

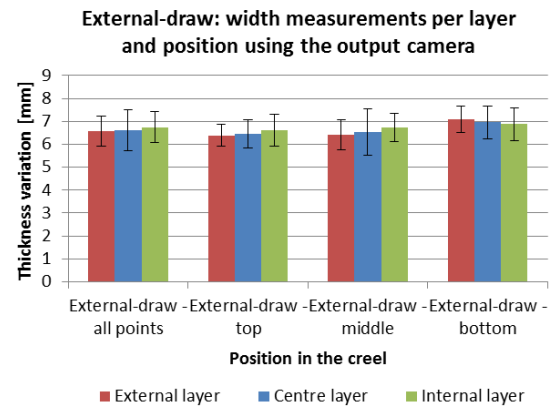


(vi)

Figure 48 Summary of the relative tow widths measured by the tow input and the output cameras for a creel of Hybon 2026 Tex 2400 (PPG). Here the tow was unwound by external-draw. Figure 48 (i) and (ii) show the distribution of the tow widths for the external layer. Figure 48 (iii) and (iv) show the distribution of the readings in the centre layer; and Figure 48 (v) and (vi) show the distribution of the readings in the internal layer.



(i) Width measurements using the input camera



(ii) Width measurements using the output camera

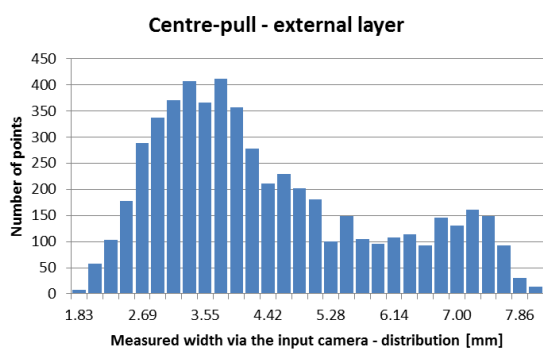
Figure 49 Consolidated data tow width for the various layers and zones for the creel. The histograms represent data acquired by the input and output cameras as the tow enters and leaves the pair of rollers. This dataset is for the a creel of PPG Hybon 2026 Tex 2400, unwound using the external-draw method.

With reference to the consolidated data presented in Figure 49, the first conclusion is that the process of passing the tow in between the pair of rollers spreads them slightly but this renders the width with more uniformity with a lower degree of variability. However, with regards to the analysis of the different clusters (zones and layers), no obvious trend was observed even though the expectation was to see a trend, similar to that observed for the thickness of the tow. Possible reason for this uniformity in the tow width measurements may be attributed to one or

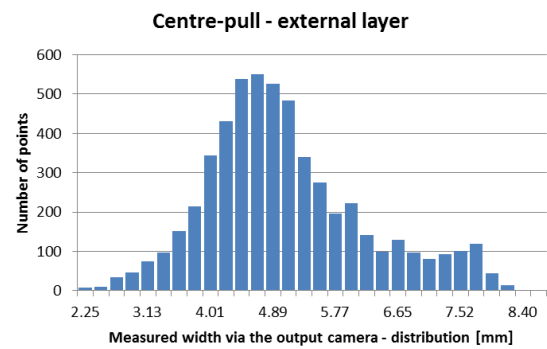
more of the following: (i) since the cameras effectively measured the widths in air (not in contact with a surface), the applied tension would draw the filaments together; (ii) the applied pressure via the pair of rollers may have been too high thus spreading the tow unintentionally; and (iii) the data indicated that the vibrations introduced in the line during the experiment may have created some distortions in the width reading and hence the loss of some precision. Any vibration introduced in the experimental setup may have generated a small relative angular displacement between the tow and the measurement planes, thus creating an artificial and variable factor in the datasets.

#### 4.2.4.5 *Width measurement: centre-pull experiments*

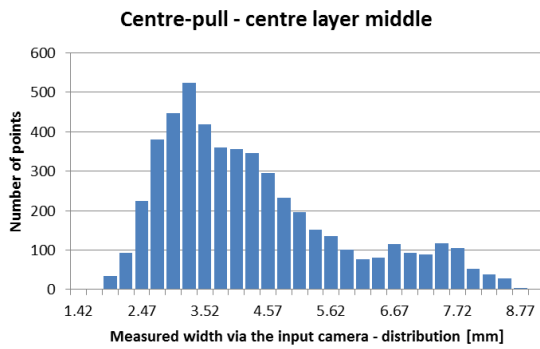
These experiments where the tow was unwound from the creel via centre-pull were carried out in a similar manner as described in Section 4.2.4.4. The data are organised in a similar format as before: a summary of the widths obtained by both cameras for each one of the three layers and the consolidated data for comparison purposes are presented respectively in Figure 50 and Figure 51.



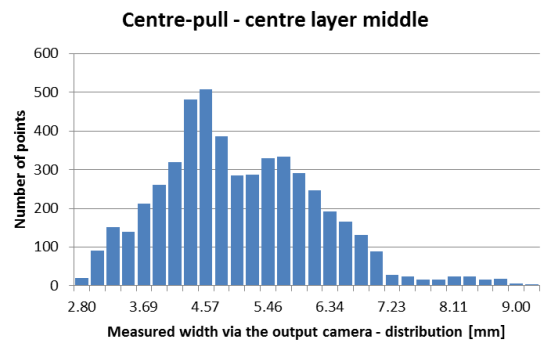
(i)



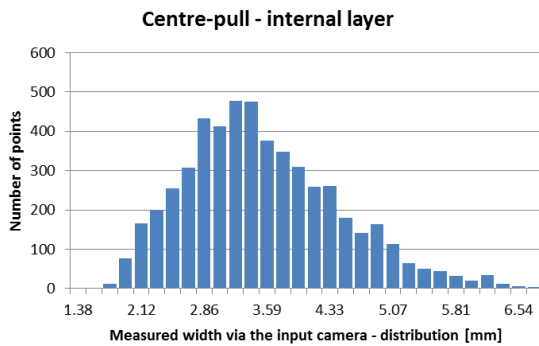
(ii)



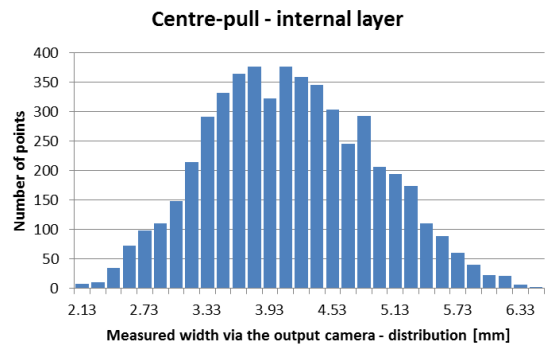
(iii)



(iv)

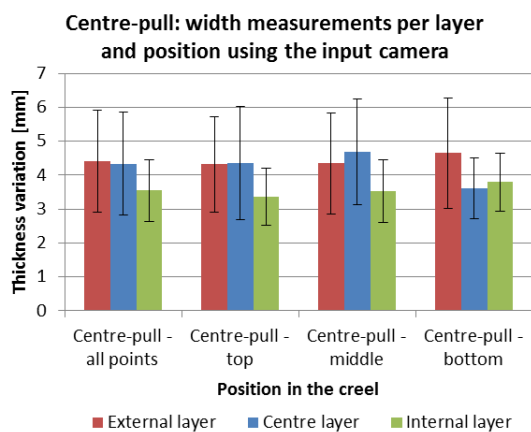


(v)

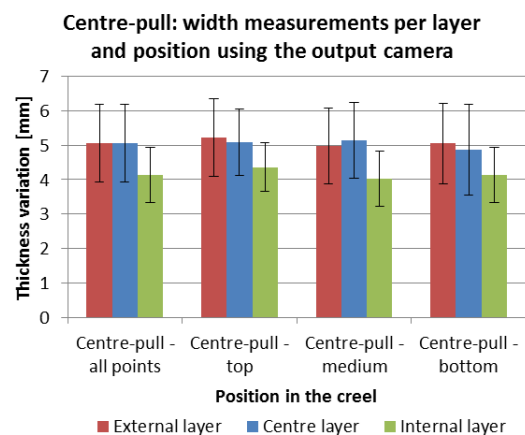


(vi)

Figure 50 Summary of the relative tow widths measured by the tow input and the output cameras for a creel of Hybon 2026 Tex 2400 (PPG). Here the tow was unwound by centre-pull. Figure 50 (i) and (ii) show the distribution of the tow widths for the external layer. Figure 50 (iii) and (iv) show the distribution of the readings in the centre layer; and Figure 50 (v) and (vi) show the distribution of the readings in the internal layer.



(i) Width measurements using the input camera



(ii) Width measurements using the output camera

Figure 51 Consolidated data tow width for the various layers and zones for the creel. The histograms represent data acquired by the input and output cameras as the tow enters and leaves the pair of rollers. This dataset is for a creel of PPG Hybon 2026 Tex 2400, unwound using the centre-pull method.

With reference to the centre-pull experiments, as expected, the variability in the widths is higher due to the presence of twists as discussed previously. A notable feature of the data presented in Figure 51 is that the width increases as the diameter of the bore increases during centre-pull experiments. This observation may be caused by the introduction of fewer twists per unwinding length as the diameter of the creel was increased. This can create a lower clustering of the twists in the tow and thus lead to a general increase in the apparent width. This observation suggests that creels with a smaller bore will introduce more twists if the fibres are subjected to centre-pull.

#### 4.2.4.6 Width comparison between both unwinding methods

A comparison is established in the Figure 52 consolidating the data from each layer with regard to the unwound method. This information clearly shows that the width using external-draw is bigger than that obtained using centre-pull which means a higher thickness. In addition, the variability of the readings is lower using external-draw.

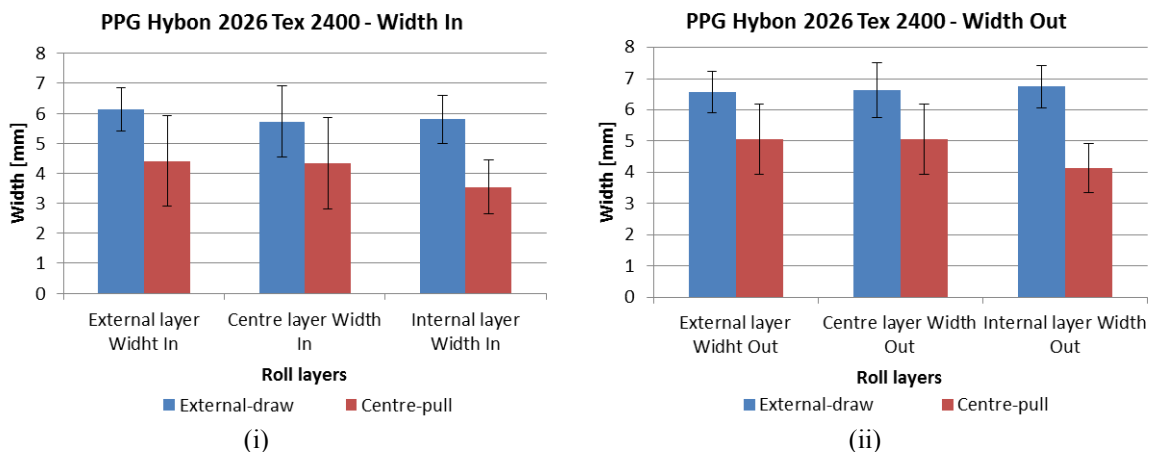


Figure 52 Width comparison by layers for the two unwind methods showing; (i) the width as measured by the input camera or before passing through the rig; and (ii) the width as measured by the output camera or after passing through the rig. The columns show the means, and the error bars represent the  $\pm$  standard deviation.

#### 4.2.5 Tension measurements

The load-cell for monitoring the tension in the tow generated exactly in the same manner to that described for measuring the pressure in Section 4.2.4. The sampling rate was 100 Hz with a line speed of 1050 mm/minute. This permitted data acquisition of the tension each time 0.175 mm of fibre travel in between the rollers. Details of the experimental parameters were presented in Table 8. An example of the information recorded from both load-cells is given in Figure 53.

Due to the low pressure applied within both cylinders during the tests performed (as the remit was not to change the geometry of the tow), the readings for the tension created within the tow were not used for extracting any conclusion about the changes in the geometry.

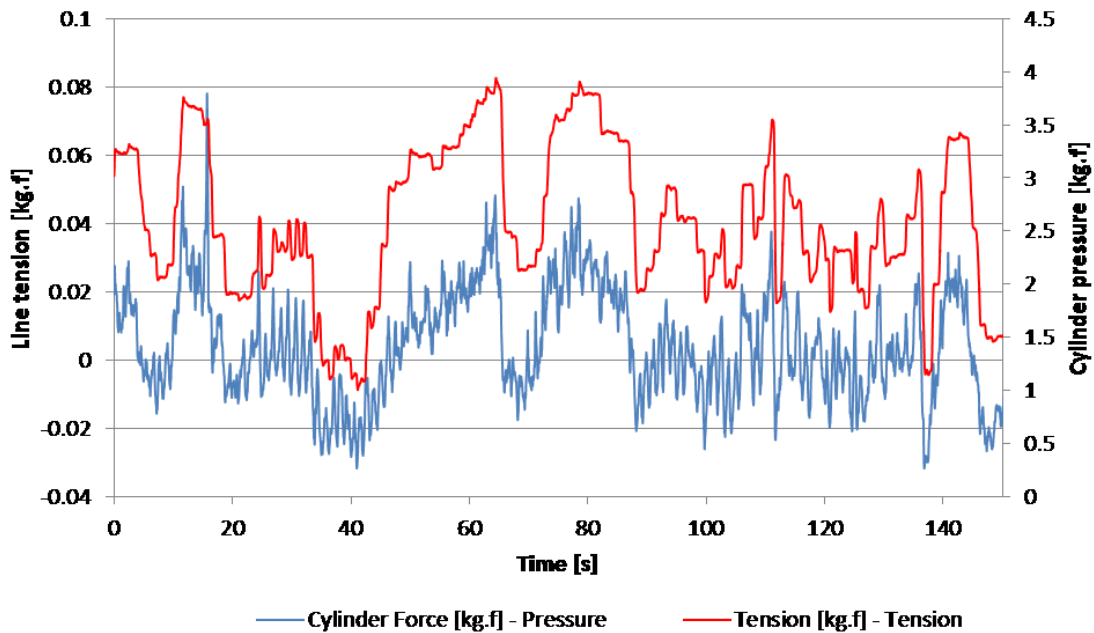


Figure 53 Superposition of the readings of the pressure load-cell (red, with scale on the right) and the tension load-cell (blue, with scale in the left) during 150 seconds.

As it was explained before, changes in the thickness of the tow were measured by the pressure load-cell by the movement of the upper roller against a pressurised pneumatic cylinder (red

series of Figure 53). This phenomenon creates very small changes in the line tension up to  $\pm 0.1$  kg.f as recorded by the tension load-cell (blue series in Figure 53). It is emphasised that for all the experiments, the profile in the tension was nearly a scaled copy of the pressure profile. This denotes the high sensitivity of a load-cell when it is placed in a suspended position (see Figure 13 and Figure 14).

## 5 Conclusions

- a. A literature review was carried out to establish the state-of-the-art with regard the fibre spreading and in-situ monitoring of the impregnation process. This study concluded that there was merit in developing a low-cost image analysis-based system to enable real-time monitoring of the width of the bundle and the impregnation process (axial, transverse and through-thickness).
- b. A coding system was used to define the relative positions of the tows of within the creel.
- c. A pair of low-cost CMOS-cameras was purchase and a platform was designed and built to accommodate the cameras and a section of the tow. A custom LED-based lightning system was designed, constructed and installed. The fixture for housing the tow enabled the tow to be positioned in the same location for the various experiments. An enclosure was built out of card-board to exclude the stray-light. Two orifices were introduced into the card-board shield to enable a micro-pipette to be located such that its tip was positioned over the centre of the tow. The second orifice was used to locate a UV probe to “freeze” the motion of the photo-curable resin. The top-camera was used to enable fine adjustment of the tip of the micro-pipette in such a way that the drop of resin was always dispensed on the centre of the tow.
- d. Custom-written software in LabVIEW was used to track “the motion” of the drop of resin in the axial and transverse directions via the top-camera. The bottom camera was used to infer the through-thickness permeation.
- e. It was necessary to use a pigmented photo-curable resin because of the contrast of the as-received resin was poor. The photo-curable feature was used for “freezing” the movement

of the resin by the application of an appropriate UV-light. The samples containing the cross-linked resin were used during the calibration of the system.

- f. With regard to the on-line monitoring of the width of the tow, a rig was designed and built to monitor the thickness (via load-cells). The real-time monitoring of the width was carried out via a pair of CMOS-cameras.
- g. Custom-written software in LabVIEW was used to track and visualise the thickness and the width of the tow in real-time.
- h. Since it was necessary to pigment the resin to improve the contrast, a series of parallel-plate rheological experiments were carried out to determine the viscosity of the as-received and pigmented photo-curable resin. The viscosities of the as-received and pigmented photo-curable resin (0.5 in wt %) were found to be 3.7 and 4.1 Pa.s at 20 °C respectively.
- i. The maximum error associated in measuring the perimeter of the drop of resin as function of impregnation time using the top camera was found to be 7%. In the case of the bottom camera the maximum error was calculated to be 8%.
- j. With respect to the axial, transverse and through-thickness impregnation process, it was found that the fibres from PPG showed much faster impregnation than the Owens Corning. Besides, different evolution trends were found for both different manufacturers (polynomial VS nearly-linear respectively). Regarding the PPG fibres spreading the fibres by an average of about 220%, enabled an increase of about 700% in the through-thickness impregnation in comparison with the as-received fibres during the first 50 seconds of the test. This demonstrates that by spreading the fibres the impregnation rate can be increased dramatically.

- k. The permeability values of the different experiments were calculated, and it was found that a spreading of 200% increased the axial permeability by nearly 250%. The permeability values of the as-received fibres were found approximately four times higher than at calculated using the Gebart's equation; this is possibly because of the specific characteristics of the experimental setup.
- l. Visual analysis of the "frozen" samples demonstrated conclusively that the images taken during the resin permeation process from the top and bottom faces of the tow correlated with the observed permeation front.
- m. It was demonstrated that the technique developed in this study can be used to enable real-time monitoring of the thickness of the tow when the tow is extracted by centre-pull or external-draw.
- n. When centre-pull was used, a higher average thickness was detected with a higher standard deviation. The average thickness when the centre-pull unwinding method was used was found to be around 35% higher in the external and centre layer, and around a 105% higher in the internal layer. In both payout methods (centre-pull and external-draw), the average thickness was found to decreased as the diameter of the creel increased. The same conclusions were obtained with the analysis of the width for both unwinding methods: the width when external-drawn was found to be consistently higger than when centre-pull was used.
- o. The technique developed in this study can be used to enable real-time monitoring of the width and thickness of the tow.
- p. The image-analysis-based technique can be used to study the effects of fibres from different suppliers with regard to the impregnation process.

## **6 Future work**

The following topics are worthy of further research.

(i) The technique for measuring the widths of the fibres should be implemented on a filament winding line and this could be correlated to the degree of impregnation that can be attained as a function of twists. The observation that the number of twists decreases as the diameter of the inner bore increases could have implications and may explain the variability in the void contents observed in filament winding where the tow is extracted via centre-pull.

(ii) The tow width measurement technology developed and demonstrated here could be used to quantify in real-time the effectiveness of techniques for enabling fibre spreading [7].

(iii) The technology developed here for monitoring the rate of axial, transverse and through-thickness impregnation could be used to validate the various models published by other researchers on modelling the impregnation process.

(iv) The technology developed here can also be used to study the effect of specified surface treatments on the rates of impregnation.

## References

- [1] A. Banerjee, L. Sun, S. C. Mantell, and D. Cohen, "Model and experimental study of fiber motion in wet filament winding," *Composites Part A: Applied Science and Manufacturing*, vol. 29, pp. 251-263, 1998.
- [2] S. C. Joshi and Y. C. Lam, "Integrated approach for modelling cure and crystallization kinetics of different polymers in 3D pultrusion simulation," *Journal of Materials Processing Technology*, vol. 174, pp. 178-182, 2006.
- [3] K. N. Kendall, C. D. Rudd, M. J. Owen, and V. Middleton, "Characterization of the resin transfer moulding process," *Composites Manufacturing*, vol. 3, pp. 235-249, 1992.
- [4] K. Croft, L. Lessard, D. Pasini, M. Hojjati, J. Chen, and A. Yousefpour, "Experimental study of the effect of automated fiber placement induced defects on performance of composite laminates," *Composites Part A: Applied Science and Manufacturing*, vol. 42, pp. 484-491, 2011.
- [5] E. Sevkat and M. Brahim, "The bearing strength of pin loaded woven composites manufactured by vacuum assisted resin transfer moulding and hand lay-up techniques," *Procedia Engineering*, vol. 10, pp. 153-158, 2011.
- [6] M. S. Irfan, V. R. Machavaram, R. S. Mahendran, N. Shotton-Gale, C. F. Wait, M. A. Paget, M. Hudson, and G. F. Fernando, "Lateral spreading of a fiber bundle via mechanical means," *Journal of Composite Materials*, vol. 46, pp. 311-330, February 1, 2012 2012.
- [7] M. Irfan, V. Machavaram, R. Murray, F. Bogonez, C. Wait, S. Pandita, M. Paget, M. Hudson, and G. Fernando, "The design and optimisation of a rig to enable the lateral spreading of fibre bundles," *Journal of Composite Materials*, July 4, 2013 2013.
- [8] Y.-m. Pei, K. Wang, M.-s. Zhan, W. Xu, and X.-j. Ding, "Thermal-oxidative aging of DGEBA/EPN/LMPA epoxy system: Chemical structure and thermal-mechanical properties," *Polymer Degradation and Stability*, vol. 96, pp. 1179-1186, 2011.
- [9] S. Nagendiran, M. Alagar, and I. Hamerton, "Octasilsesquioxane-reinforced DGEBA and TGDDM epoxy nanocomposites: Characterization of thermal, dielectric and morphological properties," *Acta Materialia*, vol. 58, pp. 3345-3356, 2010.
- [10] P. A. Crosby, G. R. Powell, G. F. Fernando, C. M. France, R. C. Spooncer, and D. N. Waters, "In situ cure monitoring of epoxy resins using optical fibre sensors," *Smart Materials and Structures*, vol. 5, p. 415, 1996.
- [11] G. Gardiner. (3/25/2009 January). *The making of glass fiber*. Available: <http://www.compositesworld.com/articles/the-making-of-glass-fiber>
- [12] A. T. DiBenedetto, "Tailoring of interfaces in glass fiber reinforced polymer composites: a review," *Materials Science and Engineering: A*, vol. 302, pp. 74-82, 2001.
- [13] -. A. T. M. A. T. Robert W. Fox (Robert William), 1938- Philip J Pritchard, *Introduction to fluid mechanics*: Hoboken, N.J. : Wiley 2004.
- [14] Z.-R. Chen, Lin Ye, and Meng Lu, "Permeability Predictions for Woven Fabric Preforms," *Journal of Composite Materials*, vol. 44, pp. 1569-1586, June 1, 2010 2010.

- [15] A. Nabovati, E. W. Llewellyn, and A. C. M. Sousa, "A general model for the permeability of fibrous porous media based on fluid flow simulations using the lattice Boltzmann method," *Composites Part A: Applied Science and Manufacturing*, vol. 40, pp. 860-869, 2009.
- [16] B. R. Gebart, "Permeability of unidirectional reinforcements for RTM," *Journal of Composite Materials*, vol. 26, pp. 1100-33, 1992.
- [17] F. Zhou, J. Alms, and S. G. Advani, "A closed form solution for flow in dual scale fibrous porous media under constant injection pressure conditions," *Composites Science and Technology*, vol. 68, pp. 699-708, 2008.
- [18] M. V. Brusckhe and S. G. Advani, "Flow of generalized Newtonian fluids across a periodic array of cylinders," *Journal of Rheology*, vol. 37, pp. 479-498, 1993.
- [19] A. Ragondet, "Experimental characterisation of the vacuum infusion process," Phd, School of mechanical, materials and manufacturing engineering., University of Nottingham, 2005.
- [20] D. H. N. Shotton-Gale, S. D. Pandita, M.A. Paget, J.A. Allen and G. Fernando, "Clean and environmentally friendly wet-filament winding," in *Management, recycling and reuse of waste composites*, V. Goodship, Ed., ed: Woodhead Publishing Limited, 2010, pp. 329-368.
- [21] S. D. Pandita, M. S. Irfan, V. R. Machavaram, N. Shotton-Gale, R. S. Mahendran, C. F. Wait, M. A. Paget, D. Harris, C. Leek, and G. F. Fernando, "Clean wet-filament winding - Part 1: design concept and simulations," *Journal of Composite Materials*, 2012.
- [22] P. C. Carman, "Fluid flow through granular beds," *Process Safety and Environmental Protection: Transactions of the Institution of Chemical Engineers, Part B*, vol. 75, pp. S32-S48, 1997.
- [23] A. L. Berdichevsky and Z. Cai, "Preform permeability predictions by self-consistent method and finite element simulation," *Polymer Composites*, vol. 14, pp. 132-143, 1993.
- [24] S. C. Amico and C. Lekakou, "Axial impregnation of a fiber bundle. Part 1: Capillary experiments," *Polymer Composites*, vol. 23, pp. 249-263, 2002.
- [25] X. Chen and T. D. Papathanasiou, "Micro-scale modeling of axial flow through unidirectional disordered fiber arrays," *Composites Science and Technology*, vol. 67, pp. 1286-1293, 2007.
- [26] K. J. Ahn, J. C. Seferis, and J. C. Berg, "Simultaneous measurements of permeability and capillary pressure of thermosetting matrices in woven fabric reinforcements," *Polymer Composites*, vol. 12, pp. 146-152, 1991.
- [27] S. D. Schwab, R. L. Levy, and G. G. Glover, "Sensor system for monitoring impregnation and cure during resin transfer molding," *Polymer Composites*, vol. 17, pp. 312-316, 1996.
- [28] T. Luthy and P. Ermanni, "Linear direct current sensing system for flow monitoring in Liquid Composite Moulding," *Composites Part A: Applied Science and Manufacturing*, vol. 33, pp. 385-397, 2002.
- [29] R. Matsuzaki, S. Kobayashi, A. Todoroki, and Y. Mizutani, "Cross-sectional monitoring of resin impregnation using an area-sensor array in an RTM process," *Composites Part A: Applied Science and Manufacturing*, vol. 43, pp. 695-702, 2012.
- [30] B. Yenilmez and E. Murat Sozer, "A grid of dielectric sensors to monitor mold filling and resin cure in resin transfer molding," *Composites Part A: Applied Science and Manufacturing*, vol. 40, pp. 476-489, 2009.

- [31] R. Gauvin, F. Trochu, Y. Lemenn, and L. Diallo, "Permeability measurement and flow simulation through fiber reinforcement," *Polymer Composites*, vol. 17, pp. 34-42, 1996.
- [32] T. Stöven, F. Weyrauch, P. Mitschang, and M. Neitzel, "Continuous monitoring of three-dimensional resin flow through a fibre preform," *Composites Part A: Applied Science and Manufacturing*, vol. 34, pp. 475-480, 2003.
- [33] S. Thomas, C. Bongiovanni, and S. R. Nutt, "In situ estimation of through-thickness resin flow using ultrasound," *Composites Science and Technology*, vol. 68, pp. 3093-3098, 2008.
- [34] J. P. Dunkers, J. L. Lenhart, S. R. Kueh, J. H. van Zanten, S. G. Advani, and R. S. Parnas, "Fiber optic flow and cure sensing for liquid composite molding," *Optics and Lasers in Engineering*, vol. 35, pp. 91-104, 2001.
- [35] N. Gupta and R. Sundaram, "Fiber optic sensors for monitoring flow in vacuum enhanced resin infusion technology (VERITY) process," *Composites Part A: Applied Science and Manufacturing*, vol. 40, pp. 1065-1070, 2009.
- [36] V. Antonucci, M. Giordano, L. Nicolais, A. Calabrò, A. Cusano, A. Cutolo, and S. Insera, "Resin flow monitoring in resin film infusion process," *Journal of Materials Processing Technology*, vol. 143-144, pp. 687-692, 2003.
- [37] C. Lekakou, S. Cook, Y. Deng, T. W. Ang, and G. T. Reed, "Optical fibre sensor for monitoring flow and resin curing in composites manufacturing," *Composites Part A: Applied Science and Manufacturing*, vol. 37, pp. 934-938, 2006.
- [38] S. H. Ahn, W. I. Lee, and G. S. Springer, "Measurement of the Three-Dimensional Permeability of Fiber Preforms Using Embedded Fiber Optic Sensors," *Journal of Composite Materials*, vol. 29, pp. 714-733, April 1, 1995 1995.
- [39] W. Li, Y. D. Huang, L. Liu, and N. T. Chen, "Rapid and nondestructive analysis of quality of prepreg cloth by near-infrared spectroscopy," *Composites Science and Technology*, vol. 65, pp. 1668-1674, 2005.
- [40] B. Jiang and Y. D. Huang, "Investigation of the impregnation degree of the prepreg by near infrared spectroscopy," *Composites Part B: Engineering*, vol. 42, pp. 946-948, 2011.
- [41] Y. J. Lee, J. H. Wu, Y. Hsu, and C. H. Chung, "A prediction method on in-plane permeability of mat/roving fibers laminates in vacuum assisted resin transfer molding," *Polymer Composites*, vol. 27, pp. 665-670, 2006.
- [42] P. B. Nedanov and S. G. Advani, "A Method to Determine 3D Permeability of Fibrous Reinforcements," *Journal of Composite Materials*, vol. 36, pp. 241-254, January 1, 2002 2002.
- [43] J. Schell, M. Siegrist, and P. Ermanni, "Experimental Determination of the Transversal and Longitudinal Fibre Bundle Permeability," *Applied Composite Materials*, vol. 14, pp. 117-128, 2007.
- [44] X. Wu, J. Li, and R. A. Shenoi, "A New Method to Determine Fiber Transverse Permeability," *Journal of Composite Materials*, vol. 41, pp. 747-756, March 1, 2007 2007.
- [45] P. Synnergren, L. Larsson, and T. S. Lundström, "Digital Speckle Photography: Visualization of Mesoflow through Clustered Fiber Networks," *Appl. Opt.*, vol. 41, pp. 1368-1373, 2002.
- [46] P. Wang, S. Drapier, J. Molimard, A. Vautrin, and J.-C. Minni, "Characterization of Liquid Resin Infusion (LRI) filling by fringe pattern projection and in situ thermocouples," *Composites Part A: Applied Science and Manufacturing*, vol. 41, pp. 36-44, 2010.

- [47] M. S. Irfan, "Summary of Fibre Spreading Methods," *University of Birmingham*, September 2011.
- [48] R. Marissen, L. Th. van der Drift, and J. Sterk. (2000, 10). *Technology for rapid impregnation of fibre bundles with a molten thermoplastic polymer*. Available: <http://www.sciencedirect.com/science/article/pii/S0266353800001226>
- [49] L. D. B. Joseph Lee Lifke, Dana Jesse Finley, Brent William Gordon, "Method and apparatus for spreading fiber bundles," US Patent 6,049,956, 2000.
- [50] B. L. Jean-Michel Guirman, Alain Memphis, "Method and device for producing a textile web by spreading tows," US Patent 6,836,939, 2005.
- [51] Y. O. Narihito Nakagawa, "Fiber separator for producing fiber reinforced metallic or resin body," US Patent 5,101,542, 1992.
- [52] E. M. Sternberg, "Method and apparatus for charging a bundle of filaments," US Patent 3,967,118, 1976.
- [53] R. E. Alan Edelstein, Jonathan M. Peritt, "Electrostatic fiber spreader including a corona discharge device," US Patent 5,200,620, 1993.
- [54] D. R. Juergen Nestler, Frank Vettermann, "Device and method for spreading a carbon fiber hank," US Patent 7,536,761, 2009.
- [55] T. Z. Masahiro Kobayashi, Masahiro Kobayashi, Takamichi Zoda, "Method and apparatus for spreading or dividing yarn, tow or the like," US Patent 3,657,871, 1972.
- [56] T. B. Sager, "Method and apparatus for separating monofilaments forming a strand," US Patent 4,959,895, 1990.
- [57] T. H. Daisaku Akase, Hidetaka Matsumae, Toshihide Sekido, "Method and apparatus for opening reinforcing fiber bundle and method of manufacturing prepegs," US Patent 6,094,791, 2000.
- [58] H. O. Kiyotsugu Tanaka, Hidetaka Matsumae, Seiji Tsuji, Daisaku Akase, "Production device and method for opened fiber bundle and prepreg production method," US Patent 6,743,392, 2004.
- [59] C. G. Daniels, "Pneumatic spreading of filaments," US Patent 3,795,944, 1974.
- [60] J. W. Pryor, "Method and apparatus for conveying filter tow," US Patent 4,537,583, 1985.
- [61] H. F. Tai-Shung Chung, Zev Gurion, Paul E. McMahon, Richard D. Orwoll, Daniel Palangio, "Process for preparing tapes from thermoplastic polymers and carbon fibers," US Patent 4,588,538, 1986.
- [62] J. A. Newell and A. A. Puzianowski, "Development of a pneumatic spreading system for Kevlar-based SiC-precursor carbon fibre tows," 0954-0083, 1999.
- [63] N. Instruments. (March). *Spatial Calibration*. Available: [http://zone.ni.com/reference/en-XX/help/372916J-01/nivisionconcepts/spatial\\_calibration/](http://zone.ni.com/reference/en-XX/help/372916J-01/nivisionconcepts/spatial_calibration/)
- [64] C. G. Relf, *Image Acquisition and Processing with LabVIEW*: CRC Press LLC, 2004.
- [65] N. Instruments. (August 2012). *NI Vision Builder for Automated Inspection Tutorial*.
- [66] S. Rangarajan. Algorithms for edge detection.